AUTOMATED APPROACHES FOR SALT DOME DETECTION FROM 2D AND 3D SEISMIC DATA

BY

ASJAD AMIN

A Dissertation Presented to the
DEANSHIP OF GRADUATE STUDIES

KING FAHD UNIVERSITY OF PETROLEUM & MINERALS

DHAHRAN, SAUDI ARABIA

In Partial Fulfillment of the
Requirements for the Degree of

DOCTOR OF PHILOSOPHY

In

ELECTRICAL ENGINEERING

NOVEMBER 2016

KING FAHD UNIVERSITY OF PETROLEUM & MINERALS
DHAHRAN 31261, SAUDI ARABIA

DEANSHIP OF GRADUATE STUDIES

This thesis, written by **ASJAD AMIN** under the direction of his thesis adviser and approved by his thesis committee, has been presented to and accepted by the Dean of Graduate Studies, in partial fulfillment of the requirements for the degree of **DOCTOR OF PHILOSOPHY IN ELECTRICAL ENGINEERING**.

Dissertation Committee

Dr. Mohamed Deriche (Adviser)

Dr. Ghassan AlRegib (Co-adviser)

Dr. Azzedine Zerguine (Member)

Dr. Lahouari Ghouti (Member)

Dr. Mohamed Mohandes (Member)

Dr. Ali Ahmad Al-Shaikhi
Department Chairman

Dr. Salam A. Zummo
Dean of Graduate Studies

19/12/16
Date

This dissertation is dedicated to my parents, my wife, my children and all family.

ACKNOWLEDGMENTS

In the name of Allah, the Most Beneficient, the Most Merciful

I am thankful to Allah Almighty for His blessings, mercy and support, and for carrying me through this challenging phase of my life's journey.

I would like to deeply thank my adviser Dr. Mohamed Deriche for the continuous support of my doctoral research, and for his patience, enthusiasm and encouragement. His invaluable help of constructive comments and suggestions throughout the experimental and thesis works have contributed to the success of this research. It would not have been possible without him facilitating the necessary resources.

I would like to express my sincere gratitude to my co-adviser Dr. Ghassan AlRegib for his support and guidance, and for sharing his knowledge and valuable ideas with me. I would also like to thank my dissertation committee members Dr. Azzedine Zerguine, Dr. Mohamed Mohandes, and Dr. Lahouari Ghouti for their guidance, insightful comments and constructive feedback.

I am thankful to the King Fahd University of Petroleum and Minerals (KFUPM) for providing me with the research facilities, precious resources, and an environment conducive to intellectual growth for my doctoral research.

Special thanks to all my friends at KFUPM for their kindness and support during my study. I would especially like to mention here the names of Dr. M. Ali Qureshi, Anum Ali, Mujahid Amin, Hussain Ali, Dr. Adeel Sabir, Dr. Alam Zaib, Dr. Naveed Iqbal, Waqas Afzal, Mr. Asim Bukhari. Thanks for the friendship and memories.

My deepest gratitude goes to my beloved parents and siblings for their endless love, prayers, and encouragement. Finally, I would like to thank my wife and children for their love, patience, and understanding. My wife has been extremely supportive throughout my Ph.D. and has made countless sacrifices to help me get to this point.

TABLE OF CONTENTS

LIST OF TABLES

LIST OF FIGURES

NOMENCLATURE

μ Centroid vector of clusters.

c_i Codewords in codebook.

C_σ Coherence attribute from HOSVD.

E_c Coherence estimate from covariance matrix.

D Dictionary of training patches.

$\alpha(.)$ The entries of estimated vector.

θ Orientation of filter.

G_i Gradient of input image in ith direction.

λ_1 Largest eigenvalue attribute.

σ_l Largest singular value attribute from HOSVD.

β Mutual information feature selection coefficient.

$I(x, y)$ Mutual information between variables X and Y.

M Number of attributes.

N Patch size for feature extraction.

J Score for mutual information algorithms.

$Trace_{\sigma}$ Trace attribute from HOSVD.

T_r Trace attribute from covariance matrix.

$A(.)$ Unfolded matrix from tensor.

LIST OF ABBREVIATIONS

ACM Active Contour Model.

CA Coherence Attribute.

CE Coherence Estimate.

CHSA Cumulative Hybrid Seismic Attribute.

CV Chan Vese.

FN False Negative.

FP False Positive.

GLCM Grey Level Co-occurrence Matrix.

GoT Gradient of Texture.

HMM Hidden Markov Model.

HOSVD Higher Order Singular Value Decomposition.

JMI Joint Mutual Information.

LEV Largest EigenValue.

LRI Local Radii Index.

LSV Largest Singular Value.

MI Mutual Information.

MIFS Mutual Information Feature Selection.

MIM Mutual Information Maximization.

mRMR minimum Redundancy Maximum Relevance.

NCIS Normalized Cuts Image Segmentation.

NR No Reflection.

PRC Pairwise Region Comparison.

SVD Singular Value Decomposition.

TN True Negative.

TP True Positive.

THESIS ABSTRACT

NAME: Asjad Amin

TITLE OF STUDY: Automated Approaches for Salt Dome Detection from 2D and 3D Seismic Data

MAJOR FIELD: Electrical Engineering

DATE OF DEGREE: November 2016

Seismic interpretation is commonly used to describe the process of data analysis by either a trained human expert or a computer aided system, with the aim of extracting important geologic features. Such features are then used in different seismic applications such as detection of faults, salt domes, horizons, and other events. The oil and gas industry uses the characteristics received from earth subsurface echoes to detect oil reservoirs. Accurate localization of oil fields is crucial to the exploration process as it can save industry from huge financial losses which otherwise can happen due to drilling at wrong locations. One of the key tasks in seismic data interpretation is the detection of salt bodies, as major accumulations of oil and gas are associated with these structures. This is primarily due to the excellent sealing capabilities of salt domes. Historically, salt dome interpretation has been carried by human experts. Human interpreters require adequate training and experience to perform this task accurately and continuously. However, manual (or subjective) methods are slow, require a large amount of manpower, and can be affected by human fatigue, among other factors. To alleviate the challenges of manual interpretation of salt domes, we witnessed, in recent years, substantial research efforts put in developing automated or semi-automated salt dome detection workflows.

In this thesis, we introduce a number of automated approaches for salt dome detection from 2D and 3D seismic data. We develop a multidirectional 3D edge-detector based salt dome detection technique to overcome the limitations of traditional 2D edge-based methods. We also introduce a data-driven codebook based workflow using texture attributes for efficient detection of salt bodies. Furthermore, we also develop a hybrid model using edge- and texture-based classifiers. The fusion of these two classifiers is carried at the decision level. We also propose new texture-based attributes using the concept of higher order singular value decomposition (HOSVD). The attributes are computed from 3D volumes, thus making them more suitable for 3D seismic data. We also develop a dictionary-based workflow using a feature ranking approach. The ranking is achieved using robust information theoretic models. Finally, we develop 1D HMM models for salt dome detection and tracking. In summary, the thesis provides a suite new approaches for salt dome detection (interpretation), new attributes for salt dome

classification, and a modified HMM model for salt dome tracking in seismic volumes.

ملخص الرسالة

الاسم: أسجد أمين

عنوان الدراسة: أسلوب آلي لاكتشاف القبب الملحية من البيانات الجيوفيزيائية الثنائية والثلاثية الأبعاد.

التخصص: الهندسة كهربائية

تاريخ المناقشة: نوفمبر 2016

ترتبط عملية تحليل البيانات السيزمية (الجيوفيزيائية) عادة بطرق تقليدية من خلال خبراء جيوفيزيائيين أو آليا باستخدام أنظمة الحاسب لاكتشاف التكوينات الجيولوجية ذات الأهمية. لهذه التكوينات العديد من التطبيقات في مجالات المسح الجيوفيزيائي كتحديد الصدوع، القباب الملحية، الأفق في الطبقات الأرضية وتراكيب جيولوجية أخرى. تقوم شركات النفط عند المسح الجيوفيزيائي بالاستفادة من انعكاسات الموجات السيزمية من الطبقات الأرضية لاكتشاف مكامن الغاز والنفط. ويعد التعيين الدقيق لموقع حقل النفط المحتمل ذا أهمية اقتصادية بالغة خصوصا عند حفر آبار التنقيب وما يتبعها من تكاليف باهظة قد تحدث عند الحفر في المكان الخاطئ. ومن أهم التراكيب الجيولوجية عند تحليل البيانات السيزمية هي القباب الملحية، والتي يرتبط تواجد الغاز الطبيعي والنفط بها. فيعتبر تحديدها خطوة رئيسية، حيث تشكل تلك القباب الملحية عازلا محكما لمكامن النفط. يتم تحديد القباب الملحية عادة عن طريق خبراء جيوفيزيائيين، حيث يتطلب تفسير البيانات السيزمية تدريبا مكثفا وخبرة طويلة في هذا المجال لتحديد موقع هذه التراكيب الجيولوجية بدقة. وتستغرق هذه المهمة الكثير من الوقت والجهد، بالإضافة لفريق عمل كبير نسبيا يحلل حجما هائلا من البيانات. ولتلافي هذه التحديات عند تحديد القباب الملحية بالطرق التقليدية، قام العديد من الباحثين مؤخرا بتطوير طرق آلية أو شبه آلية لاكتشاف القباب الملحية.

في هذه الرسالة، نقترح عددا من الطرق الآلية لاكتشاف القباب الملحية من البيانات السيزمية ثنائية وثلاثية الأبعاد. وقمنا بتطوير طريقة متعددة الاتجاهات تعتمد على اكتشاف الحافة ثلاثية البعد للقباب الملحية للتغلب على ضعف أداء الطرق التقليدية ثنائية البعد. ونقترح طريقة أخرى تعتمد على السمات التركيبية (texture attributes) والترميز اعتمادا على البيانات لزيادة فعالية تحديد القباب الملحية. كما طورنا طريقة للتصنيف تمزج السمات التركيبية مع اكتشاف الحافة. نقترح في هذه الدراسة سمات جديدة باستخدام تحليل القيمة المفردة عالية الرتبة (higher order singular value decomposition)، فيتم احتساب هذه السمات باستخدام البيانات ثلاثية الأبعاد. كذلك قمنا باقتراح طريقة تعتمد على تشكيل قاموس من خلال تصنيف وترتيب الخصائص، ويتم الترتيب باستخدام أحدث الطرق في مجال نظرية المعلومات. أخيرا، قمنا بتطوير طرق تحديد وتعقب القباب الملحية تعتمد على نموذج ماركوف المخفي (hidden Markov model) أحادي البعد. هذه الرسالة تقدم مجموعة من الطرق الجديدة المتقدمة لتحديد واكتشاف القباب الملحية، وتطوير سمات جديدة لتصنيف القباب الملحية، وطرق معدلة لنموذج ماركوف المخفي لتتبع القباب الملحية في البيانات السيزمية المتعددة الأبعاد.

CHAPTER 1

INTRODUCTION

Seismic interpretation is commonly used to describe the process of data analysis by a trained human interpreter or a computer aided system with the aim of extracting important geological information (e.g. faults, salt bodies etc.). Seismic data is generally presented in the form of an image of the different earth layers below the surface of ground. 2D seismic shows a single slice of the earth whereas 3D seismic shows a volume of earth. Fig 1.1 shows an example of 3D seismic data. The term inline here is defined as the direction in which the receiving sensors are deployed whereas crossline refers to the direction that is perpendicular to the orientation of the receiving sensors.

Seismic data is obtained through the reflection of seismic waves from the earth's subsurface. The seismic waves, transmitted by the energy source, travel down through the earth. The properties of these waves change as they propagate through rocks and fluids. The reflection of these waves, received by the surface sensors, contains important geological information which is used to identify a

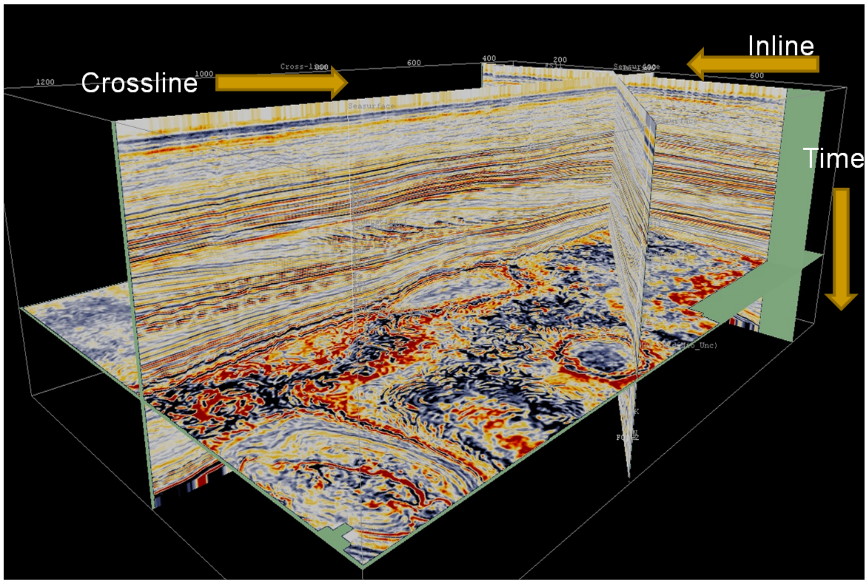

Figure 1.1: Sample 3D Seismic Data (Netherland Offshore F3 [1])

number of characteristics for the earth layers including.

- Horizons, Faults
- Structure, Structural features
- Salt and other bodies
- Fluid presence
- Traps
- Rock properties

The characterization of these features is a difficult task as the data is subjected to different types of noise and is actually a result from a combination of reflections. The noise may be i) random noise, ii) noise due to multiple reflections, or iii) noise due to refracted energy, among others. In general, we can categorize seismic noise into two main types: random noise and coherent noise. Random noise has no correlation with the neighboring channels and therefore is easier to attenuate during the pre processing stage of seismic data. Coherent noise, however, is difficult to attenuate in the preprocessing phase as it can interfere with the real signals and may appear as the part of data.

Traditionally, seismic interpretation has been carried by expert human interpreters. One of the goals is to extract important information, such as salt bodies, from the seismic data. The human interpreter, however, needs substantial training and adequate experience in order to successfully interpret seismic data. Although manual interpretation is reliable and widely used in seismic industry, the method is slow and requires a large amount of manpower. Seismic datasets used in oil and gas industry are usually of the order of tera-bytes. Therefore, it is practically impossible for a human interpreter to label such large data sets. Fully automated seismic interpretation is not feasible as it can bring with it a lot of uncertainties and inaccuracies. An alternative approach is to implement an automated interpretation with some input from an expert interpreter. This will help in improving accuracy and reducing interpretation time.

One of the most important tasks in seismic data interpretation is the detection and tracking of salt bodies as most of the important reservoirs are trapped around such bodies. Salt domes are largely subsurface geologic structures that consist of cylinders of salt (Fig. 1.2). Major accumulations of oil and Gas are associated with salt domes. This is primarily due to excellent sealing capabilities of salt domes. Salt dome detection is a difficult and time consuming task especially in case of 3D seismic volumes. Traditional amplitude based detection schemes often mix between local discontinuities and amplitude variations. Though the reflections from salt boundaries have often high amplitudes, there is still a good chance that an amplitude-based scheme may give inaccurate detection results. In order to improve the results, manual editing is often needed. This manual editing can take many hours depending upon the size of the dataset and the available man power. Another option is to use some kind of normalization technique to reduce amplitude variations. Other machine learning based techniques such as artificial neural networks can also be used. Artificial neural networks are less affected by amplitude variations and therefore provide more accurate salt boundaries.

Over the last few years, image segmentation methods have attracted considerable attention from the geophysics community. Image segmentation schemes such as edge-based segmentation, graph-cuts, active contours, texture-based classification, etc. are shown to work well for salt boundary detection and provide an efficient alternative to manual labeling of salt domes. Most of such schemes proposed in the literature use amplitude as the only attribute [2], [3]. Although amplitude is an important attribute and helps greatly in detecting salt boundaries, using only one attribute can easily effect the accuracy of the segmentation process. Other commonly used attributes are texture-based attributes computed from 2D seismic data [12], [8]. To develop a more robust segmentation algorithm, it is essential to investigate other important seismic attributes extracted from 2D and 3D data.

Seismic attributes play a key role in the interpretation process. A good seismic attribute is the one which is directly sensitive to the desired geologic feature or reservoir property of interest. These attributes have long been used in exploration processes even when there were no digital recordings available. Seismic attributes can reveal texture differences between salt areas and surrounding geology more robustly when compared to edge based attributes. A salt structure can be defined as an area of incoherent texture compared to its surroundings. While, numerous attributes [12], [13], [14] have been proposed in the literature, very limited efforts have been put in identifying and ultimately ranking such attributes with respect to the task of interest; that is accurate salt dome detection or as a matter of fact the detection of other important events in seismic data.

State-of-the-art classifier-based salt dome detection approaches [12], [8] have traditionally used Bayesian classifiers for training and detection. Although the Bayesian classifier based approaches provide good results, it is important to investigate other approaches such as data-driven models, dictionary-based classifier, the fusion of classifiers, etc. to improve the accuracy of delineation process. These approaches have shown superior results over traditional Bayesian classification models in many image processing applications.

The main focus of this thesis is to develop a suite of computer-aided algorithms for salt dome detection in 2D and 3D seismic data. We start by providing a comprehensive study of different existing seismic attributes and approaches used for

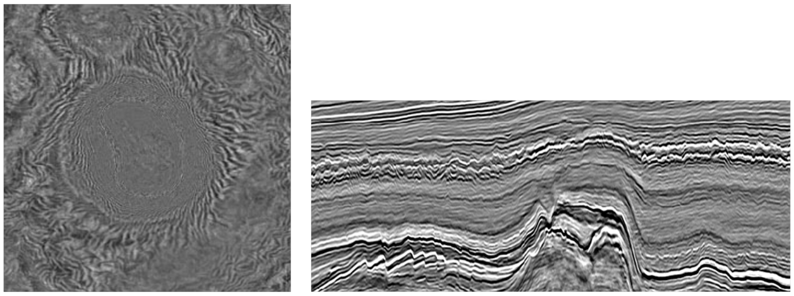

(a) (b)

Figure 1.2: Salt dome examples (a) North Sea (b) Netherland Offshore F3 [1]

salt dome detection. The work then follows by presenting the development of automated salt dome classification models using edge and texture based attributes, development of new powerful seismic attributes for salt dome classification, development of robust classification model using information theoretic approach, and development of a salt dome detection and tracking approach using context-based model. A number of contributions have been made under each of these categories.

1.1 Research Objectives

Salt dome detection is considered a challenging problem as the data received from earth's subsurface is affected by many factors such as seismic noise, multiple reflections, etc. Therefore it is important to develop powerful seismic attributes and automated approaches for accurate detection of salt bodies in migrated seismic surveys. In this thesis, we focus on the development of seismic attributes relevant to the salt dome detection problem and robust approaches for salt dome segmentation. In summary, we list below the main objectives of the thesis:

- To propose a 3D multidirectional edge detection method for salt dome detection.

- To propose a hybrid approach for salt dome detection using edge and texture based attributes.
- To propose a data driven model (codebook) using texture-based attributes to delineate salt boundaries in 2D seismic data.
- To develop a ranking scheme to create an optimal set of seismic attributes with relevance to the problem of salt dome detection.
- To develop new seismic attributes, computed from 3D data, for salt dome detection and tracking.
- To propose a robust dictionary-based classification approach using the above mentioned attributes for salt dome detection.
- To propose the hidden markov model approach for salt boundary detection and tracking in 2D and 3D surveys.
- To evaluate the performance of the proposed methods using the standard Netherlands F3 Block and compare the results to existing techniques.

1.2 Major Contributions

The main contributions of the thesis are:

- Development of a new approach for salt dome detection using a 3D multi-directional edge detector [15].

- Development of a hybrid approach for salt dome detection in 2D and 3D seismic data using edge and texture based attributes [9].
- Development of a Codebook-Based Learning Model for salt dome detection [16]
- Development of feature ranking approach for texture-based attributes using information theoretic algorithms [17].
- Development of a new texture attributes for salt dome detection and tracking using the concept of Higher Order Singular Value Decomposition (HOSVD).
- Development of an automated salt dome detection algorithm using an attribute ranking framework with a dictionary-based classifier [10], [1].
- Development of a novel approach for salt dome detection and tracking in seismic surveys using a Hidden Markov Model [18].
- Development of LRI-based features for seismic retrieval scene labeling applications [19]

1.3 Thesis Organization

The rest of the thesis is structured as follows:

Chapter 2 provides an extensive literature review of existing approaches for salt dome detection, segmentation results produced by these approaches for different seismic data, critical analysis and limitations of existing approaches.

---

[1] Extended version submitted to Interpretation Journal (Minor revision)

Chapter 3 provides a detailed review of existing seismic attributes used for salt dome classification. These include edge-based, GLCM-based, covariance matrix based, Gabor filter based, and LRI-based attributes. In addition to the formulation of these attributes, we have also shown the maps produced by these attributes and their relevance to different interpretation applications.

Chapter 4 provides the details of new approaches proposed for salt dome detection using existing edge and texture based attributes. These approaches include multidirectional 3D edge detection for salt dome detection in 3D data, data driven codebook based model using texture attributes, a hybrid approach using the fusion of edge and texture based classifiers. In addition to these approaches, we also introduce new HOSVD-based attributes to overcome the limitations of existing texture-based attributes.

Chapter 5 introduces the dictionary-based classification model using the HOSVD based attributes for salt dome detection. This model also include an information theoretic approach for feature ranking.

Chapter 6 provides the details of hidden markov model based technique for salt dome detection and tracking. The parameter estimation, context-based modeling, etc. for HMM are discussed in detail.

Finally, we conclude the thesis in Chapter 7 and provide a discussion on future research perspectives.

CHAPTER 2

LITERATURE REVIEW

One of the most important tasks in seismic data interpretation is the detection of salt bodies as reservoirs are trapped around these salt bodies. Salt domes are an important diapir shaped structures in the Earth subsurface that have excellent sealing capabilities and contain hints about major accumulations of petroleum and gas reservoirs. Therefore, determining the accurate location of salt domes within migrated seismic volumes is one of the key steps in the exploration projects. However, with the increasing size of acquired seismic volumes, manual interpretation of salt domes is becoming extremely time consuming and labor intensive. Therefore, to overcome this laborious task, researchers in academia and industry have proposed several fully- and semi-automated algorithms for detecting salt bodies within seismic volumes. Over the last few decades, researchers have proposed several edge-based, texture-based, hybrid (edge and texture), normalized cuts, active contour, and patch-based classification methods for salt dome delineation. These methods can be categorized as:

- Salt Dome detection using Edge based methods
- Salt Dome Detection using Graph-based segmentation
    - Salt Dome Detection using Normalized Cuts
    - Salt Dome detection using Pairwise Region Comparison
- Salt Dome Detection using active contours-based methods
    - Salt Dome detection shape deformation technique
    - Salt Dome detection using Level Set Method
- Salt Dome Detection using Clustering Methods
- Salt Dome detection using texture based attributes

In figure 2.1, we show the categorization of salt dome detection methods from 2D and 3D seismic data. We will now discuss each of these methods in more details.

2.1 Salt Dome Detection using Edge-based Methods

Edge detection is one of the most important image processing tasks used to detect pixels intensity variations in an image. Edge detection can be used for the accurate estimation of dissimilarities caused by faulting or stratigraphic variations. Therefore, edge detection based techniques are really useful in detecting

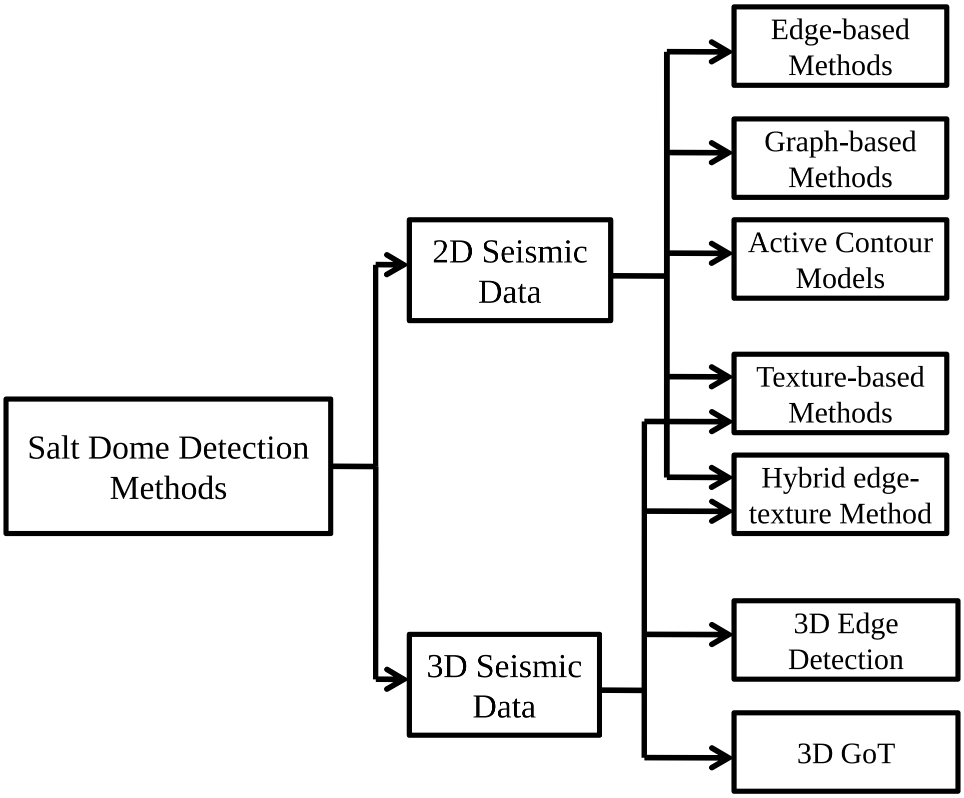

Figure 2.1: Salt dome detection methods from 2D and 3D seismic data

salt dome boundaries in seismic data. Sobel edge detector, which computes the first derivative, is the most common operator used in the detection of salt domes.

Jing et al., in [2], proposed a salt boundary detection technique based on the Sobel filter. The Sobel operator is used to calculate the first order derivative in both the inline and crossline directions. The average of these two measurements is then used for salt boundary detection.

In [2], a more general form of the Sobel algorithm was implemented by applying masks with different weights and then combining the weighted samples. The combined samples give information about the dissimilarities in an image along any direction. In the case of the 2D Sobel operator, the first mask detects discontinuity in one direction and the second mask detects dissimilarity in the other direction.

The boundary of the salt dome is tracked by combining the two dissimilarity maps. Moreover, this algorithm can also help in determining the thickness of salt layers and the depth of domes. Sobel gradients in the x and y direction are given as:

$$G_x = \begin{bmatrix} -1 & 0 & 1 \\ -2 & 0 & 2 \\ -1 & 0 & 1 \end{bmatrix} \tag{2.1}$$

$$G_y = \begin{bmatrix} -1 & -2 & -1 \\ 0 & 0 & 0 \\ 1 & 2 & 1 \end{bmatrix} \tag{2.2}$$

This simple method was able to detect salt boundaries with good accuracy. Since there is no normalization technique used, the scheme works well only when seismic data exhibits small amplitude variations. Figure 2.2 shows some of the results from [2].

Aqrawi et al., in [3], proposed a salt body detection algorithm based on a 3D Sobel edge detector. The Sobel filter is combined with amplitude normalization and dimension weighting. The normalization minimizes the variations between low and high amplitudes. The weighting, here, is used to avoid the horizontal artifacts that may appear due to vertical gradient.

The scheme starts by estimating the structural dip that maximizes trace to trace correlation. The second step is to compute the discontinuities using the

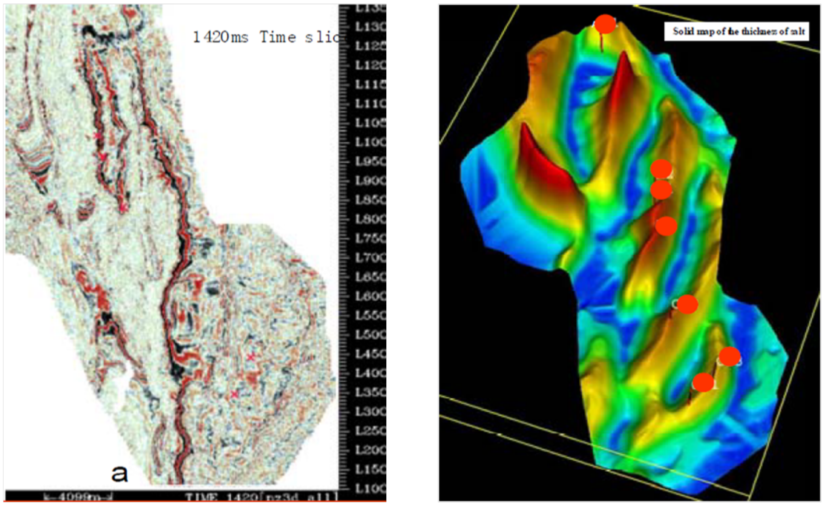

(a) (b)

Figure 2.2: (a) Seismic data, (b) Estimated salt body shape using the 2D Sobel filter (Images taken from [2])

dip. The third step involves the 3D sobel edge detector. The operator size used here is 3 × 3 × 3. 3D sobel edge detector with normalization elaborates the salt bodies even if the seismic data has small amplitude variations. Figure 2.3 shows the original seismic data and the detected salt bodies.

Other edge detection based techniques such as Prewitt edge detector [20] can also be used to detect salt boundaries. Like Sobel operator, Prewitt operator is also a first order edge operator but with different kernels. The Prewitt gradients in the x and y direction are given as:

$$G_x = \begin{bmatrix} -1 & 0 & 1 \\ -1 & 0 & 1 \\ -1 & 0 & 1 \end{bmatrix} \tag{2.3}$$

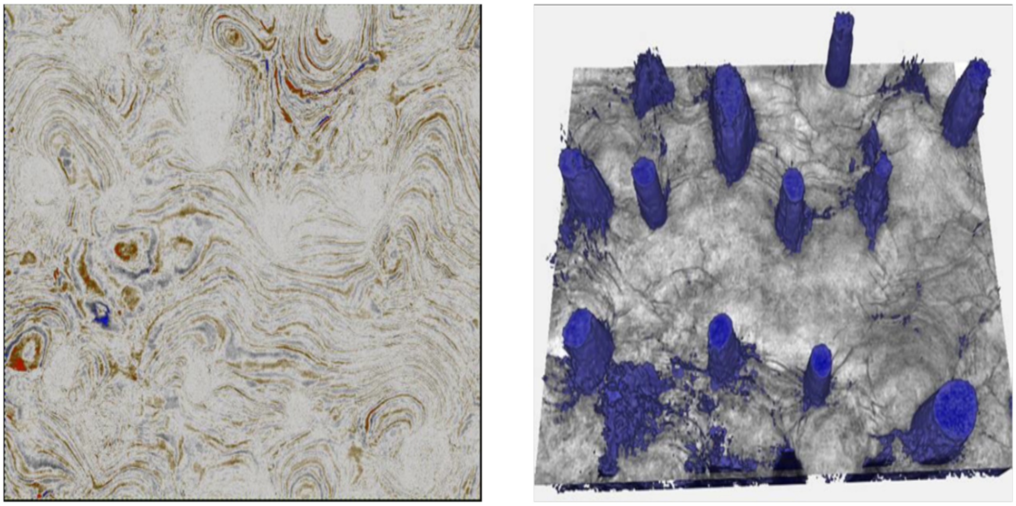

(a) (b)

Figure 2.3: (a) Seismic data, (b) Estimated salt boundaries using the 3D Sobel filter (Images taken from [3])

$$G_y = \begin{bmatrix} -1 & -1 & -1 \\ 0 & 0 & 0 \\ 1 & 1 & 1 \end{bmatrix} \tag{2.4}$$

The Canny edge detection technique [21], which is widely considered as an optimal edge detection technique, can also be used to detect salt bodies in seismic data. The Canny edge detector uses a blurring operation to remove noise from the image before computing the edges.

However, edge detection based segmentation algorithms are very sensitive to the noise present in seismic data. Such schemes often confuse between local discontinuities and amplitude variations. In case of large amplitude variations, these techniques fail to provide a refined salt dome boundary.

2.2 Salt Dome Detection using Graph-based Segmentation

Graph-based segmentation methods are commonly used in many image processing applications. These segmentation techniques do not rely on local discontinuities and therefore calculate an optimal partition of the entire image. A number of such algorithms are used in image processing, but not all are suitable for seismic images. The Normalized Cuts Image Segmentation (NCIS) and Pairwise Region Comparison (PRC) methods are shown to work well with seismic images, therefore they are used in seismic interpretation for salt dome detection.

2.2.1 Salt Dome Detection using Normalized Cuts

Normalized Cuts Image Segmentation (NCIS) [22] provides an optimal way of detecting salt domes. For 3D seismic data, the NCIS detects the salt domes by solving a global optimization problem, and therefore is less sensitive to local discontinuities. The NCIS extracts global impressions from an image and does not focus on the local features. Global impression is helpful in forming the groups of pixels. These groups are based on some pre defined criterion e.g. foreground and background pixels can be separated into different groups. For 3D seismic data, the NCIS was first used to paint 3D atomic meshes [23][24]. Subsequently, the method was applied to the problem of detecting salt boundaries in [25][26] [27].

Lomask et al. in [4] used the NCIS method to partition seismic images along the salt boundaries. The proposed method implements a weight matrix to indicate the presence of a boundary between pairs of pixels (nodes) in the seismic image. Each node is assigned a weight with every neighboring node based on some selected attributes. A low value is assigned to a pair if the attribute indicates that a salt boundary exists between the two nodes. Once the optimum weights are assigned, the next step is to determine the optimum partition. The optimum partition is found here using the NCIS technique.

To detect the salt domes, the NCIS is used to segment the seismic image into two regions i.e. i) Salt region, and ii) Outside the salt region. The separating curve between the two regions is the salt boundary. Using the weight matrix **W**, the NCIS finds the cut that partitions the image into two groups, A and B, by minimizing the normalized cut:

$$N_{cut} = \frac{cut}{total_A} + \frac{cut}{total_B} \tag{2.5}$$

where cut is the sum of the weights cut by the partition, $total_A$ is the sum of all weights in Group A, and $total_B$ is the sum of all weights in Group B.

The estimation of a boundary path across a seismic image may be expressed as an eigenvector problem which can be set up via the Rayleigh quotient

$$min_y \frac{\mathbf{y^T(D\text{-}W)y}}{\mathbf{y^T Dy}} \tag{2.6}$$

where **y** is the eigenvector, and **D** is a diagonal matrix. The elements of **D** are the sum of each column of **W**. The constraint introduced here is.

$$\mathbf{y}^T\mathbf{D}1 = 0 \tag{2.7}$$

where **1** is the vector with all ones. Using the constraint introduced on the Rayleigh quotient, the problem can be written as the generalized eigenvalue problem.

$$(\mathbf{D}\text{-}\mathbf{W})\mathbf{y} = \lambda\mathbf{D}\mathbf{y} \tag{2.8}$$

where λ is the eigenvalue. The values of eigenvector across the boundary ranges from -1 to 1.

The scheme was tested on the Gulf of Mexico dataset. Figure 2.4 shows the results of this scheme. The computation of weight vector for 3D data is a time consuming process. The algorithm also underperforms when the reflectors on the salt boundary are weak.

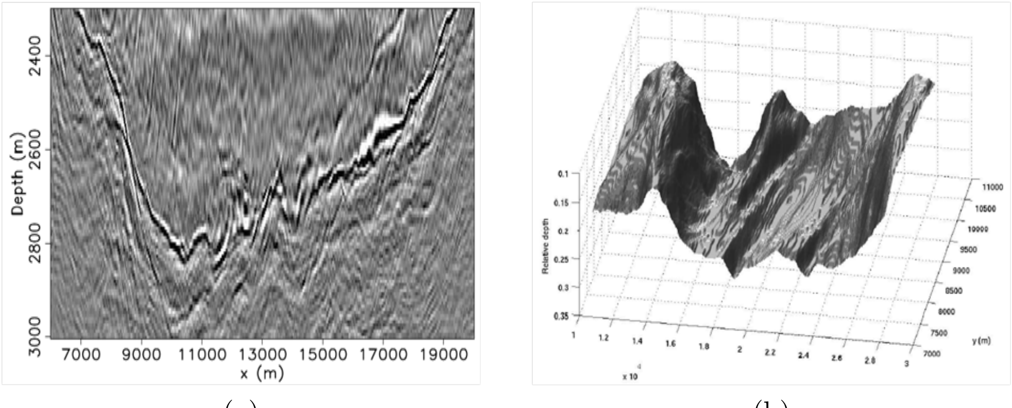

(a) (b)

Figure 2.4: (a) Seismic data, (b) Estimated salt boundaries using the NCIS (Images taken from [4])

Halpert et al., in [28], extended the work of Lomask and others. They used the NCIS technique presented in [4] to construct and update the iterative velocity model. NCIS is combined with a sediment and a salt flooding migration technique and the optimum boundary is calculated by solving a non-linear optimization problem. The initial salt body is calculated and used as a prior information to update the velocity model. The prior information about salt boundary helps in producing an improved velocity model.

The most basic NCIS algorithm relies only on a single attribute i.e. amplitude. This single attribute often detects salt boundary with good accuracy. However, in some cases, such a single attribute fails to produce the desired results. Halpert et al. in [5] used the NCIS algorithm with three attributes i.e. amplitude, dip variability and instantaneous frequency. Attributes such as dip, and frequency can provide valuable information relevant to the segmentation problem. Dip variability [29] is an important attribute that can be used to measure similarity within the seismic image. Therefore, incorporating dips is shown to increase the accuracy of salt boundary segmentation. Frequency content of a seismic image also offers an improvement in the accuracy of the detected salt body. These attributes are combined using a method that takes into account uncertainty at each boundary location and provides better results to those using a single attribute only.

In case of a single attribute, the NCIS algorithm assumes that the salt boundary is defined by a strong reflector. This is true for some cases but in most of the cases, due to amplitude variations along the salt boundary, the above assumption does not hold. This creates an uncertainty problem which can be solved using information from multiple attributes. Figure 2.5 show the results of this segmentation scheme.

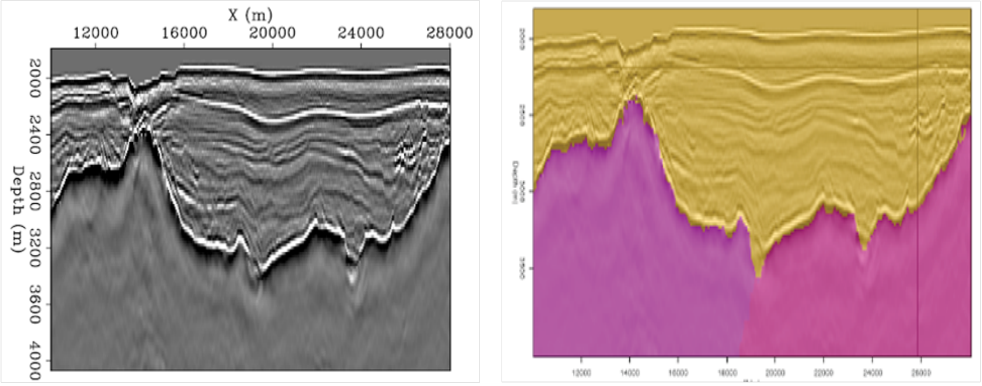

(a) (b)

Figure 2.5: (a) Seismic data, (b) Estimated salt boundaries using the extended NCIS (Images taken from [5])

2.2.2 Salt Dome Detection using Pairwise Region Comparison

The NCIS is the most commonly used global image segmentation scheme for seismic data. However, this scheme is computationally inefficient as it requires a lot of preprocessing and prior information about the boundary. In absence of any prior information, NCIS can be computationally very expensive.

In [6], a Pairwise Region Comparison (PRC) method based on [30] was used for salt interpretation. This method operates on full seismic image and is computationally more efficient than the NCIS technique. PRC has a running time of O(NlogN) as compared to NCIS which has a running time of O(N^2) where N is the number of pixels in an image. The PRC algorithm discussed in [30] falls under the category of graph-based image segmentation. Graph-based image segmentation methods use the concept of minimum spanning trees [31]. The PRC algorithm uses pixel to pixel comparison to determine whether the pair belongs to the a certain partition or not. In [6], the PRC method is used to provide two possible interpretations of seismic image. A fast image update scheme is then used to examine the changes as a result of the two interpretations.

Although it is time consuming to interpret the large salt bodies manually, still we should not rely totally on automatic salt boundary segmentation as sharp velocity contrast makes it really difficult to interpret salt bodies accurately. Therefore, human interpreters can help in achieving better accuracy. A balance is needed between the interpreters role and the segmentation algorithm so that the process does not become too slow and the desired level of accuracy is also achieved. In [32], a manual 2D interpretation is used to initiate an automatic 3D segmentation. Another alternative is to use human interpreters to chose from multiple interpretation provided by an automatic segmentation scheme.

The PRC image segmentation algorithm can automatically detect salt boundaries in seismic images. However, in areas where salt interpretation is uncertain, human expertise is needed to chose from two or more possible interpretations. Halpert in [6] takes input from human interpreters and combines it with pairwise region comparison (PRC) image segmentation algorithm to pick salt bodies on seismic images. A Fast image updating scheme is then used to determine the effect of different salt interpretations given by the PRC algorithm. Figure 2.6 shows some of these results.

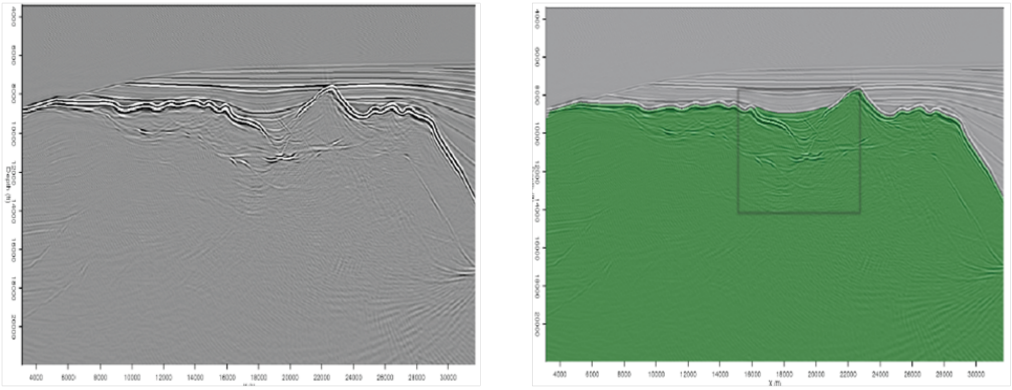

(a) (b)

Figure 2.6: (a) Seismic data, (b) Estimated salt boundaries using the PRC (Images taken from [6])

2.3 Salt Dome Detection using Active Contours

Salt boundary segmentation methods introduced by [33], [7], and and [34] are based on the active contour models (ACM), which combine the interpreter's input with automated segmentation. The initial boundary information is provided by a geophysics expert and based on an initial estimate, the ACM models iteratively optimize the cost function to yield a salt-dome boundary.

2.3.1 Salt Dome Detection using Shape Deformation Technique

Accurate interpretation of salt bodies is essential to build an accurate velocity model. Boundary tracking algorithms often fails to give the desired salt boundary.

Zhang et al. in [33] proposed a salt boundary segmentation method based on shape deformation technique. This scheme combines the expert interpreter input with the automatic segmentation scheme.

In this method, the initial boundary information is provided by a human expert. The new boundary in successive time slices is extracted based on the initial information. It is assumed that in successive slices, the salt boundary will deform within a specific limit [35]. A reference seismic image that has been labeled accurately by the human interpreter is available. The segmentation result in the reference image is characterized by a contour. The contour on the reference image is represented by a set of points, $V = v_1, v_2, ..., v_n$ where $v_i = (x_i, y_i)$. For each point v_i, the algorithm identifies a set of possible points $B_i = v_i(j), j = 1, 2, ..., ni$ on the input image, where $v_i(j) = (x_i(j), y_i(j))$. The shape deformation technique consists of the following steps.

1. Identify the best point v_i' from the set B_i such that $V' = v_1', v_2', , v_n'$ is located in or near the true object boundary in the input image.

2. Deform the prior shape V to match the new set V' while keeping the general characteristics of prior shape .

2.3.2 Salt Dome Detection using the Level Set Method

Automated salt body extraction algorithms[36], discussed so far, do not consider the existence of sediments within the salt body. An efficient automated algorithm should consider and segment there sediments. In most of the cases, the task of separating sediments from the salt bodies is carried by a human interpreter. It is hard to design an automated algorithm for this task as it involves complex geometry. In [7], an automated salt body extraction scheme based on level set method [37][38] is presented. The technique is designed to carry out segmentations within the salt bodies. The level set method describes the motion of an object boundary subject to forces. In case of seismic data, the object is a salt body represented by positive voxels while negative voxels represent the outside of the salt body. An expert human interpreter can be asked to provide the initial set of salt voxels. An advantage of the level set method is that it can easily follow the objects that change topology. The level set method was first used in seismic for interactive visualization and interpretation of geobodies [39].

The automated salt body extraction scheme presented in [7] introduces a local stop criterion. The regions, where a salt boundary has been found without any uncertainty, are omitted from further evolution. this can help in speeding up the detection process. Also it can help in highlighting the parts that require further investigation. Figure 2.7 shows one iteration of level set. The technique was applied on 3D seismic volume from Gulf of Mexico.

In [34], active contour model using edge function was proposed. The model iteratively segments the salt boundary using energy minimization function based on the edge strength. This method was applied to the F3 offshore block and the results were encouraging. However, providing an initial estimate of salt dome and designing a cost function is time consuming and requires input from interpreter

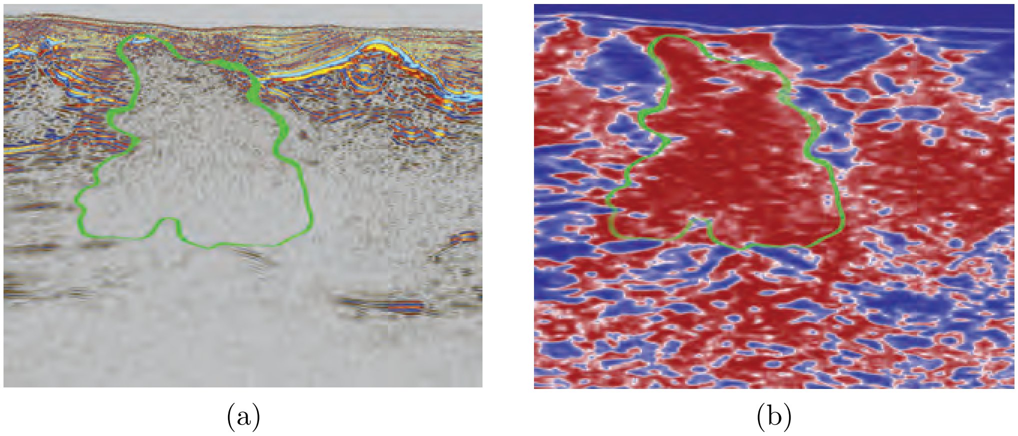
(a) (b)

Figure 2.7: (a) Slat body labeled by interpreter, (b) One iteration of level set method (Images taken from [7])

at each seismic inline sections.

2.4 Salt Dome Detection using Clustering Methods

There are many image segmentation algorithms that can be used for seismic data. The most basic segmentation techniques are the pixel-based algorithms. In the case of seismic data, pixel-based segmentation is simple to implement as it only requires thresholding the amplitudes. Although the scheme is simple and computationally efficient, it is really difficult to compute the optimal value of the threshold. Therefore, such schemes may work well for some slices but can also behave inconsistently for other cases.

Traditional amplitude based detection schemes often confuse between local discontinuities and amplitude variations. To avoid such inconsistency, globally optimized pixel based segmentation algorithms [40] are used. K-means clustering

[41] can also be used to partition seismic images into two groups i.e. salt region and outside. The accuracy of this method depends upon the attributes selected. The partitions is accurate when the attributes have significantly different values inside the salt region from outside. This is not always true when the only attribute selected is instantaneous amplitude.

Stochastic clusters based techniques [42] [24] overcome the above problem by iteratively combining the adjacent nodes probabilistically. The probability between a node and its neighbor depends on the chosen attributes. The stochastic cluster methods can successfully segment the seismic image into groups, the groups can be more than two.

2.5 Salt Dome Detection using Texture-based Attributes

Salt boundaries are often characterized by changes in texture rather than reflectivity. Therefore, using only boundary-sensitive attributes such as instantaneous amplitude may result in incorrect interpretation of salt bodies. Salt dome detection methods based on texture attributes are proposed by [43], [8], and [44]. Berthelot et al. in [12] uses the texture-sensitive attributes in addition to the boundary-sensitive attributes. The algorithm discussed in [12] extracts some selected texture attributes from the seismic data and then uses these attributes to train a classifier. The classifier estimate the probability of each pixel in the seismic image. A graph-cut segmentation algorithm [45] use these probabilities to segment the desired salt boundary. The accuracy of the salt boundary is directly linked to the selected texture attributes. A salt structure can be defined as an area of incoherent texture compared to its surroundings. Attributes derived from the covariance matrix, such as chaos and trace [46] [47] [48] can assist in detecting the salt boundary.

Other techniques that focus on extracting multiple seismic attributes are discussed in [13][14]. Barthelot et al. in [8] presented some new texture based features for salt dome detection. The authors investigated some more texture based characteristics of seismic data. Three different texture groups were considered in [8]: i) Gray-level co-occurrence matrix (GLCM) attributes, ii) frequency-based attributes, and iii) dip and similarity attributes.

The gradient of texture (GoT) method for salt dome detection, recently introduced by [11] and [49] measures the texture dissimilarity between two neighboring cubes and windows, respectively, to detect the salt-dome boundaries. However, the challenge with texture-based schemes is to obtain the most important attributes, which not only represent texture information but are also computational less expensive.

CHAPTER 3

SEISMIC ATTRIBUTES FOR SALT DOME DETECTION

Seismic interpretation is commonly used to describe the process of data analysis by either a trained human expert or a computer aided system, with the aim of extracting important geologic features.Such features are then used in different seismic applications such as detection of faults, salt domes, horizons, etc.. Historically, seismic interpretation has been carried by human experts. Human interpreters, however, need extended training and experience to perform this task accurately and continuously. Moreover, manual (or subjective) methods are slow, require a large amount of manpower, and can be affected by human fatigue, among other factors. To alleviate the challenges of human interpretation of seismic data, we witnessed, in recent years, substantial research efforts put in developing automated or semi-automated seismic interpretation systems. The success of such systems relies heavily on the robustness of the different attributes extracted from the data, then the use of such attributes for the purpose of classification, decision making, detection of faults, salt domes, etc,...

Seismic attributes play a key role in the interpretation process. A good seismic attribute is the one which is directly sensitive to the desired geologic feature or reservoir property of interest.Seismic attributes have long been used in exploration processes even when there were no digital recordings made. The first seismic attribute used in oil exploration was the NR (zones of no reflection) attribute [50]. This attribute was used to estimate faults in analog recording of seismic data. With the introduction of magnetic analog recordings, geologists were able to compute important seismic attributes including: structural elevation, reflectors dip, and discontinuities, among others. Reflectors dip and structural elevation were used in estimating hydrocarbon traps while the discontinuity attribute was used to highlight faults [50].

Digital recording of seismic data was introduced in 1960's. It was noted that reflections from hydrocarbon charged rocks showed large amplitudes as compared to their surroundings. This large amplitude was named as a "bright spot". Bright spots were extensively used to detect gas reservoirs [51]. Seismic attributes such as amplitude, flat spots, and frequency loss were used to identify the "bright spot" in digital seismic data.In the 1970's, three additional attributes, instantaneous amplitude, instantaneous phase, and instantaneous frequency, derived from trace analysis, were introduced for seismic interpretation. Instantaneous amplitude and frequency were used to estimate the presence of hydrocarbons.Instantaneous phase, on the other hand, was used to label faults in seismic data. Later on, some new attributes: dominant frequency, average amplitude, and zero-crossing frequency, were used to improve the accuracy of hydrocarbon and fault estimation.

Trace attributes suffer from waveform interference and therefore are greatly affected by reflections from neighboring surfaces. To overcome these limitations, curvature maps from 3D seismic data and texture attributes from 2D and 3D seismic data were proposed [52].The curvature attribute is used to estimate regional dip and small-scale features that are associated with open fractures and fault depth.The idea of applying texture-based attributes to seismic applications gained more popularity over the last decade or so. In particular, attributes derived from the Gray Level Co-occurrence Matrix (GLCM) were used for detecting salt domes, faults, etc.

In recent years, a number of 2D and 3D attributes were proposed for detecting salt domes. These attributes can broadly be classified as i) Space domain attributes, ii) Frequency domain attributes. In Figure 3.1, we show the grouping of seismic attributes used for salt dome detection. We will now discuss each of these attributes in more details.

3.1 Space Domain Attributes

Space domain attributes are effective and simple to implement. These attributes are widely used in seismic interpretation for detecting salt bodies from 2D and3D seismic data. The most common space domain attributes are:

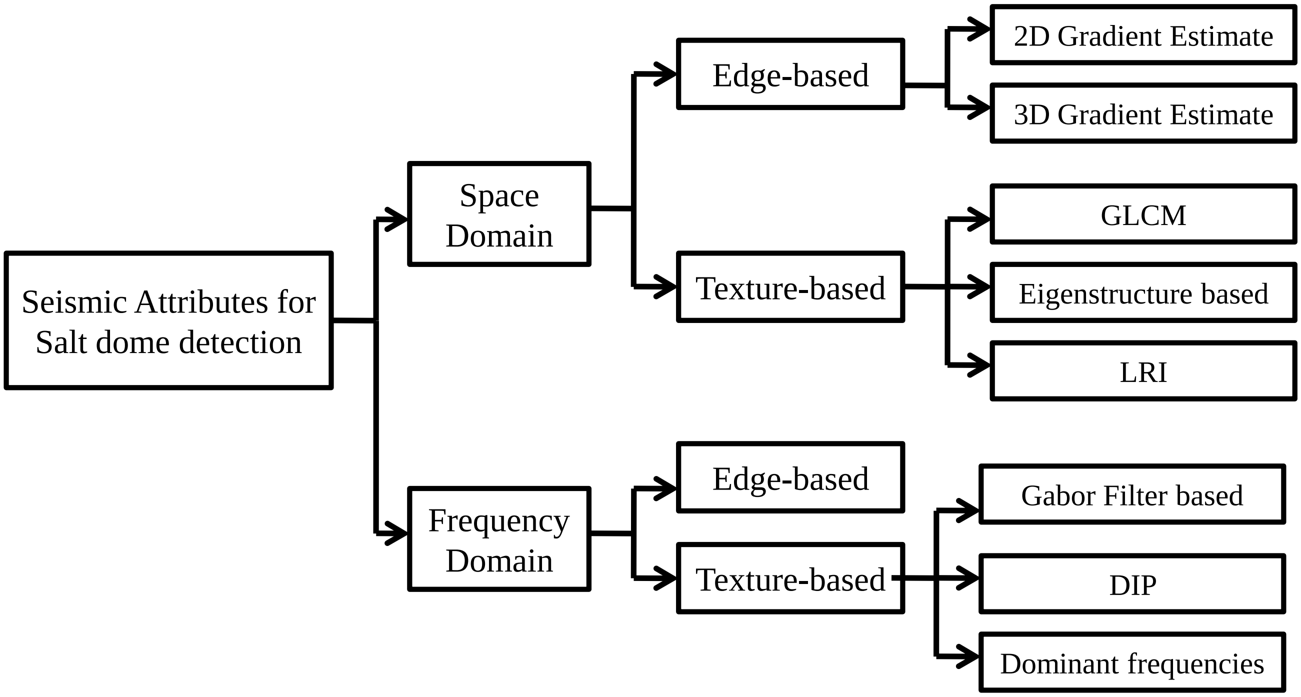

Figure 3.1: Seismic attributes for salt dome detection

3.1.1 Gradient Attributes

3.1.2 The 2D Gradient Estimate

Edge detection is one of the most important image processing tasks used to detect pixels intensity variations in an image. Edge detection can be used for the accurate estimation of dissimilarities caused by faulting or stratigraphic variations. Therefore, edge detection based techniques are really useful in detecting faults, salt dome boundaries, and horizons in seismic data. The Sobel edge detector, which uses the first derivative, is the most common operator used in the detection of salt domes. The Sobel operator is a differentiation operator which computes the gradient of the image intensity function. The Sobel edge detector in 2D computes spatial gradients of a 2D image and enhances regions of high frequency that represent edges. The convolution operators for the Sobel edge detector in the x direction and y directions are given as:

$$G_x = \begin{bmatrix} -1 & 0 & 1 \\ -2 & 0 & 2 \\ -1 & 0 & 1 \end{bmatrix} \tag{3.1}$$

$$G_y = \begin{bmatrix} -1 & -2 & -1 \\ 0 & 0 & 0 \\ 1 & 2 & 1 \end{bmatrix} \tag{3.2}$$

From the above formulation, we note that the first mask detects discontinuities in one direction and the second mask detects discontinuities in the other direction. The magnitude of the total gradient is now computed as:

$$G = \sqrt{{G_x}^2 + {G_y}^2} \tag{3.3}$$

Other edge detection based techniques such as the Prewitt edge detector ([20]), and the Scharr edge detector can also be used for seismic interpretation. Like the Sobel operator, the Prewitt operator is also a first order edge operator but using different kernels. The Prewitt gradients, in the x and y directions, are given as:

$$G_x = \begin{bmatrix} -1 & 0 & 1 \\ -1 & 0 & 1 \\ -1 & 0 & 1 \end{bmatrix} \tag{3.4}$$

$$G_y = \begin{bmatrix} -1 & -1 & -1 \\ 0 & 0 & 0 \\ 1 & 1 & 1 \end{bmatrix} \tag{3.5}$$

while the Scharr gradients, in the x and y directions, are given as:

$$G_x = \begin{bmatrix} -1 & 0 & 1 \\ -3 & 0 & 3 \\ -1 & 0 & 1 \end{bmatrix} \tag{3.6}$$

$$G_y = \begin{bmatrix} -1 & -3 & -1 \\ 0 & 0 & 0 \\ 1 & 3 & 1 \end{bmatrix} \tag{3.7}$$

3.1.3 The 3D Gradient Estimate

For 3D seismic data, the Sobel operator on 2D slices is extended to 3D taking into account continuity in the medium. In the case of the 3D Sobel operator, the first mask detects discontinuity in the x direction, the second mask detects dissimilarity in the y direction, and the third mask detects dissimilarity in the z direction. The boundary of the salt dome is tracked by combining the three dissimilarity maps into a single magnitude map. The convolution operator for 3D Sobel edge detector in the x direction, y direction, and z direction is given as:

$$G_x(:,:,-1) = \begin{bmatrix} -1 & 0 & 1 \\ -2 & 0 & 2 \\ -1 & 0 & 1 \end{bmatrix} G_x(:,:,0) = \begin{bmatrix} -2 & 0 & 2 \\ -4 & 0 & 4 \\ -2 & 0 & 2 \end{bmatrix} G_x(:,:,1) = \begin{bmatrix} -1 & 0 & 1 \\ -2 & 0 & 2 \\ -1 & 0 & 1 \end{bmatrix} \tag{3.8}$$

$$G_y(:,:,-1) = \begin{bmatrix} -1 & -2 & -1 \\ 0 & 0 & 0 \\ 1 & 2 & 1 \end{bmatrix} G_y(:,:,0) = \begin{bmatrix} -2 & -4 & -2 \\ 0 & 0 & 0 \\ 2 & 4 & 2 \end{bmatrix} G_y(:,:,1) = \begin{bmatrix} -1 & -2 & -1 \\ 0 & 0 & 0 \\ 1 & 2 & 1 \end{bmatrix} \tag{3.9}$$

$$G_z(:,:,-1) = \begin{bmatrix} -1 & -2 & -1 \\ -2 & -4 & -2 \\ -1 & -2 & -1 \end{bmatrix} G_z(:,:,0) = \begin{bmatrix} 0 & 0 & 0 \\ 0 & 0 & 0 \\ 0 & 0 & 0 \end{bmatrix} G_z(:,:,1) = \begin{bmatrix} 1 & 2 & 1 \\ 2 & 4 & 2 \\ 1 & 2 & 1 \end{bmatrix} \tag{3.10}$$

The resulting magnitude of the total gradient is obtained as:

$$G = \sqrt{{G_x}^2 + {G_y}^2 + {G_z}^2} \tag{3.11}$$

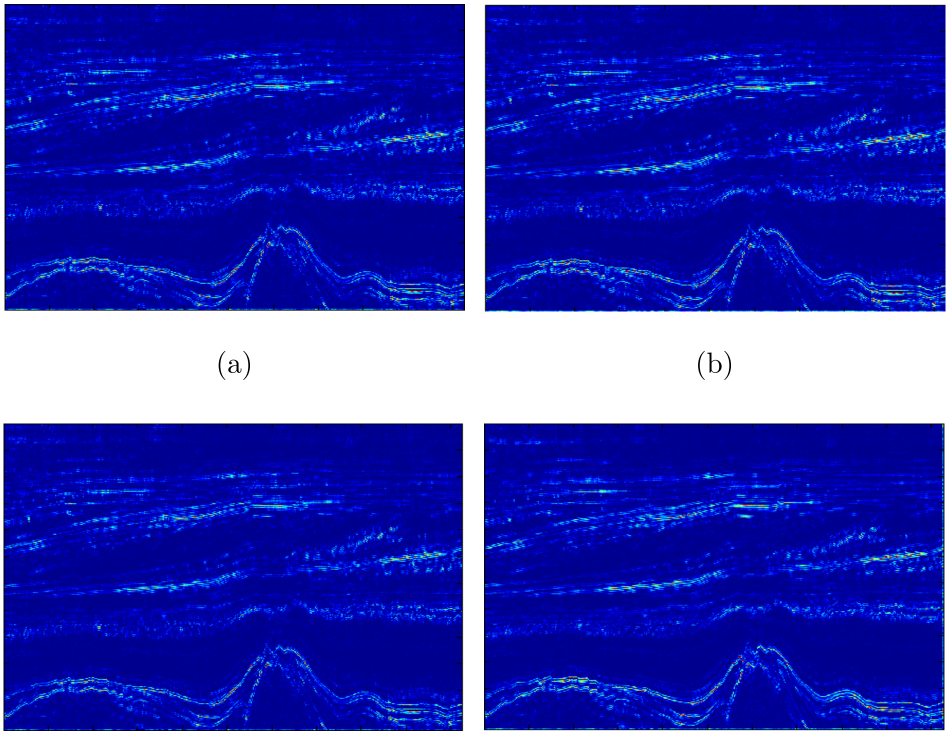

(a) (b)

(c) (d)

Figure 3.2: 2D gradient map: (a) Sobel, (b) Prewitt, (c) Scharr; (d) 3D Sobel map

3.1.4 Grey Level Co-occurence Matrix (GLCM) Attributes

The GLCM based attributes were firstly discussed by [53] and has major applications in texture analyis and texture classification. The GLCM approximates the joint probability distribution of two gray levels in an image. These attributes can detect the changes in texture among a pair of pixels in a chosen direction and pixel neighborhoods. The high values away from the diagonal in a GLCM reveal sharp gray level changes whereas the high values close to the diagonal reveal small variations in gray levels.

For an 8-bit gray scale image, $\big[I\big]$, of dimension $M \times N$, where $I(x, y)$ represents intensity within a range $[0, L-1]$ at location (x, y). We consider $L = 256$ for gray scale images. The co-occurrence matrix of intensity values, $\big[C\big]$, is calculated using the relation defined as:

$$C_{d,\theta}(i, j) = \sum_{x=1}^{M} \sum_{y=1}^{N} \delta(x, y) \tag{3.12}$$

where

$$\delta(x, y) = \begin{cases} 1 \quad \text{if } I(x, y) = i \text{ and } I(x + \Delta x, y + \Delta y) = j \\ \\ 0 \quad \text{otherwise} \end{cases} \tag{3.13}$$

$r^2 = (\Delta x^2 + \Delta y^2)$, $\theta = tan^{-1}\left(\frac{\Delta x}{\Delta y}\right)$, and $C_{d,\theta}(i, j)$ represents the number of occurrences of gray level j adjacent to gray-level i separated by a distance d in direction θ.

The second-order probability mass function, $\big[P\big]$, is computed form the GLCM matrix after normalization and is expressed as follows:

$$P_{d,\theta}(i, j) = \frac{C_{d,\theta}(i, j)}{\sum_{l,m} C_{d,\theta}(l, m)} \tag{3.14}$$

From the GLCM probability mass function or joint probability distribution, different attributes are obtained. [54] first time used the GLCM based attributes to detect salt boundaries in seismic images. The most commonly used attributes are discussed as follows:

GLCM Contrast: The GLCM contrast measures the local gray-level variations of neighboring pairs or spatial frequency in an image. It is also called difference moment. It is computed as follows:

$$\text{GLCM Contrast} = \sum_i \sum_j |i-j|^2 P(i,j) \tag{3.15}$$

For a low contrast image, the principal diagonal of GLCM matrix is more concentrated compared to the high contrast image. The GLCM contrast is low if the neighboring points have similar amplitudes. Seismic Salt regions and horizons have smooth texture; therefore, the value of contrast is low for these areas whereas it is high for salt boundaries which are rich in texture.

GLCM Entropy: The GLCM Entropy is a measure of spatial disorder or complexity in textures. It is computed as:

$$\text{GLCM Entropy} = -\sum_i \sum_j P(i,j) log P(i,j) \tag{3.16}$$

Its value is low for uniform texture whereas it is high for complex textures. For seismic images, its value is high for dipping reflectors and low for salt areas.

GLCM Dissimilarity: The GLCM Dissimilarity is similar to the GLCM contrast attribute with a difference in power in the expression. It measures the amplitude variations of neighboring pairs in an image. It is defined as follow:

$$\text{GLCM Dissimilarity} = \sum_i \sum_j |i - j| \, P(i,j) \tag{3.17}$$

It is low when the neighboring pairs have similar gray-levels. For seismic images, it is high where we observe signicant amplitude variations such as along the salt boundaries and horizons.

GLCM Energy: The GLCM Energy measures the pixel pair repetitions also called texture uniformity or angular second moment. It is also used to measure the texture disorders. It is computed as follows:

$$\text{Energy} = \left[\sum_i \sum_j P(i,j)^2 \right]^{\frac{1}{2}} \tag{3.18}$$

The value of this attribute is high for strong reflectors in seismic images.

GLCM Homogeneity: The GLCM Homogeneity or Inverse Difference Moment measures the homogeneity in an image.

$$\text{Homogeneity} = \sum \sum \frac{1}{1 + (i - j)^2} P(i,j) \tag{3.19}$$

It is maximum when all the elements in an image are same. The GLCM homogeneity and contrast both are strong inversely correlated in terms of equivalent distribution in the pixel pairs that results in decrease of homogeneity decreases with an increase in contrast by keeping constant energy.

GLCM Mutual Information: The GLCM mutual information ([55]) is useful attribute derived from the co-occurrence matrix by considering the joint probability mass function and marginal probabilities along the rows and columns of normalized GLCM and is defined as follows:

$$p_x\left(i\right) = \sum_{j=1}^{L} p\left(i, j\right) \tag{3.20}$$

$$p_y\left(i\right) = \sum_{i=1}^{L} p\left(i, j\right) \tag{3.21}$$

$$MI_{GLCM} = \sum \sum p_{ij} \log_2 \left(\frac{p_{ij}}{p_x(i) p_y(i)} \right) \tag{3.22}$$

For a given seismic image, we derive the six mentioned attributes from the co-occurrence matrices computed for distances $d = 1, 2$ and two orthogonal directions. The second order joint probability mass function is derived from the co-occurrence as defined in 3.14.

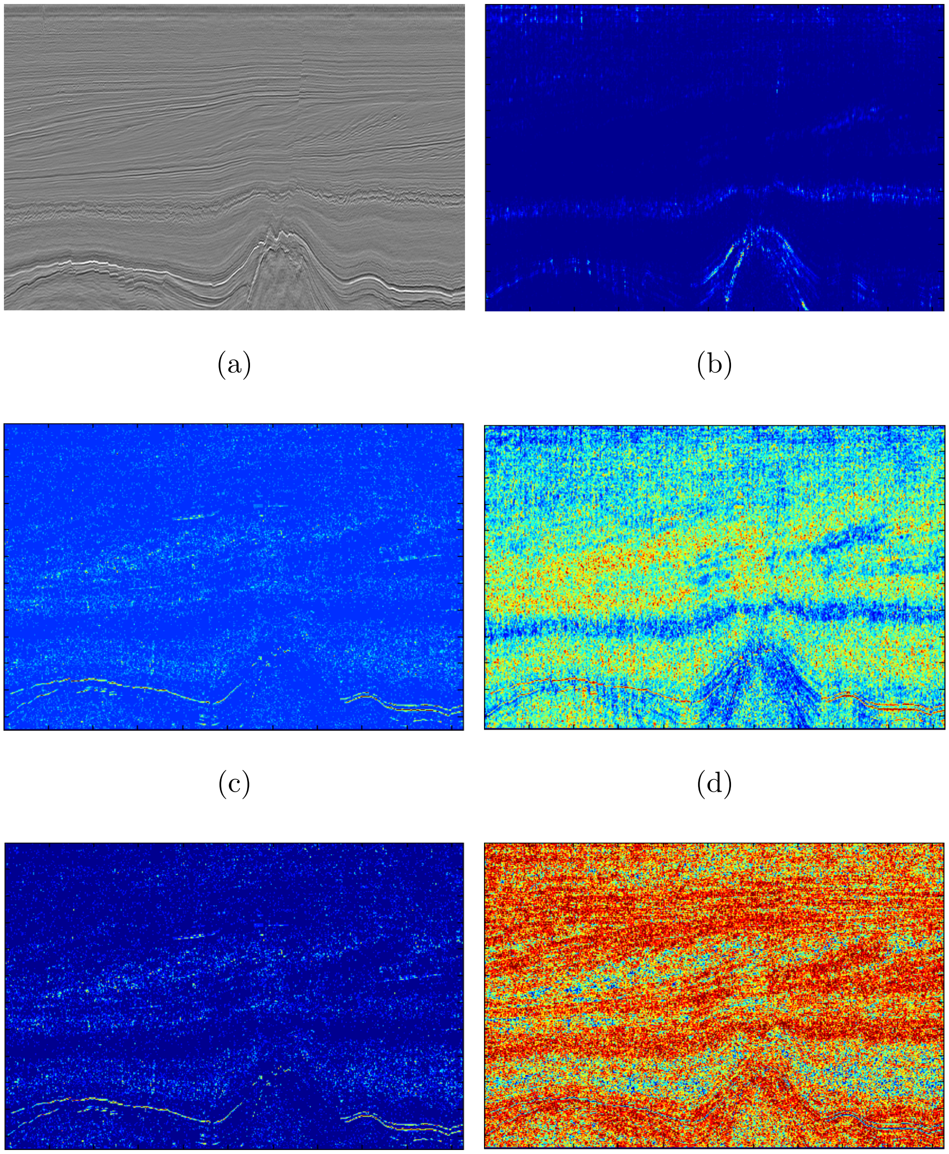

(a) (b)

(c) (d)

(e) (f)

Figure 3.3: (a) Inline # 330, GLCM attributes: (b) Contrast, (c) Energy, (d) Homogeneity, (e) Entropy, (f) MI

3.1.5 Eigenstructure-based Attributes

Self similarity properties of seismic waveforms have traditionally been modeled using the concept of correlation. In particular, the covariance matrix has been used efficiently in estimating the coherence and trace attributes [48]. Such attributes are crucial in detecting salt boundaries. The covariance (or eigenstructure) attributes are computed using the covariance matrix obtained from the gradients in the x, y and z directions.

$$C = \begin{bmatrix} C_{xx} & C_{xy} & C_{xz} \\ C_{yx} & C_{yy} & C_{yz} \\ C_{zx} & C_{zy} & C_{zz} \end{bmatrix} \tag{3.23}$$

$$C_{ab} = \frac{1}{N^3} \sum_{x,y,z} \left(G_a(x,y,z) - \mu_a\right) \left(G_b(x,y,z - \mu_b)\right) \tag{3.24}$$

where N is the window size (N = 9 for 3 x 3 windows), G_a and G_b are the gradients in directions a and b, and μ_a and μ_b are the means in a and b directions. From the covariance matrix, the the most important attributes [43] are:

Trace Attribute: The covariance matrix is first estimated from the data, then decomposed into a set of ordered eigenvalues and corresponding eigenvectors. The eigenvalues of the covariance matrix are used to obtain the trace attribute:

$$\mathrm{Tr} = \sum_i \lambda_i, \tag{3.25}$$

where $\lambda_i^\prime s$ are the eigenvalues of the covariance matrix. Strong reflections from the salt domes create strong amplitudes across the boundary whereas the profile of salt areas is relatively smooth. Therefore, this attribute gives large values along the boundary and low values for non-boundary regions.

Coherency estimate: The coherency estimate, E_c, is based on the eigen structure of the covariance matrix:

$$\mathrm{E_c} = \frac{\lambda_1}{\sum_i \lambda_i}, \tag{3.26}$$

where λ_1 is the highest eigenvalue and $\lambda_1 \cdots \lambda_p$ are the eigenvalues obtained from the eigenvector decomposition of the covariance matrix. The coherence attribute represents contrast information present in seismic slices. The attribute exhibits strong values for the smooth areas and low values across the salt boundaries where we usually have high amplitude variations.

Largest eigenvalue attribute: The largest singular value attribute is, itself, used as an attribute:

$$\lambda_1 = max(\lambda_i) \tag{3.27}$$

Salt boundaries are often represented by strong edges in seismic data. The largest eigenvalue attribute represents edge strength in a chosen volume. The value of this attribute is high for salt boundaries represented by strong edges and weak for surrounding areas. We display in Fig. 3.4 the feature maps obtained using the eigen structure attributes for Inline # 331.

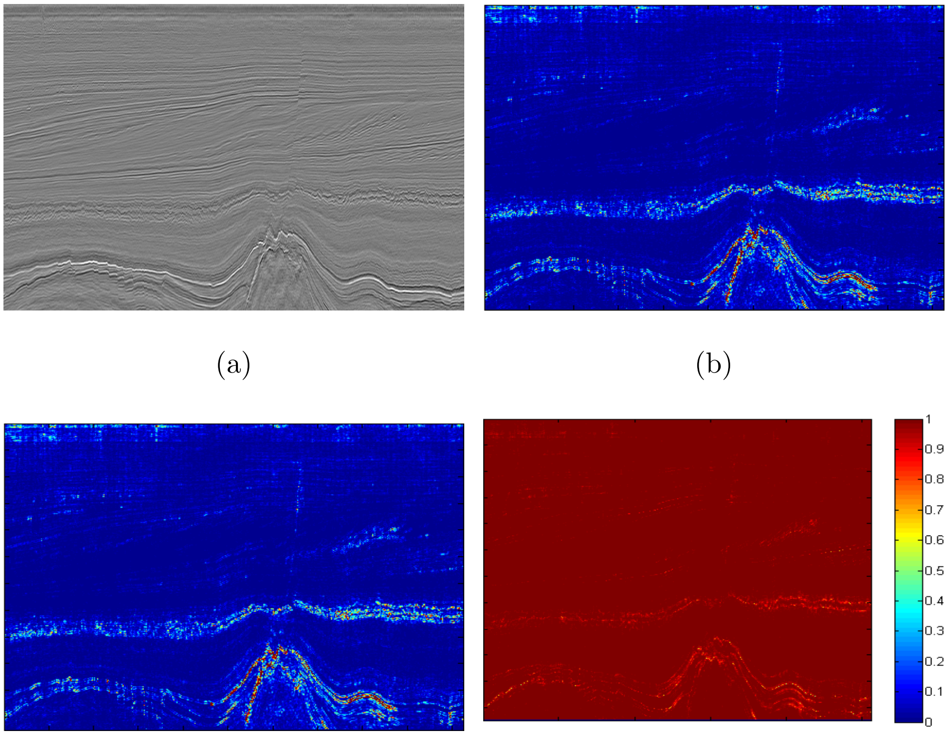

(a) (b)

(c) (d)

Figure 3.4: (a) Inline # 330, Eigen structure attributes: (b) Trace, (c) Largest eigen value, (d) Coherence estimate

3.1.6 Local Radii Index (LRI) Attributes

The seismic images belong to the homogeneous texture class, therefore, can be characterized by the distribution of distances between adjacent edges at some particular angle. The Local Radial Index (LRI), proposed by [56], is a texture similarity metric in spatial domain based on edge distances in different directions. A local index can be computed for each image pixel in two different ways, resulting in two variations of LRI i.e. LRI-A and LRI-D. In LRI-A, inter-edge distance (i.e., width of adjacent smooth regions) in each given direction is calculated whereas, in LRI-D, the distance from pixels to the nearest edge (i.e., boundary of next smooth region) is calculated in each given direction. An example of computing LRI-A and LRI-D for a small group of pixels in an image is shown in Figure 3.5. A local index is computed for each image pixel and 8 histograms are created for each neighboring direction. The algorithm for LRI-A and LRI-D indices is as follows:

LRI-A Index:

For i^{th} pixel x_i and directions $d = 1, \cdots, 8$, let a_{dj} denote j neighboring pixels in direction d, where $j = 1, \cdots, K$.

$$LRIA_d = \begin{cases} 0, & \text{if } |x_i - a_{d1}| \leq T \\ \min\,(j, K), & \text{if } a_{dj} > x_i + T \text{ for } j = 1, \cdots, K \text{ but not K+1} \\ \max(-j, -K), & \text{if } a_{dj} < x_i - T \text{ for } j = 1, \cdots, K \text{ but not K+1} \end{cases} \tag{3.28}$$

LRI-D Index:

$$LRID_d = \begin{cases} 0, & \text{if } |x_i - a_{d1}| > T \\ \min\,(j, K) \bmod K, & \text{if } |x_i - a_{dj}| < T \text{ for } j = 1, \cdots, K-1 \text{ and } a_k > x_k + T \\ -(\min(j, K) \bmod K), & \text{if } |x_i - a_{dj}| \leq T \text{ for } j = 1, \cdots, K-1 \text{ and } a_k < x_k - T \end{cases} \tag{3.29}$$

where threshold T is used to determine edge and controls noise sensitivity and K is used to limit the size of texture elements and it reduces the computational complexity. For our experiments, we have used $T = \sigma/2$ and $K = 3$. The maximum value of L is limited to $[-K, K]$ which results in $(2K + 1)$ bin-histogram $H_1, H_2, \cdots, H_8$ in each given direction. The LRI features for an image are computed as concatenation of the eight histograms for both LRI-A and LRI-D respectively.

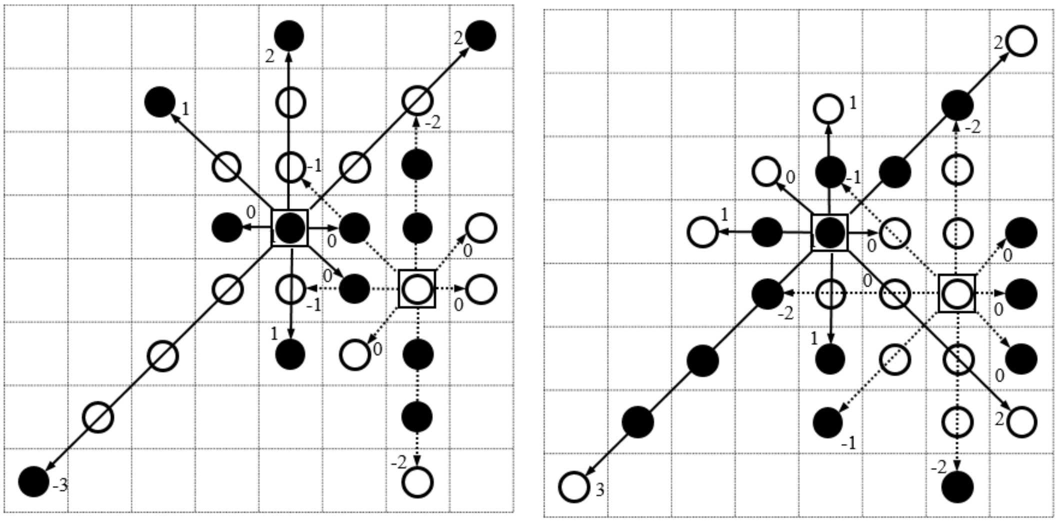

(a) (b)

Figure 3.5: An LRI example (a) LRI-A (b) LRI-D

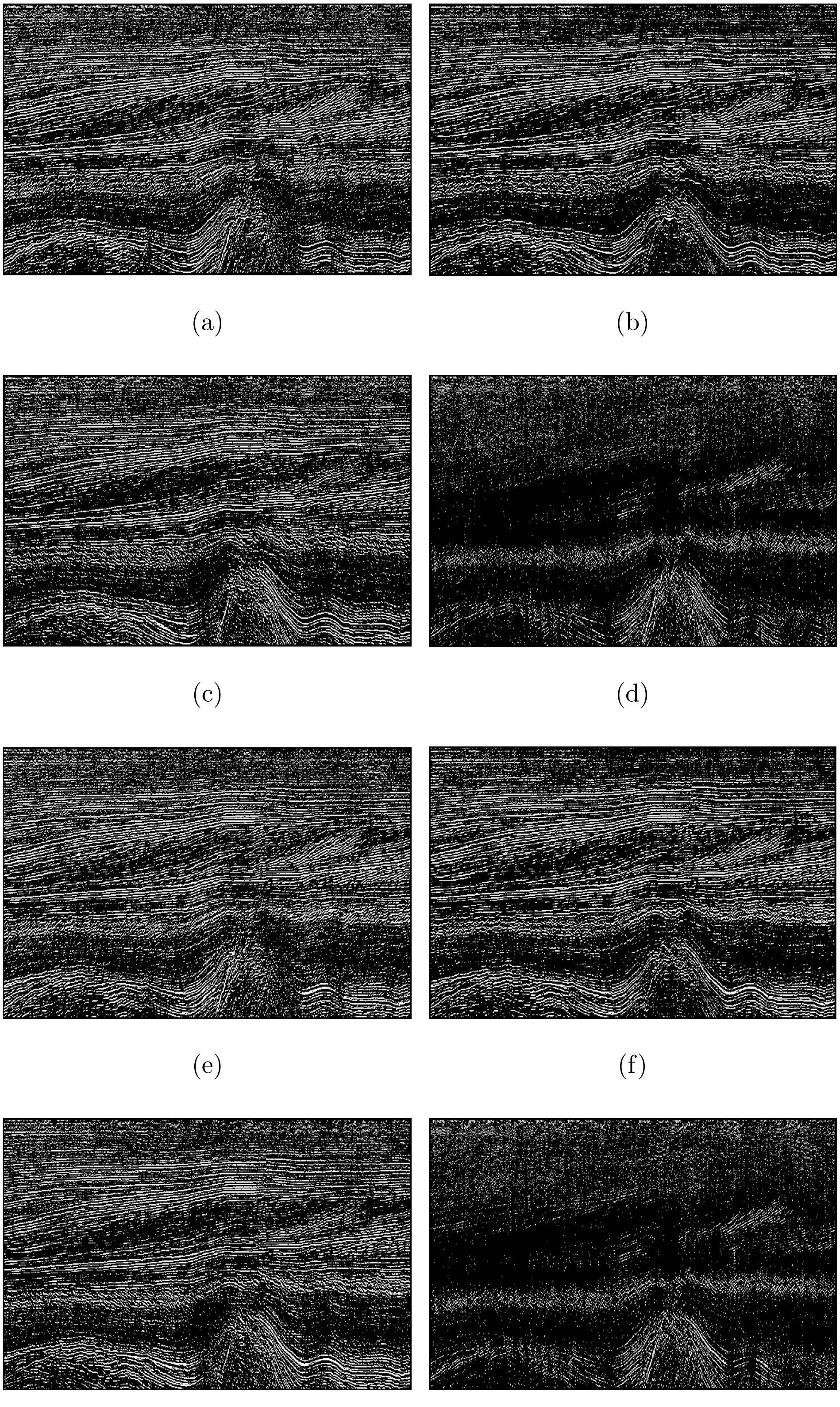
(a) (b) (c) (d) (e) (f) (g) (h)

Figure 3.6: LRI-A attributes: (a) $\theta = 0$, (b) $\theta = \pi/4$, (c) $\theta = \pi/2$, (d) $\theta = 3\pi/4$, (e) $\theta = \pi$, (f) $\theta = 5\pi/4$, (g) $\theta = 3\pi/2$, (h) $\theta = 7\pi/4$

3.2 Frequency Domain Attributes

3.2.1 Gabor Filters

Periodicity and orientation of seismic textures can be described using attributes derived from the Fourier spectrum. Frequency-based texture attributes are used to extract the impact of reflectors. Gabor filters, as discussed in [48], can be used in seismic image processing to extract frequency-based attributes [57] [58] [59]. The normalized energy values computed from the Gabor filtered images are used as the frequency attributes [48]. Different choice of parameters can discriminate between seismic textures with different frequency content. Gabor filters are designed to find the dominant size and orientation of different textures in the image. In spatial domain, the general form of Gabor filter is defined as:

$$g(x, y, \omega) = \frac{1}{2\pi\sigma^2} exp\left(-\frac{x^{'2} + y^{'2}}{2\sigma^2}\right)\left(exp\left(2\pi i\omega x^{'}\right) - exp\left(-\frac{\omega^2\sigma^2}{2}\right)\right), \quad (3.30)$$

where $x^{'} = xcos\theta + ysin\theta$, $y^{'} = -xsin\theta + ycos\theta$, σ is the standard deviation of Gaussian function along the x and y directions, $\omega =$ is the radial center frequency The Gabor filter with orientation θ and a given radial filter center ω is given by:

$$\mathrm{H(u^{'}, v^{'})} = \frac{8\sigma_u\sigma_v}{\pi}\left(exp\left(-\frac{1}{2}\left[\frac{(u^{'} - \omega)^2}{\sigma_u^2} + \frac{v^2}{\sigma_v^2}]\right]\right) + exp\left(-\frac{1}{2}\left[\frac{(u^{'} + \omega)^2}{\sigma_u^2} + \frac{v^2}{\sigma_v^2}\right]\right)\right), \quad (3.31)$$

where $u^{'} = u\cos\theta + v\sin\theta$, $v^{'} = -u\sin\theta + v\cos\theta$, σ_u and σ_v specify the filter width, and $\theta_k = \frac{\pi(k-1)}{K}, k = 1, 2, 3, ..., K$. For our experiments, we have used the Gabor filters in two scales and four orientations. In Fig. 3.7, we show the Gabor filter masks corresponding to two scales and $\theta = 0, \pi/4, \pi/2, 3\pi/4$.

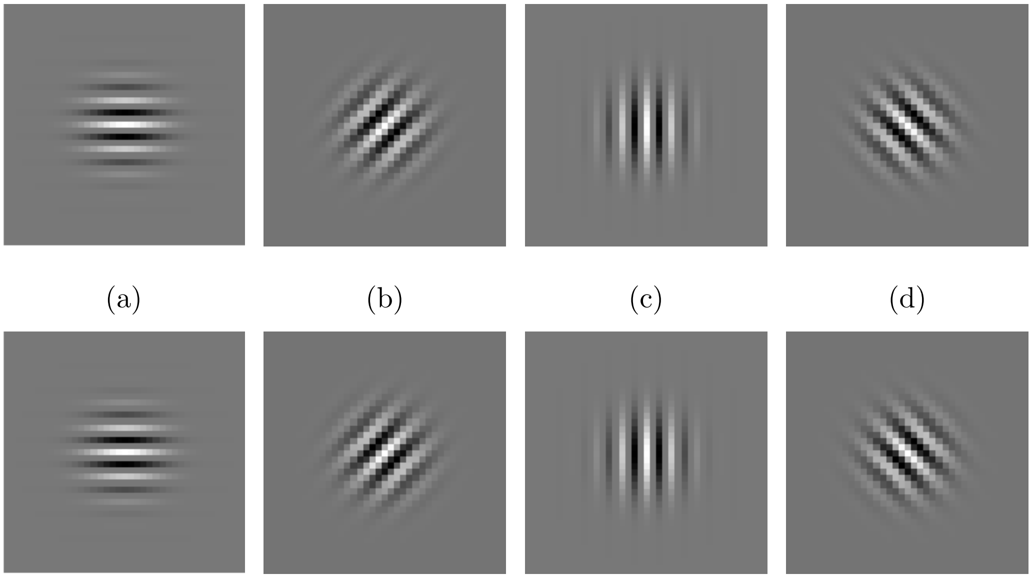

(a) (b) (c) (d)

(e) (f) (g) (h)

Figure 3.7: Gabor filter masks, scale-1: (a) $\theta = 0$, (b) $\theta = \pi/4$, (c) $\theta = \pi/2$, (d) $\theta = 3\pi/4$, scale-2: (e) $\theta = 0$, (f) $\theta = \pi/4$, (g) $\theta = \pi/2$, (h) $\theta = 3\pi/4$

We display in Fig. 3.8 the feature maps obtained using the Gabor filter with $\theta = 0, \pi/4, \pi/2, 3\pi/4$.

The Gabor filter approach discussed in [60][61] can also be used to extract frequency-based attributes for segmentation of salt bodies.

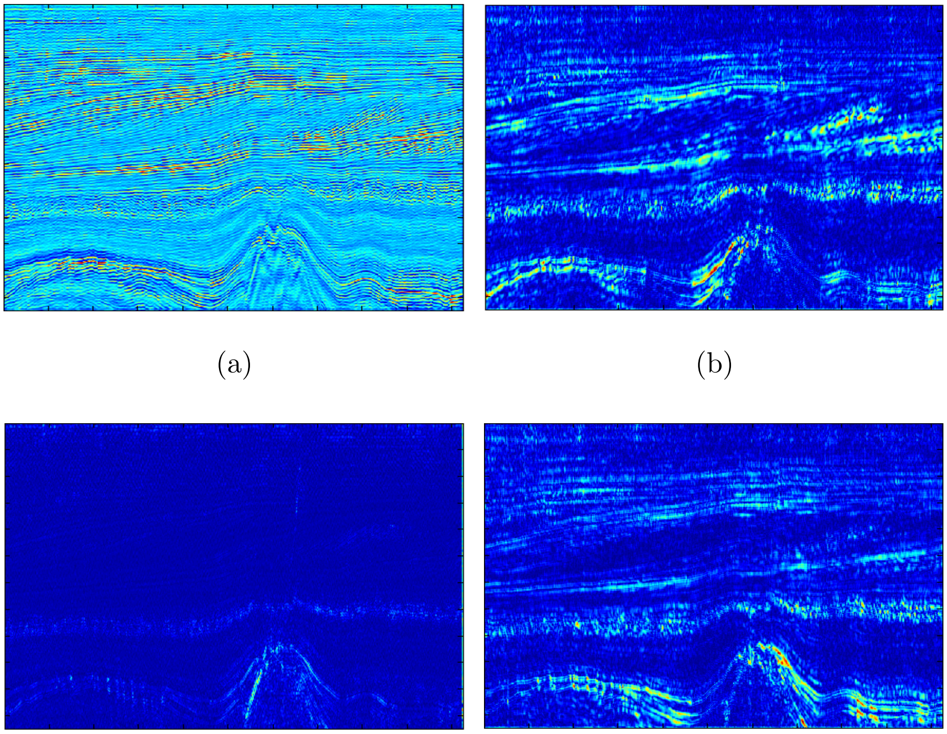

(a) (b) (c) (d)

Figure 3.8: Gabor filter attributes, scale-1: (a) $\theta = 0$, (b) $\theta = \pi/4$, (c) $\theta = \pi/2$, (d) $\theta = 3\pi/4$

3.2.2 Dip Attributes

Dip attributes are used to differentiate salt structures from the surroundings. Salt structures have low Dip estimates.

- **Image gradient based Dip estimate:** Dip estimate can be derived from the Gradient Image.

$$\text{Dip} = \tan^{-1}\left(\frac{G_x}{G_y}\right) \tag{3.32}$$

- **Fourier Sector Dip:** Dip estimate can be also be computed using Fourier spectrum.

$$\mathbb{E}(u,\theta) = \frac{\sum_{u=1}^{N} \sum_{v=1}^{N} |H(u,v)|^2 |F(u,v)|^2}{\sum_{u=1}^{N} \sum_{v=1}^{N} |F(u,v)|^2} \tag{3.33}$$

where H(u,v) is the frequency response of a Gabor filter.

3.2.3 Dominant Frequencies Attributes

Dominant frequencies f_u and f_v, computed in horizontal and vertical directions, are given as:

$$f_u = \frac{\sum_{u=1}^{N} \sum_{v=1}^{N} uF(u,v)}{\sum_{u=1}^{N} \sum_{v=1}^{N} F(u,v)} \tag{3.34}$$

$$f_v = \frac{\sum_{u=1}^{N} \sum_{v=1}^{N} vF(u,v)}{\sum_{u=1}^{N} \sum_{v=1}^{N} F(u,v)} \tag{3.35}$$

where F(u,v) is the local 2D Fourier spectrum taken over the first quadrant. 2N x 2N is the size of input.

CHAPTER 4

NEW APPROACHES FOR SALT DOME DETECTION

Salt bodies play an important role in subsurface geology, therefore accurate salt dome detection is essential for any seismic interpretation task. Detecting salt body boundary and shape accurately, however, is very difficult due to large noise and amplitude variations in seismic data. Salt dome boundary is generally represented by a strong reflector, therefore edge detection based techniques are really useful in delineating salt bodies. However, the edge-based attributes are not able to segment salt bodies accurately in the absence of strong amplitudes. A salt structure can be defined as an area of incoherent texture compared to its surroundings. Therefore, texture-based attributes can reveal differences between salt areas and surrounding geology as compared to edge based attributes In this chapter, we introduce new approaches for salt dome detection using edge-based, texture-based, and fusion of edge and texture based methods. We also introduce new attributes for salt dome detection using HOSVD.

4.1 A Novel Approach for Salt Dome Detection using A 3D Multidirectional Edge Detector

Accurate salt dome structures detection from 3D seismic data is of crucial importance in different seismic data analysis applications. The edge detection based techniques are simple and very useful in detecting broadly the salt dome boundaries in seismic data. In this section, we present a robust framework for salt dome detection based on a new formulation of the 3D edge detector. Most of the existing 2D edge based techniques only consider edges in x and y directions and 3D edge based techniques consider edges in x, y, and z directions. Such schemes often fails to trace the salt boundary accurately along the diagonals. In this work, we propose two new 3D Sobel operators that compute the edges along the diagonal directions as well. We combine the diagonal edges along with the edges in x, y, and, z directions to overcome the weaknesses of existing amplitude based salt dome detection methods. Our algorithm produces finer results as compared to existing edge based and texture attributes based salt dome detection methods when used separately. More importantly, the proposed approach is shown to be computationally efficient allowing for real time implementation and deployment.

4.1.1 3D Multidirectional Edge Detector based Salt Dome Detection Algorithm

The proposed algorithm works by computing the edge map of 3D seismic data. The algorithm considers diagonal edges along with the edges in x, y, and z directions. It starts by normalizing the available data to enhance the salt dome edges. Next, we compute the gradient magnitudes in x, y, z, and diagonal directions. We get the outline of the salt boundary by combining and thresholding all the edge maps. Fig. 4.1 shows the flowchart for the proposed algorithm. We will now discuss each of the blocks from Fig.1 in more details.

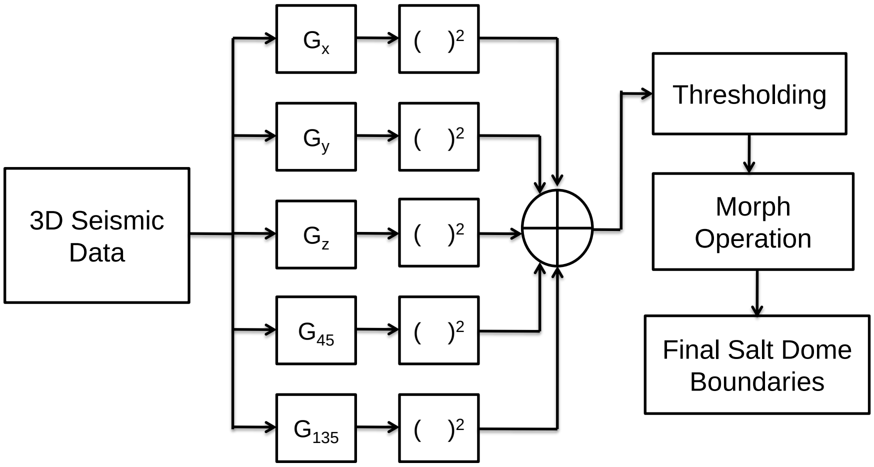

Figure 4.1: The proposed 3D multidirectional edge-based algorithm.

The 2D Sobel Edge Detector

Edge detection is one of the most important image processing tasks used to detect pixels intensity variations in an image. Edge detection can be used for the accurate estimation of dissimilarities caused by faulting or stratigraphic variations. Therefore, edge detection based techniques are really useful in detecting salt dome boundaries in seismic data.

The Sobel edge detector, which uses the first derivative, is the most common operator used in the detection of salt domes. The Sobel operator is a differentiation operator which computes the gradient of the image intensity function. The Sobel edge detector in 2D computes spatial gradients of a 2D image and enhances regions of high frequency that represent edges. The discrete gradient equations for a 3x3 Sobel edge detector in the x and y directions are given as:

$$\begin{aligned} G_x = &\{g(x+1,y-1)+2g(x+1,y)+g(x+1,y+1)\} \\ &-\{g(x-1,y-1)+2g(x-1,y)+g(x-1,y+1)\} \end{aligned} \tag{4.1}$$

$$\begin{aligned} G_y = &\{g(x-1,y+1)+2g(x,y+1)+g(x+1,y+1)\} \\ &-\{g(x-1,y-1)+2g(x,y-1)+g(x+1,y-1)\} \end{aligned} \tag{4.2}$$

where $g(x,y)$ is the amplitude value at x and y position. The magnitude of the total gradient is given as:

$$G = \sqrt{{G_x}^2 + {G_y}^2} \tag{4.3}$$

The convolution operators for the Sobel edge detector in the x direction and y directions are given as:

$$G_x = \begin{bmatrix} -1 & 0 & 1 \\ -2 & 0 & 2 \\ -1 & 0 & 1 \end{bmatrix} \tag{4.4}$$

$$G_y = \begin{bmatrix} -1 & -2 & -1 \\ 0 & 0 & 0 \\ 1 & 2 & 1 \end{bmatrix} \tag{4.5}$$

From the above formulation, we note that the first mask detects discontinuities in one direction and the second mask detects discontinuities in the other direction. The boundary of the salt dome is tracked by combining the two dissimilarity maps into a single magnitude map. An example of the resulting salt boundary is shown in Fig. 4.2.

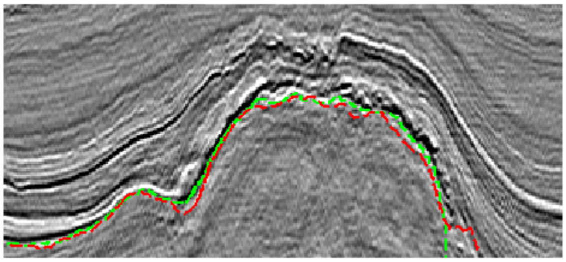

Figure 4.2: Salt boundary detected for the Inline # 111 using 2D Sobel edge detector.

Other edge detection based techniques such as the Prewitt edge detector [20], and the Scharr edge detector can also be used to detect salt boundaries. Like the

Sobel operator, the Prewitt operator is also a first order edge operator but using different kernels. The Prewitt gradients, in the x and y directions, are given as:

$$G_x = \begin{bmatrix} -1 & 0 & 1 \\ -1 & 0 & 1 \\ -1 & 0 & 1 \end{bmatrix} \tag{4.6}$$

$$G_y = \begin{bmatrix} -1 & -1 & -1 \\ 0 & 0 & 0 \\ 1 & 1 & 1 \end{bmatrix} \tag{4.7}$$

while the Scharr gradients, in the x and y directions, are given as:

$$G_x = \begin{bmatrix} -1 & 0 & 1 \\ -3 & 0 & 3 \\ -1 & 0 & 1 \end{bmatrix} \tag{4.8}$$

$$G_y = \begin{bmatrix} -1 & -3 & -1 \\ 0 & 0 & 0 \\ 1 & 3 & 1 \end{bmatrix} \tag{4.9}$$

Fig. 4.3 and 4.4 show an example of salt boundaries detected by the Prewitt and the Scharr edge detectors. Fig. 4.5 gives a comparison of Sobel, Prewitt, and Scharr edge detectors for salt dome detection. We can see that the boundary detected by the Sobel operator is very close to the ground truth. On the hand, the boundary detected by the Prewitt and Scharr edge detector deviate a bit from the ground truth. The better performance of the Sobel edge detector is due to the double weight on the center point. This increase in the weight helps in suppressing noise [62].

Although the Sobel operator gives better results as compared to other edge detectors, considering the gradient map only in the x and y directions may not give accurate results along the diagonal directions of salt dome boundaries. Fig. 4.6 shows the zoomed version of diagonal parts of the salt boundary detected by the Sobel edge detector. It can be seen that the detected boundary is not very close to the ground truth.

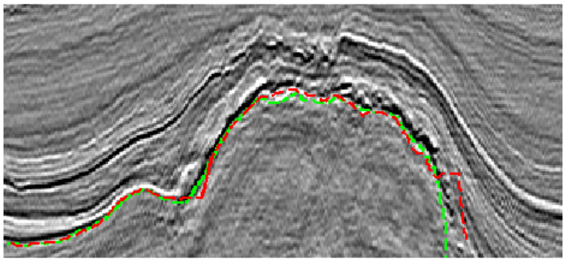

Figure 4.3: Salt boundary detected for Inline # 111 using the Prewitt edge detector.

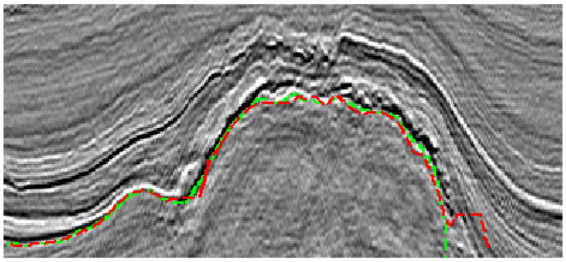

Figure 4.4: Salt boundary detected for Inline # 111 using the Scharr edge detector.

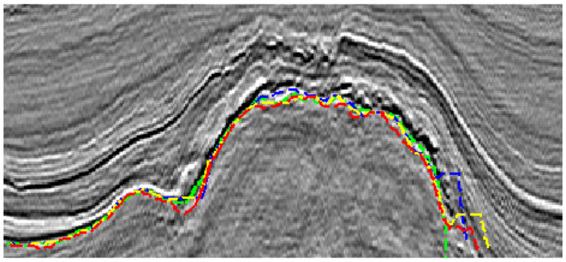

Figure 4.5: Ground truth (Green), 2D Sobel edge detector (Red), Prewitt edge detector (Blue), Scharr edge detector (Yellow)

To improve the performance of the Sobel edge detector, we include the diagonal directions along with x and y directions. The discrete gradient equation for 3x3 Sobel edge detector in the diagonal directions are given as:

$$\begin{aligned} G_{45} = &\{g(x+1,y) + 2g(x+1,y+1) + g(x,y+1)\} \\ &- \{g(x-1,y) + 2g(x-1,y-1) + g(x,y-1)\} \end{aligned} \tag{4.10}$$

$$\begin{aligned} G_{135} = &\{g(x-1,y) + 2g(x-1,y+1) + g(x,y+1)\} \\ &- \{g(x,y-1) + 2g(x+1,y-1) + g(x+1,y)\} \end{aligned} \tag{4.11}$$

The convolution operators for the Sobel edge detector in the diagonal directions are given as:

$$G_{45} = \begin{bmatrix} -2 & -1 & 0 \\ -1 & 0 & 1 \\ 0 & 1 & 2 \end{bmatrix} \tag{4.12}$$

$$G_{135} = \begin{bmatrix} 0 & -1 & -2 \\ 1 & 0 & -1 \\ 2 & 1 & 0 \end{bmatrix} \tag{4.13}$$

The magnitude of the total gradient is now computed as:

$$G = \sqrt{{G_x}^2 + {G_y}^2 + {G_{135}}^2 + {G_{45}}^2} \tag{4.14}$$

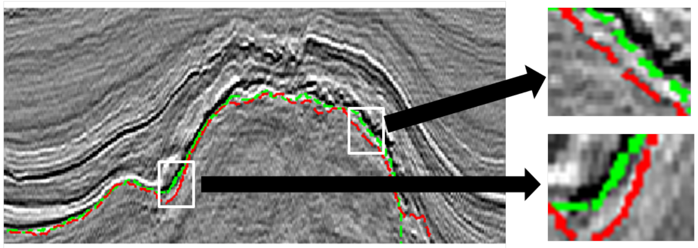

Figure 4.6: Zoomed portion of detected salt boundary using 2D Sobel edge detector without diagonal edges

The 3D Extension of the Sobel Edge Detector

For 3D seismic data, the Sobel operator on 2D slices is extended to 3D taking into account continuity in the medium. In the case of the 3D Sobel operator, the first mask detects discontinuity in the x direction, the second mask detects dissimilarity in the y direction, and the third mask detects dissimilarity in the z direction. The boundary of the salt dome is tracked by combining the three dissimilarity maps into a single magnitude map. The size of 3D Sobel operator, used in our algorithm, for each direction is 3x3x3. The convolution operator for

3D Sobel edge detector in the x direction, y direction, and z direction is given as:

$$G_x(:,:,-1) = \begin{bmatrix} -1 & 0 & 1 \\ -2 & 0 & 2 \\ -1 & 0 & 1 \end{bmatrix} G_x(:,:,0) = \begin{bmatrix} -2 & 0 & 2 \\ -4 & 0 & 4 \\ -2 & 0 & 2 \end{bmatrix} G_x(:,:,1) = \begin{bmatrix} -1 & 0 & 1 \\ -2 & 0 & 2 \\ -1 & 0 & 1 \end{bmatrix} \tag{4.15}$$

$$G_y(:,:,-1) = \begin{bmatrix} -1 & -2 & -1 \\ 0 & 0 & 0 \\ 1 & 2 & 1 \end{bmatrix} G_y(:,:,0) = \begin{bmatrix} -2 & -4 & -2 \\ 0 & 0 & 0 \\ 2 & 4 & 2 \end{bmatrix} G_y(:,:,1) = \begin{bmatrix} -1 & -2 & -1 \\ 0 & 0 & 0 \\ 1 & 2 & 1 \end{bmatrix} \tag{4.16}$$

$$G_z(:,:,-1) = \begin{bmatrix} -1 & -2 & -1 \\ -2 & -4 & -2 \\ -1 & -2 & -1 \end{bmatrix} G_z(:,:,0) = \begin{bmatrix} 0 & 0 & 0 \\ 0 & 0 & 0 \\ 0 & 0 & 0 \end{bmatrix} G_z(:,:,1) = \begin{bmatrix} 1 & 2 & 1 \\ 2 & 4 & 2 \\ 1 & 2 & 1 \end{bmatrix}$$

The magnitude of the total gradient is given as:

$$G = \sqrt{{G_x}^2 + {G_y}^2 + {G_z}^2} \tag{4.17}$$

As discussed for the case of 2D Sobel edge detection, the Sobel operator in the x, y, and z directions may not produce accurate results for the diagonal parts of salt dome boundaries. We, therefore, introduce two more Sobel operators in the diagonal directions to detect the diagonal edges. The convolution operators for the 3D Sobel in the diagonal directions are given as:

$$G_{45}(:,:,-1) = \begin{bmatrix} -2 & -1 & 0 \\ -1 & 0 & 1 \\ 0 & 1 & 2 \end{bmatrix} G_{45}(:,:,0) = \begin{bmatrix} -4 & -2 & 0 \\ -2 & 0 & 2 \\ 0 & 2 & 4 \end{bmatrix} G_{45}(:,:,1) = \begin{bmatrix} -2 & -1 & 0 \\ -1 & 0 & 1 \\ 0 & 1 & 2 \end{bmatrix}$$

$$G_{135}(:,:,-1) = \begin{bmatrix} 0 & -1 & -2 \\ 1 & 0 & -1 \\ 2 & 1 & 0 \end{bmatrix} G_{135}(:,:,0) = \begin{bmatrix} 0 & -2 & -4 \\ 2 & 0 & -2 \\ 4 & 2 & 0 \end{bmatrix} G_{135}(:,:,1) = \begin{bmatrix} 0 & -1 & -2 \\ 1 & 0 & -1 \\ 2 & 1 & 0 \end{bmatrix}$$

Based on this new formulation, the resulting magnitude of the total gradient is now obtained as:

$$G = \sqrt{{G_x}^2 + {G_y}^2 + {G_z}^2 + {G_{45}}^2 + {G_{135}}^2} \tag{4.18}$$

4.1.2 Experimental Results

We tested our salt dome detection method on the Netherlands offshore F3 block acquired from the North Sea. The data set covers a block of 24 x 16 km^2. The Inline range is from 100 to 750, the cross line range is 300 to 1250, and the time direction ranges from 0 to 1848 ms. In the first step, we applied normalization scheme to enhance the salt dome edges in the dataset. Next, we applied the proposed 3D Sobel edge detector to delimit the salt boundaries.

Inline # 111 is considered as a test case to compare the performance of our proposed 3D salt dome detection method with the conventional 2D Sobel edge detector based method. Fig. 4.7 shows the ground truth and the salt boundary detected using the proposed method. The green boundary here is the ground truth, while red is the boundary produced by the proposed method. We see that the proposed method is able to outline the boundary with excellent accuracy. Fig. 4.8 provides a comparison of the 2D Sobel edge detector and our proposed 3D Sobel edge detector. We can see that the proposed method detects the salt boundary with excellent accuracy. Fig. 4.9 shows the boundary points using the proposed method, the 2D Sobel edge detector, and the ground truth points. We can see that the boundary produced by our algorithm is very close to the ground truth. The boundary produced by the 2D Sobel edge detector based method loses the track at many points along the diagonal boundaries.

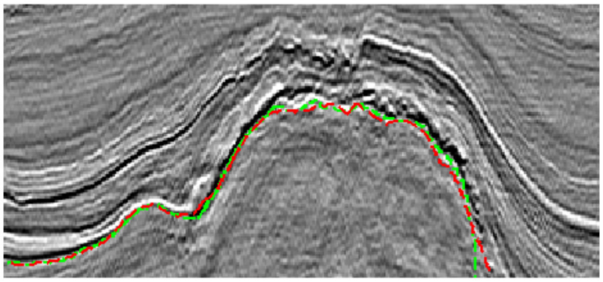

Figure 4.7: Ground truth (Green), Salt boundary detected for Inline # 111 using the proposed multideirectional edge-based method (Red).

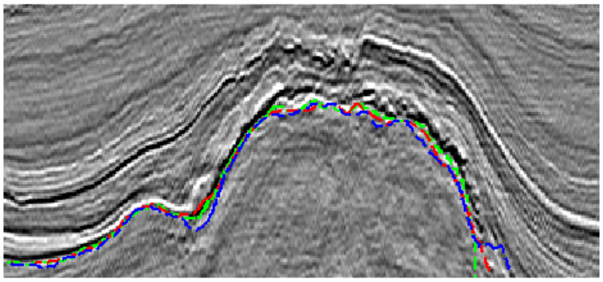

Figure 4.8: Ground truth (Green), Salt boundary detected for Inline # 111 using the proposed multidirectional edge-based method (Red), Salt boundary detected for Inline # 111 using the 2D Sobel edge detector (Blue).

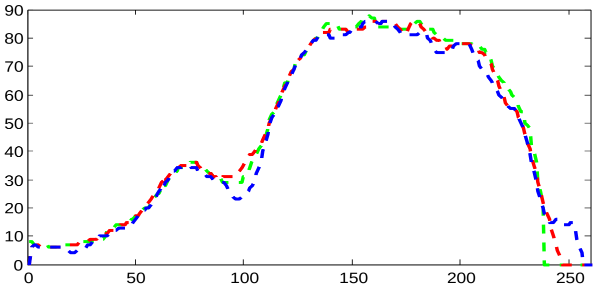

Figure 4.9: Ground truth points (Green), Salt boundary points using the proposed multidirectional edge-based method (Red), Salt boundary points using the 2D Sobel edge detector (Blue).

Numerous other examples are provided in Fig. 4.15 for Inlines # 111 to 134 using the proposed method. The proposed algorithm gives excellent results even for the Inlines which have an uneven salt boundary.

We compared the performance of our method with the 2D Sobel edge detector based salt dome detection method [2], the 3D Sobel edge detector based method [3], and the texture attributes based method [43]. For the texture attributes based method, GLCM based features, eigen structure based features and Gabor filter based attributes are used. Figure 4.10 shows the results of the salt boundary detected using the proposed method, 2D Sobel based method, 3D Sobel based method, and the texture based method. The green boundary here is the ground truth, red is the boundary produced by the proposed method, blue is the boundary produced by the 2D Sobel based method, yellow is the boundary produced by the Aqrawi's 3D Sobel based method, and pink is the boundary produced by texture based method. We can see that the results obtained using our proposed algorithm outperforms all other methods (see also Fig. 4.11). We can see that the boundary produced by our algorithm is very close to the ground truth. The 2D and 3D edge based methods [2], [3] are not able to trace the boundary accurately along the diagonals. The texture-based method [43] deviates from the ground truth at multiple points especially at the start and at the end of the salt dome boundary as expected for texture based techniques. Figure 4.12 shows the zoomed version of the diagonal parts of salt dome boundary for Inline # 111. We can see that our algorithm performs better than other edge detection based techniques which fails to trace the boundary accurately along the diagonals.

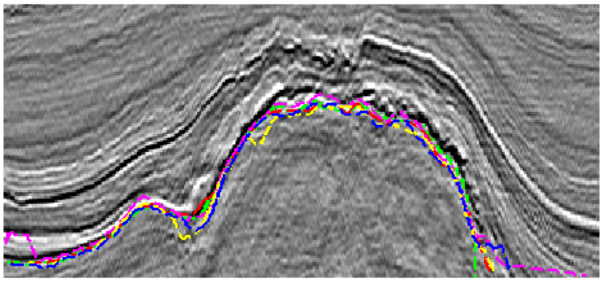

Figure 4.10: Salt boundary detected for Inline # 111: Proposed multidirectional edge-based method (Red), 2D Sobel based method (Blue), 3D Sobel based method (Yellow), Texture attributes based method (Pink), Ground truth (Green)

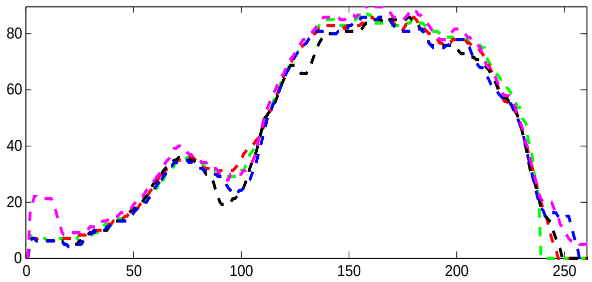

Figure 4.11: Salt boundary points detected for Inline # 111: Proposed multidirectional edge-based method (Red), 2D Sobel based method (Blue), 3D Sobel based method (Black), Texture attributes based method (Pink), Ground truth (Green)

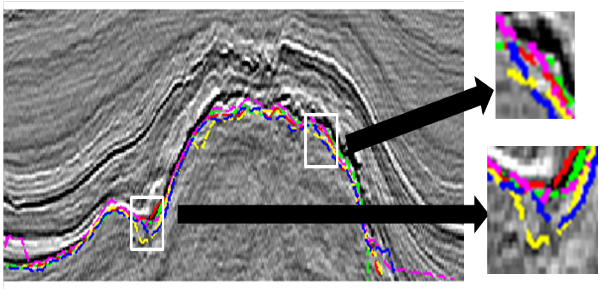

Figure 4.12: Zoomed portion of diagonal salt boundary for Inline # 111: Proposed multidirectional edge-based method (Red), 2D Sobel based method (Blue), 3D Sobel based method (Yellow), Texture attributes based method (Pink), Ground truth (Green)

Finally, we also show in Table 1 the average classification accuracy for Inlines # 111 to 134 (24 images) using the proposed method, the 2D Sobel based method, the 3D Sobel based method, and the texture based method. The proposed method gives an average accuracy of 89% which is 8% higher than the 2D Sobel based method, 4% higher than the 3D Sobel based method, 2% higher than the texture based method (which is computationally very expensive).

Precision, Recall and F-measures have also been used traditionally as evaluation metrics in image segmentation. To measure these metrics, we compute the True Positive (TP), the False Positive (FP), the True Negative (TN), and

Table 4.1: Classification Accuracy of the proposed Multidirectional edge-based method and other methods (averaged over 24 slices)

Salt Dome Detection Method	Accuracy
Proposed method	89.64%
2D Sobel based [2]	81.13%
3D Sobel based [3]	85.22%
Texture attributes based [43]	87.78%

the False Negative (FN) using the ground truth and the detected salt region. Precision, recall, and F-measure are computed using:

$$Precision = \frac{TP}{TP + FP} \tag{4.19}$$

$$Recall = \frac{TP}{TP + FN} \tag{4.20}$$

$$F - Measure = 2 \times \frac{Precision \times Recall}{Precision + Recall} \tag{4.21}$$

In Fig. 4.13, we show the ground truth of the salt dome and the salt regions detected using the proposed method, 2D Sobel based method, 3D Sobel based method, and the texture based method for Inline # 111. In table-2, we show the average precision, recall, and F-measure values computed for Inlines # 111 to 134. The F-measure value obtained for the proposed method is almost 3% higher than Jing and Aqrawi's method and 4% higher than the texture attributes based method. The results show the improved performance obtained using the proposed algorithm while keeping the algorithm complexity to the minimum.

Table 4.2: Precision, Recall, and F-measure of the proposed Multidirectional edge-based method and other methods (averaged over 24 slices)

Salt Dome Detection Method	**Precision**	**Recall**	**F-Measure**
Proposed method	98.66	97.64	98.15
2D Sobel [2]	97.68	94.71	95.17
3D Sobel [3]	98.60	93.99	95.24
Texture attributes [43]	92.88	98.86	94.78

To further illustrate the performance of the proposed algorithm, we show in Fig. 4.14 the detected salt volume using the proposed approach. The algorithm results in a relatively smooth profile as expected in practical scenarios.

However, edge detection based segmentation algorithms are very sensitive to the noise present in seismic data. In case of large amplitude variations, the proposed 3D gradient based workflow may fail to provide a refined salt dome boundary.

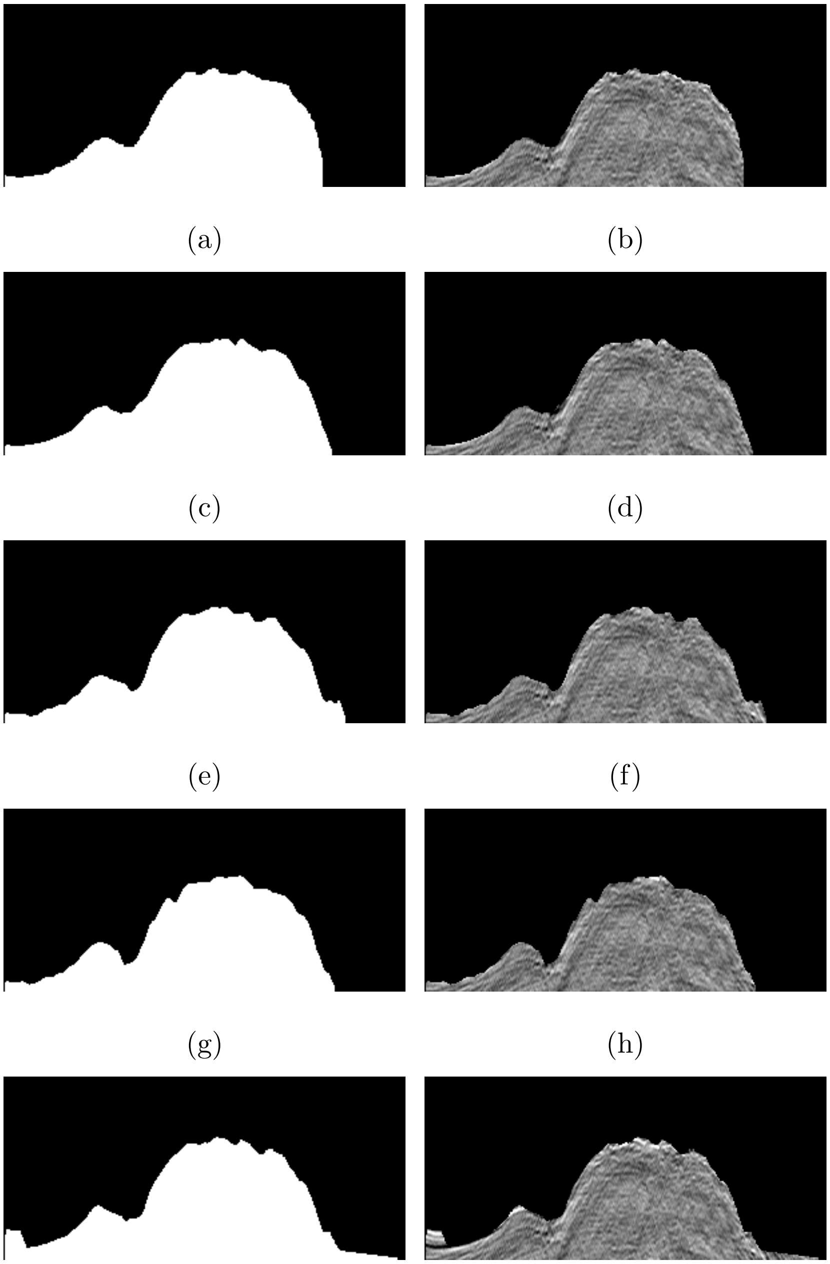

(a) (b)

(c) (d)

(e) (f)

(g) (h)

(i) (j)

Figure 4.13: 1st Row: Ground Truth, Detected salt dome region: The proposed multidirectional edge-based method (2nd Row), 2D Sobel based method (3rd Row), 3D Sobel based method (4th Row), Texture attributes based method (5th Row)

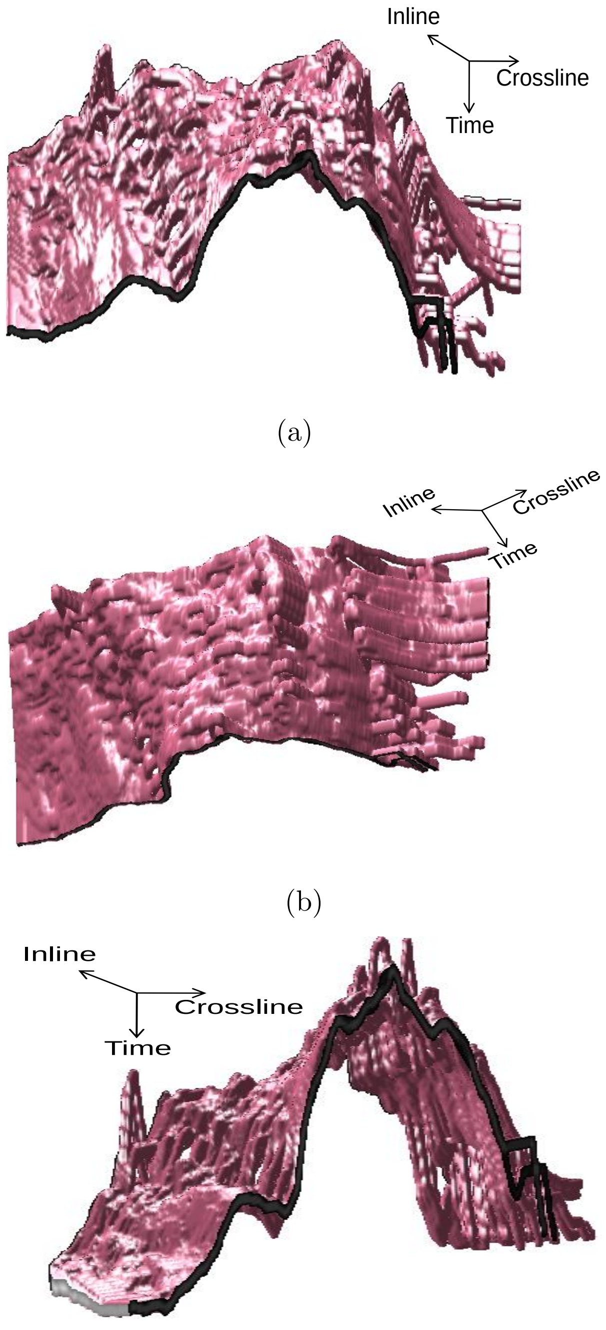

(a)

(b)

(c)

Figure 4.14: 3D Salt Dome detected using the proposed multidirectional edge-based method

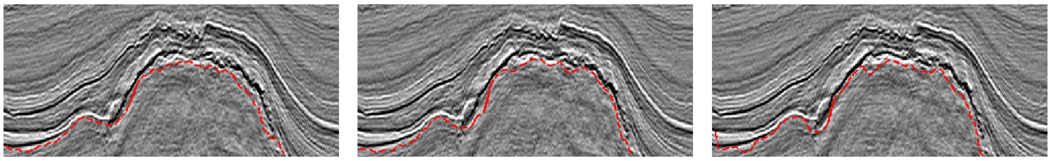

(a) Inline # 111 (b) Inline # 112 (c) Inline # 113

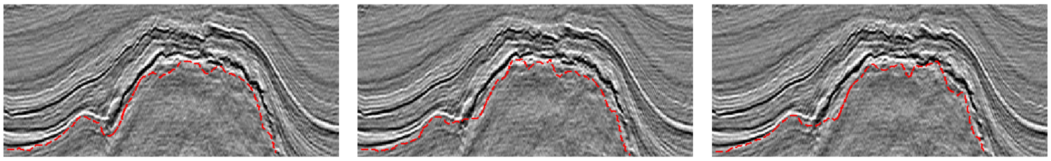

(d) Inline # 114 (e) Inline # 115 (f) Inline # 116

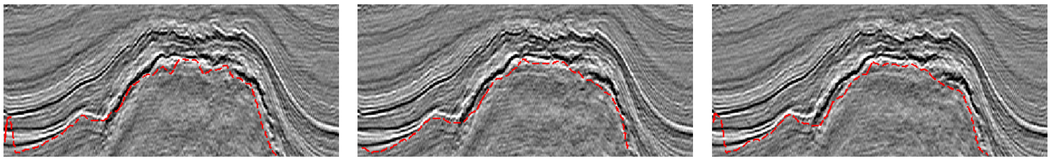

(g) Inline # 117 (h) Inline # 118 (i) Inline # 119

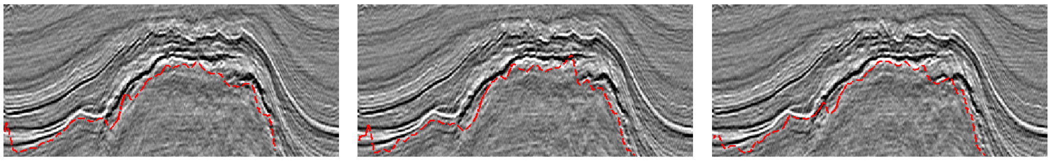

(j) Inline # 120 (k) Inline # 121 (l) Inline # 122

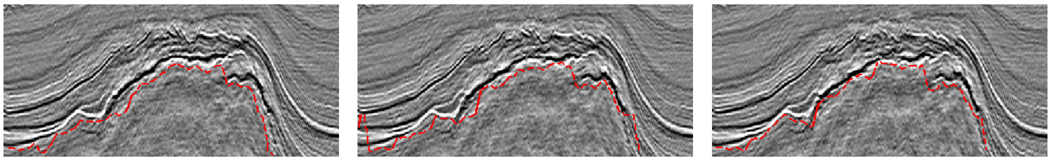

(m) Inline # 123 (n) Inline # 124 (o) Inline # 125

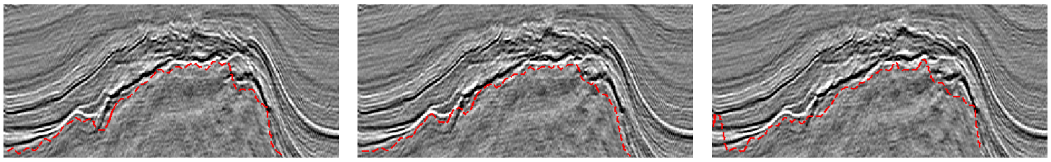

(p) Inline # 126 (q) Inline # 127 (r) Inline # 128

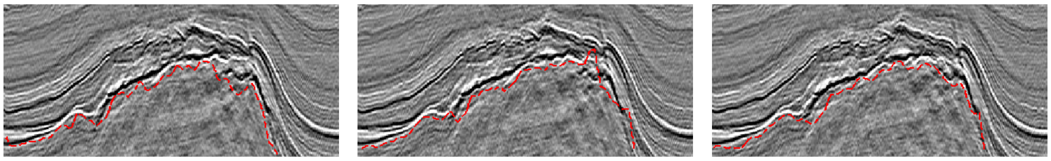

(s) Inline # 129 (t) Inline # 130 (u) Inline # 131

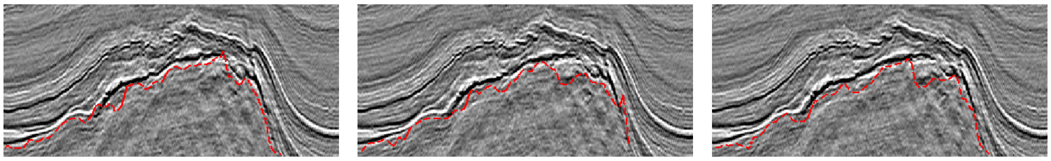

(v) Inline # 132 (w) Inline # 133 (x) Inline # 134

Figure 4.15: Salt boundary detected for the Inlines # 111 to # 134 using the proposed multidirectional edge-based method

4.2 Salt Dome Detection Using A Codebook-based Learning Model

In image processing, visual codebook-based methods have effectively been used for many problems including action identification, object recognition, tracking, segmentation, etc. Codebook-based methods, using local features, are simple, accurate, and computationally efficient. In this section, we present a supervised codebook-based learning model for salt-dome detection in seismic imaging using texture-based attributes. The proposed algorithm is data-driven and overcomes the limitations of existing texture attributes-based salt-dome detection techniques which are heavily dependent upon the relevance of attributes to the geological nature of salt domes and the number of attributes used for classification. The algorithm works by combining the attributes from the Gray Level Co-occurrence Matrix (GLCM) and those from the Gabor filter, with a codebook-based learning approach to delineate salt boundaries in seismic data. The combination of GLCM and Gabor filter based attributes ensures that the algorithm works well even in the absence of strong reflectors along the salt boundary. Contrary to existing salt dome detection techniques, our algorithm works with a codebook of small size and is shown to be robust and computationally efficient. The learning properties of the codebook-based model makes the algorithm flexible and adaptable to the nature of time-scale varying data acquired in seismic surveys. Our experimental results show that the proposed codebook-based workflow can detect salt domes with good accuracy superior to existing salt-dome detection techniques.

4.2.1 Codebook-based Salt Dome Detection Algorithm

The overall structure of the proposed algorithm is shown in Fig. 4.16. The algorithm starts by creating a codebook from the available training data. The training slices are first divided into small patches, a few patches are then selected from salt and non-salt boundary regions. Next, we compute the GLCM and Gabor filter based features for these patches. K-means clustering is then used to quantize the feature vectors. The encoded codewords are concatenated to form a codebook. For a given test slice, the proposed scheme first divides it into small non overlapping patches and computes the GLCM and Gabor features for each patch. By computing the distance between the test patch feature vector and the code-vectors, each patch is classified as either a salt or a non-salt boundary patch. We preliminary outline the salt boundary by classifying all the patches. To get the accurate salt boundary from these classified patches, we use edge strength to detect the correct boundary points within each patch. In what follows, we discuss each of the blocks from Fig. 4.16 in more details.

Gray Level Co-occurance Matrix (GLCM) attributes

The GLCM approximates the joint probability distribution of two gray levels in an image. The high values away from the diagonal in a GLCM reveal sharp gray level changes whereas the high values close to the diagonal reveal small variations in gray levels. The GLCM based attributes discussed by [53] were first applied in [54] to detect salt boundaries. These attributes can detect the changes in texture

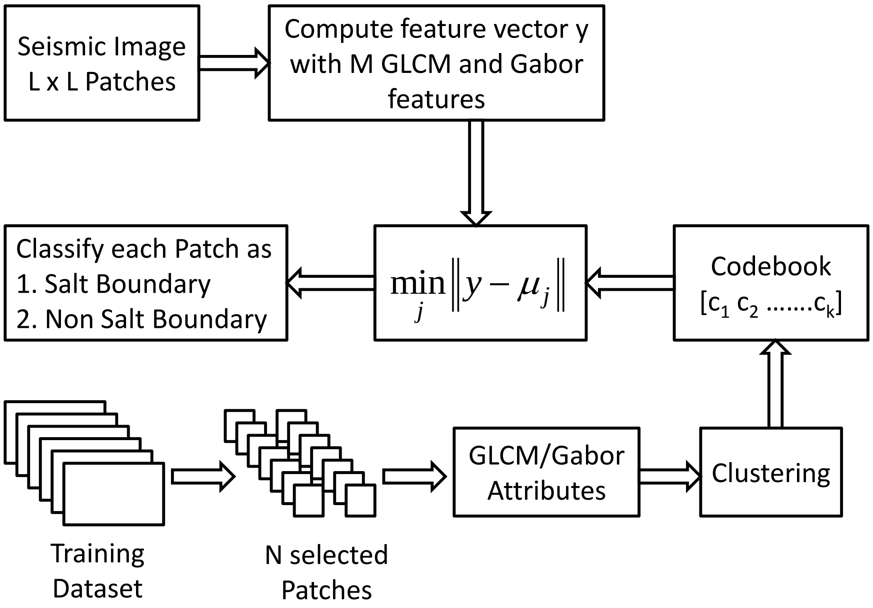

Figure 4.16: Main steps of the proposed codebook-based salt dome detection method

among a pair of pixels along a chosen direction and neighborhood. The joint probability distribution, $P_{GLCM}(i,j)$, is computed as:

$$P_{GLCM}(i,j) = \frac{q_{d,\theta(i,j)}}{\sum_{i,j} q_{d,\theta}(i,j)} \tag{4.22}$$

where $q_{d,\theta}(i,j)$ represents the number of occurrences of gray levels separated by a distance d in direction θ. From the $[P_{GLCM}]$, the following attributes are obtained:

GLCM Contrast: GLCM contrast measures the grey level variations of neighboring pairs in an image:

$$\text{Contrast} = \sum_i \sum_j |i-j|^2 \, P_{GLCM}(i,j) \tag{4.23}$$

GLCM contrast in an image is low if the neighboring points have similar amplitudes. This feature measures local gray level variations (or linear dependencies). Salt regions have smooth texture, therefore, the value of contrast is low for these areas. The value of GLCM contrast is high for salt boundaries which are rich in texture.

GLCM Entropy: GLCM Entropy is a measure of spatial disorder in textures. The GLCM Entropy is computed as:

$$\text{Entropy} = -\sum_i \sum_j P_{GLCM}(i,j) log P_{GLCM}(i,j) \tag{4.24}$$

The value of this attribute is high for dipping reflectors and low for salt areas.

GLCM Dissimilarity: GLCM Dissimilarity is similar to GLCM contrast attribute with a difference in power; contrast unlike dissimilarity grows quadratically. It measures the amplitude variations of neighboring pairs in an image with a maximum value of 1.

$$\text{Dissimilarity} = \sum_i \sum_j |i-j| \, P_{GLCM}(i,j) \tag{4.25}$$

GLCM dissimilarity is low when the neighboring pairs have similar grey levels. The value of this attribute is high along the salt boundaries where we observe large amplitude variations.

GLCM Energy: GLCM Energy is computed as:

$$\text{Energy} = \left[\sum_i \sum_j P_{GLCM}(i,j)^2 \right]^{\frac{1}{2}} \tag{4.26}$$

The value of this attribute is high for strong reflectors along the salt boundary.

In addition to the above attributes, we have also investigated other GLCM-based attributes including homogeneity, inertia, correlation, etc. However, the results were not encouraging due to the geological structure of our data. In Fig. 4.17, we show the maps for the GLCM contrast, entropy, dissimilarity, and energy attributes computed for inline # 354. For our experiments, for the sake of consistency with previous work [8], we have used $d = 1, 2$ and $\theta = 0, \pi/2$.

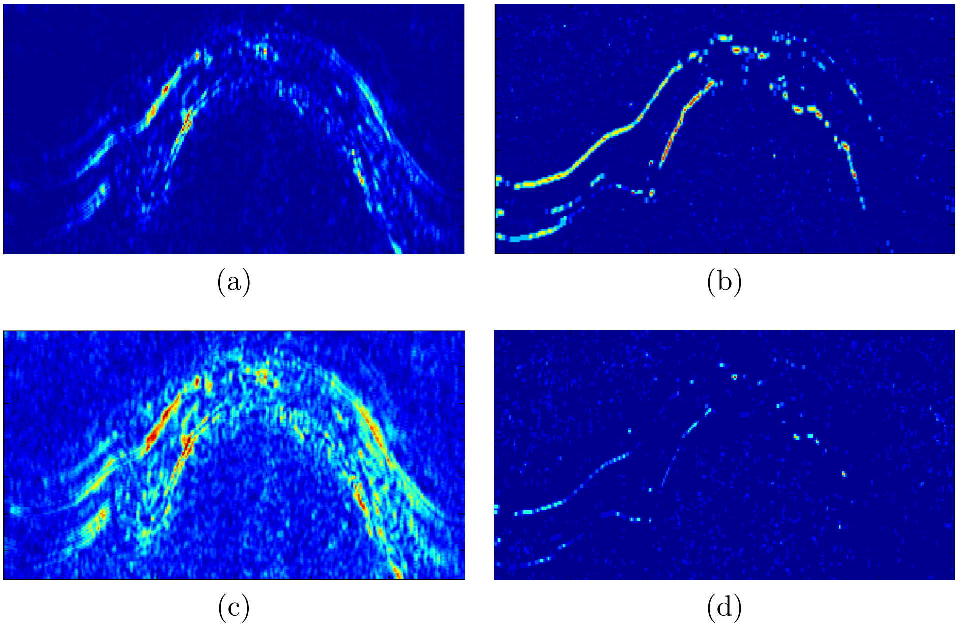

(a) (b) (c) (d)

Figure 4.17: GLCM attributes for inline # 354: (a) Contrast, (b) Entropy, (c) Dissimilarity, (d) Energy

Gabor filter based attributes:

Periodicity and orientation of seismic textures can be described using attributes derived from the Fourier spectrum. Frequency-based texture attributes are used to extract the impact of reflectors. Gabor filters, as discussed in [48], can be used in seismic image processing to extract frequency-based attributes. The normalized energy values computed from the Gabor filtered images were used as the frequency attributes [48]. Different choice of parameters can discriminate between seismic textures with different frequency content. Gabor filters are designed to find the dominant size and orientation of different textures in the image. The Gabor filter with phase ϕ along the x-axis (orientation $= 0^o$) and a given radial frequency F_R is written as:

$$\mathrm{h(x,y)} = exp\left\{-\frac{1}{2}\left[\frac{x^2}{\sigma_x^2}+\frac{y^2}{\sigma_y^2}\right]\right\} cos(2\pi F_R x+\phi) \tag{4.27}$$

For $\phi = 0$, the frequency response is given by:

$$\begin{aligned}\mathrm{H(u,v)} = \frac{8\sigma_u\sigma_v}{\pi}\Bigg(& exp\left(-\frac{1}{2}\left[\frac{(u-F_R)^2}{\sigma_u^2}+\frac{v^2}{\sigma_v^2}\right]\right) \\ & +exp\left(-\frac{1}{2}\left[\frac{(u+F_R)^2}{\sigma_u^2}+\frac{v^2}{\sigma_v^2}\right]\right)\Bigg),\end{aligned} \tag{4.28}$$

where $u = u\cos\theta + v\sin\theta$, $v = -u\sin\theta + v\cos\theta$, θ is the orientation, and $\sigma_u = \frac{1}{2\pi\sigma_x}$ and $\sigma_v = \frac{1}{2\pi\sigma_y}$ specify the filter width. For our experiments, and in consistency with the previous work, we have used $F_R = 2\sqrt{2}$, and $\sigma_x = \sigma_y = 4$. In Fig. 4.18, we show the Gabor filter attributes computed for inline # 354.

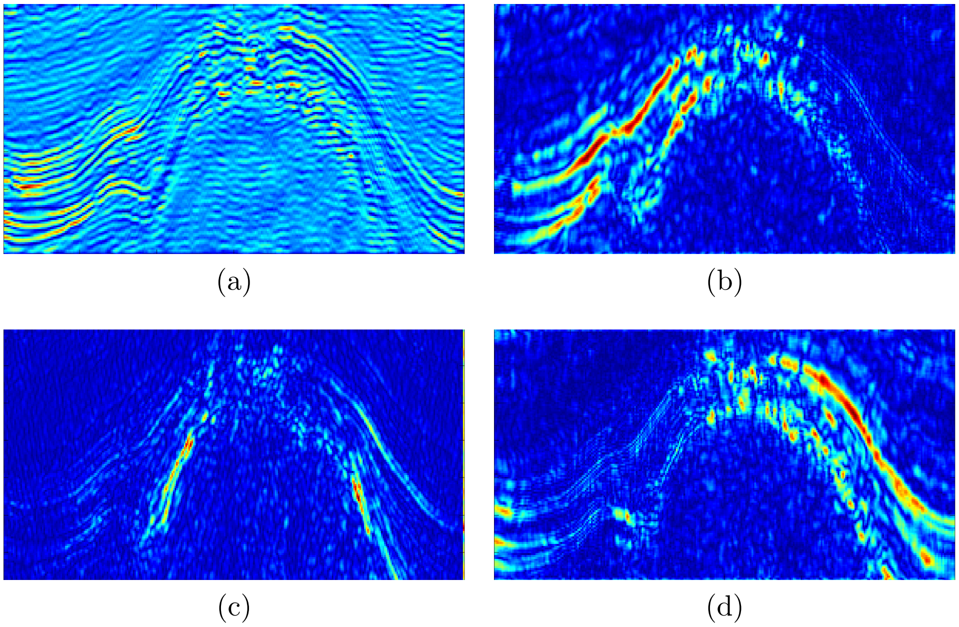
(a) (b) (c) (d)

Figure 4.18: Gabor filter attributes for inline # 354: (a) $\theta = 0$, (b) $\theta = \pi/4$, (c) $\theta = \pi/2$, (d) $\theta = 3\pi/4$

Codebook-based learning model

The basic principle of codebook construction is to use the local features, extracted from the given training data set, and generate a codebook. The K-means algorithm is frequently used to encode the features because of its effectiveness and simplicity. The K centroids, computed by K-means, are the K words in the codebook.

For each training patch, we calculate M features. We use the features estimated from the GLCM and the Gabor filter. For each patch, we compute 4 values ($d = 1, 2$ and $\theta = 0, \pi/2$) for each GLCM attribute and take the average of these values. For the Gabor attributes, we compute one value (average normalized energy) per direction ($\theta = 0, \pi/4, \pi/2, 3\pi/4$) for each patch. In total, we get M=8 attributes. For N training samples, we have a set of training features

$\mathbf{X} = [\mathbf{x}_1\mathbf{x}_2....\mathbf{x}_N] \in \mathbb{R}^{N\times M}$ where $\mathbf{x}_i$ is a training feature vector of size M. From $\mathbf{X}$, we construct a codebook with K words, $\mathbf{C} = [\mathbf{c}_1\mathbf{c}_2....\mathbf{c}_K] \in \mathbb{R}^{K\times M}$. We apply K-means clustering to get the centroids $\boldsymbol{\mu}_1, \boldsymbol{\mu}_2, ...\boldsymbol{\mu}_k$ where $\boldsymbol{\mu} \in \mathbb{R}^M$. Algorithm 1, discussed below, describes the construction of the dictionary while Algorithm 2 outlines the main step of the K-means clustering algorithm. Each cluster center is then used as a codeword in the codebook i.e. $\mathbf{c}_i = \boldsymbol{\mu}_i$. In the final step, all the centroids are concatenated to form the codebook.

Given a test slice, we first divide it into non-overlapping patches of size $L \times L$. For each patch, we compute the feature vector $\mathbf{y} \in \mathbb{R}^M$, containing the GLCM and Gabor attributes. Next, we compute the distance between feature vector $\mathbf{y}$ and codebook-words to classify each patch as either salt boundary or non-salt boundary patch based on simple minimum distance (see Algorithm 3).

Algorithm 1: Codebook Creation

1. From the training dataset, select N patches of size $L \times L$.
2. For each training patch, compute M seismic attributes.
3. From the N patches, we generate $\mathbf{X} = \{\mathbf{x}_1\, \mathbf{x}_2.......\mathbf{x}_N\} \in \mathbb{R}^{N\times M}$ training feature vectors.
4. Apply K-means clustering (See Algorithm 2) on salt and non-salt boundary training feature vectors separately to get K_1 (salt) cluster centroids $\{\boldsymbol{\mu}_1\, \boldsymbol{\mu}_2.......\boldsymbol{\mu}_{K_1}\}$ and K_2 (non-salt) cluster centroids $\{\boldsymbol{\mu}'_1 \boldsymbol{\mu}'_2.......\boldsymbol{\mu}'_{K_2}\}$ where $\boldsymbol{\mu} \in \mathbb{R}^M$, K_1 & $K_2 << N$.

5. Concatenate all the centroid vectors to form the codebook, $\mathbf{C} = \{\boldsymbol{\mu}_1\, \boldsymbol{\mu}_2 ....\boldsymbol{\mu}_K\}$ where $K = K_1 + K_2$.

Algorithm 2: K-means clustering

1. Obtain the learning feature set $\mathbf{X}$, where $\mathbf{X} = \{\mathbf{x}_1\, \mathbf{x}_2 ....\mathbf{x}_N\} \in \mathbb{R}^{N \times M}$.
2. For $n = 1\ \ to\ \ N$

   assign $q_n = k$ for $argmin_k\ \left\| \mathbf{x}_n - \boldsymbol{\mu}_k \right\|^2$
3. For $k = 1\ \ to\ \ K$

$$\boldsymbol{\mu}_k = \frac{\sum_n \mathbf{x}_n . I(q_n)}{\sum_n I(q_n)} \quad where\ \ I(q_n) = 1\ \ if\ \ q_n = k$$

4. Repeat Step 2 and 3 till termination condition reached

Algorithm 3: Proposed Classification Model

1. Divide the input test Inline into non overlapping patches.
2. For each patch, estimate M attributes such that $\mathbf{y_i} \in \mathbb{R}^M$
3. To classify each of the patches, compute the distance between $\mathbf{y_i}$ and the codebook C, and decide on $\underset{j}{min} \left\| \mathbf{y_i} - \boldsymbol{\mu_j} \right\|, j = 1, 2, ..., K$
4. Identify the class (salt or non-salt boundary) for all the patches based on the minimum distance criteria.

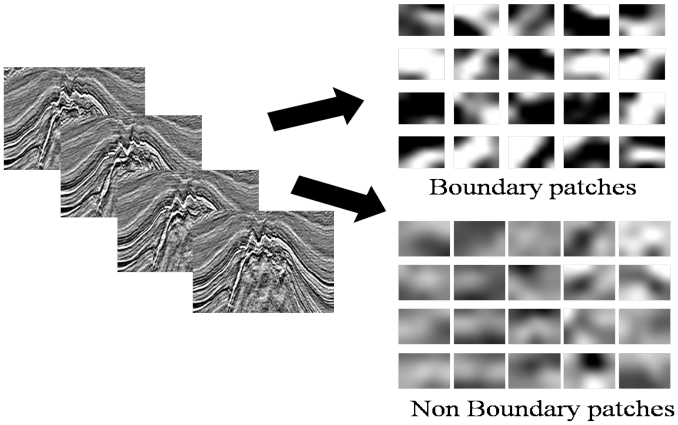

Figure 4.19: Salt and non-salt patches extracted from training data

4.2.2 Experimental Results

We have used the Netherlands offshore F3 block (North Sea) to analyze the performance of our proposed salt-dome detection algorithm. The block covers an area of 24×16 km^2. In the first step, we extracted the training patches (see Fig. 4.19) from labelled salt boundary and non-salt boundary regions. Different inlines were used for training and testing. The training patches were selected equally from the salt boundary and non-salt boundary classes. 200 patches of size $L \times L$ were selected for each class. From experiments, we observed that the maximum accuracy is achieved for $L = 5$. For $L < 5$, the features extracted from the patches are not very accurate as the size of patch is small. For $L > 5$, the accuracy decreases because the features extracted from large patches do not represent accurately local information [10]. For each patch, the proposed algorithm computes the GLCM and the Gabor filter attributes. Next, the codebook is created using Algorithm 1. We have used $M = 8$ and $K = 12$ ($K_1 = K_2 = 6$).

To evaluate the performance of the proposed method, inline # 354 (See

Fig.4.20 (a)) is considered as a test case. The test inline is first divided into non overlapping patches of size 5 x 5. Each patch is then classified as a salt boundary or non-salt boundary patch using the codebook. To detect the salt boundary accurately, we first compute the edge strength for the classified patches using the Sobel operator and select the points that give the maximum edge values. The final boundary is then obtained by linking the missing points using the joining line followed by the smoothing operation [15]. Figure. 4.20 (b) shows the classification result for the salt boundary patches. We see here that most of the boundary patches are correctly classified. Figure 4.20 (c) shows the ground truth (green) and the salt boundary (red) detected for the inline # 354 using the proposed codebook-based approach. We observe that the proposed method is able to detect the salt boundary accurately. Few more examples are provided in Fig. 4.21 for Inlines # 360, 389, 410 and 454 using the proposed method. The proposed algorithm gives excellent results even for the Inline # 454 which has a fault and uneven salt boundary.

We compared the performance of our method with the edge detection based method [2], the texture attributes based method [8], and the dictionary-based salt dome detection method [10]. In Fig. 4.22, we show the salt boundary detected using the proposed method (red), the edge-based method (blue), the texture-based method (pink), and the dictionary-based method (yellow) for inline # 354. The boundary produced by the proposed algorithm closely follows the ground truth (green) whereas the boundary produced by the edge-based and the texture-based methods deviate a lot from the ground truth, especially at the start and along the diagonals. The results of our method are also comparable to the dictionary-based method as shown in Fig. 4.22. The dictionary-based method, however, is not able to detect the points at the end of salt dome where the boundary is represented by weak edges. Note also that the dictionary-based method is computationally very expensive as compared to the proposed method.

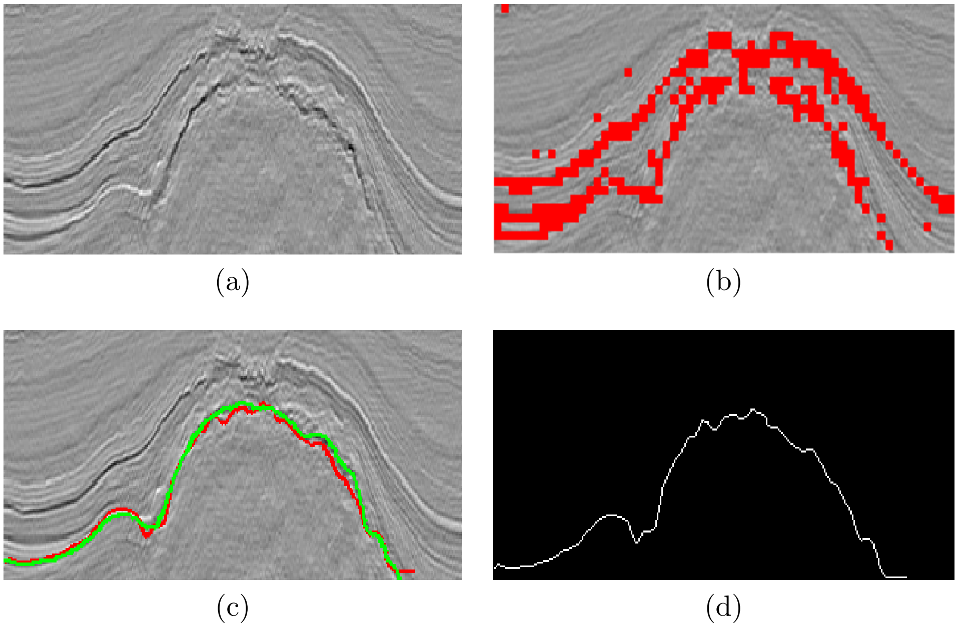
(a)

(b)

(c)

(d)

Figure 4.20: (a) Inline # 354, (b) Salt boundary patches identified using the proposed codebook method, (c) Salt boundary detected (Red), Ground truth (Green) (d) Final detected salt boundary

To further evaluate the performance of the proposed algorithm, we used three objective evaluation metrics, namely, Precision, Recall, and the F-measure. These metrics are commonly used to analyze the performance of image segmentation algorithms. Table 1 shows the average classification accuracy, precision, recall and F-measure values computed for inlines # 350 to 380 using the proposed method, the edge detection based method, the texture attributes based method, and the

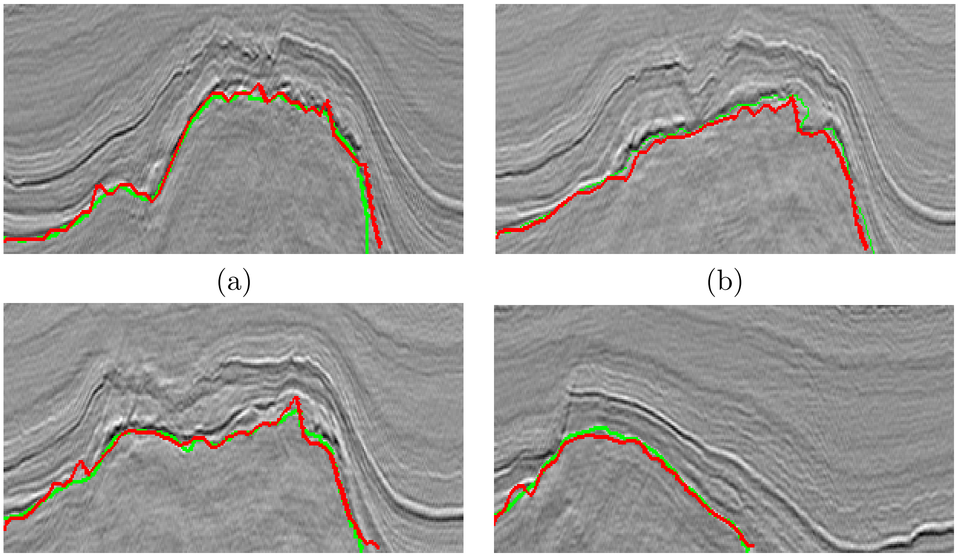
(a) (b)

(c) (d)

Figure 4.21: Salt boundary detected for Inline # (a) 360, (b) 389, (c) 410, (b) 454

dictionary-based method. Here, the classification accuracy is computed using the Normalized Frechet Distance. The proposed codebook-based salt dome detection method gives an average accuracy of 91% which is 10% higher than the edge-based method, 4% higher than the texture-based method, and 1.4% higher than the dictionary-based method. The F-measure value computed for the proposed method is almost 2.5% higher than Sobel edge detector based method, 3% higher than the texture attributes based method, and 1% higher than the dictionary-based method. Overall, the results show that the proposed algorithm performs better than existing techniques.

We see that the performance of our method is slightly better than the traditional dictionary-based method. However, the dictionary-based method is computationally very expensive as it solves an ℓ^1 minimization problem to classify each patch. The proposed codebook-based method, on the other hand, is simple and

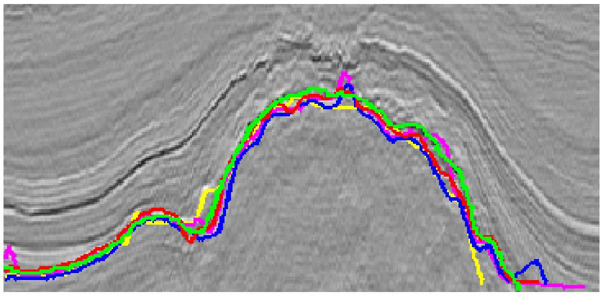

Figure 4.22: Salt boundary detected for inline # 354: Ground truth (Green), Proposed codebook method (Red), Edge-based (Blue), Texture-based (Pink), Dictionary-based (Yellow)

Table 4.3: Accuracy, Precision, Recall, F-Measure of the proposed Codebook method and other methods

Method	Accuracy	Precision	Recall	F-Measure
Proposed method	91.12%	98.94	98.63	98.78
Edge-based [2]	81.23%	97.67	94.62	96.12
Texture-based [8]	87.44%	93.1	98.19	95.60
Dictionary-based [10]	89.74%	98.12	97.28	97.60

computationally very efficient. This can be seen from Table II where we show the running time for both algorithms implemented using a core i-5 machine.

Table 4.4: Execution time: Dictionary & Codebook Methods

Inline	Codebook	Dictionary
Inline # 350	1.61 sec	27.14 sec
Inline # 351	1.62 sec	27.22 sec
Inline # 352	1.56 sec	26.63 sec
Inline # 353	1.57 sec	26.81 sec
Inline # 354	1.59 sec	26.86 sec
Average over Inlines # 350-365	1.60 sec	29.92 sec

In Fig. 4.23, we show the 3D salt volume detected using the proposed codebook-based approach. The algorithm produces smooth salt profiles with good accuracy and fewer variations. The initial feedback received from experts in geophysics, who saw the final salt bodies, have been very encouraging to further pursue our work in this direction. The concept of using learning-based data-driven models for detecting salt domes in seismic volumes can be extended to other events detection such as horizons and faults.

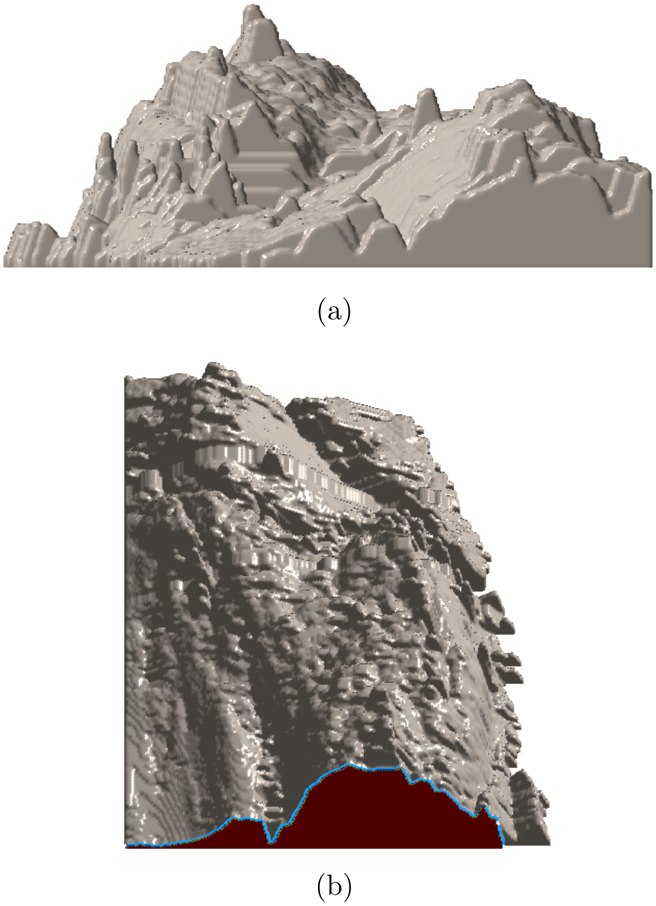
(a)

(b)

Figure 4.23: 3D Salt volume detected using the codebook-based method (a) side view (b) top view

4.3 A Hybrid Approach for Salt Dome Detection in 2D and 3D Seismic Data

Salt boundaries are often characterized by changes in texture rather than reflectivity. Therefore, using only boundary-sensitive attributes such as instantaneous amplitude may result in incorrect interpretation of salt bodies. In this section, we present a hybrid approach based on edge and texture attributes. Although amplitude is an important attribute and helps greatly in detecting salt boundaries, using only one attribute can easily effect the accuracy of the segmentation process. We use a hybrid salt dome detection model in which we combine the most important texture based attributes with the edge based attributes to overcome the weaknesses of existing amplitude based salt dome detection methods. Our experimental results show that the proposed algorithm can detect salt boundaries with high accuracy superior to existing gradient based as well as texture based techniques when used separately.

4.3.1 Salt Dome Detection using Edge and Texture Attributes

The proposed algorithm mainly consists of three steps. First, we apply the 3D edge detection scheme to segment the salt dome. Second, we extract texture based attributes from the seismic data and use these attributes to classify boundary pixels using a multivariate Bayesian classifier. Finally, we combine the results of

3D edge detection and those from the texture based segmentation to get the final segmented salt dome. Fig. 4.24 shows the flowchart for the proposed algorithm. We will now discuss each of these blocks in more details.

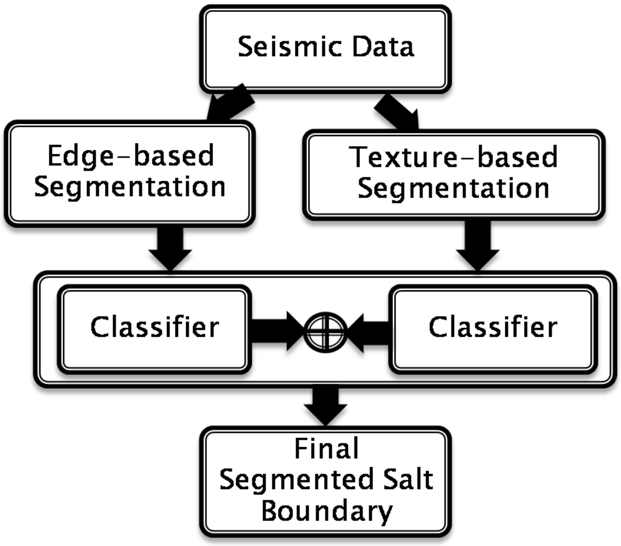

Figure 4.24: Main steps of the proposed hybrid edge-texture based method

3D Edge-based segmentation

Edge detection is one of the most important image processing tasks used to detect pixels intensity variations in an image. The edge detection based techniques are really useful in detecting salt domes in seismic data as the salt dome boundary is generally represented by a strong reflector. Sobel edge detector [20], which computes the first derivative, is the most common operator used in the detection of salt domes. Here, the Sobel operator on 2D slices is extended to 3D taking into account continuity in the medium. The edges from the first trace are first computed. The edge information from this first trace is then used to detect the edges through the remaining slices with reduced computational load. For 2D images, the Sobel gradient in the x direction and y direction is given as:

$$G_x = \begin{bmatrix} -1 & 0 & 1 \\ -2 & 0 & 2 \\ -1 & 0 & 1 \end{bmatrix} G_y = \begin{bmatrix} -1 & -2 & -1 \\ 0 & 0 & 0 \\ 1 & 2 & 1 \end{bmatrix} \tag{4.29}$$

In the case of the 2D Sobel operator, the first mask detects discontinuity in one direction and the second mask detects dissimilarity in the other direction. The boundary of the salt dome is tracked by combining the two dissimilarity maps into a single magnitude map.

Texture-based segmentation

Seismic attributes can reveal texture differences between salt areas and surrounding geology as compared to edge based attributes. A salt structure can be defined as an area of incoherent texture compared to its surroundings. Therefore, using only boundary-sensitive attributes such as instantaneous amplitude may result in incorrect interpretation of salt bodies. Here, we use the texture-sensitive attributes in addition to the boundary-sensitive attributes. The proposed algorithm extracts some selected texture attributes from the seismic data, then uses these attributes to train a classifier. The classifier estimate the probability of each pixel in the seismic image. These probabilities are used to segment the desired salt boundary. The accuracy of the salt boundary is directly linked to the selected texture attributes. Here, we used features extracted from the co-occurrence matrix together with those from the Gabor filter and eigenstructure attributes.

Salt Boundary Classification using texture attributes

For the texture attributes based salt boundary detection, we used a supervised Bayesian classification framework with a multivariate normal distribution. For a test feature vector $\mathbf{x}$, the pdf is given by:

$$P(\mathbf{x}|k) = \frac{1}{(2\pi)^{N/2}\sqrt{\det(\sum_{\mathbf{k}})}}\left[\exp[-\frac{1}{2}(\mathbf{x}-\mu_{\mathbf{k}})^T {\sum}_k^{-1}(\mathbf{x}-\mu_{\mathbf{k}})\right] \tag{4.30}$$

where N is the number of features, k represent the number of classes, and $\mu_{\mathbf{k}}$ and $\sum_{\mathbf{k}}$ are the class mean vectors and covariance matrices.

For a given test vector $\mathbf{x}$, the decision rule on whether $\mathbf{x}$ represents an edge or a non edge pixel is based on the following framework: Decide class i (i=0 for background, i=1 for edges) if

$$P(c_i/\mathbf{x}) > P(c_k/\mathbf{x}) \qquad k = 0, 1\ ; \qquad i \neq k \tag{4.31}$$

The above a posteriori probabilities can be expressed in terms of the a priori probability and the class conditional pdfs $P(\mathbf{x}/c_k)$ using the Baye's theorem:

$$P(c_k/\mathbf{x}) = \frac{P(\mathbf{x}/c_k)P(c_k)}{P(\mathbf{x})} \tag{4.32}$$

Combining edge-based and texture-based results

To get the final boundary, we combine the 3D edge detection result with the classification result from the texture based attributes. The combination is carried at the classifier level. We threshold and take the union of the two boundaries. The edge based boundary gives excellent results when there is a strong reflector but fails if the boundary is represented by a weak reflector. Therefore, by adding the result of texture based detection we ensure that the final segmented boundary tracks the salt dome efficiently under all conditions. The union of two boundaries may result in noisy and disconnected edges. These disconnected edges are removed/linked by using simple morphological operations.

4.3.2 Experimental Results

We tested our salt dome detection method on the Netherlands offshore F3 block acquired in the North Sea which has a resolution of 651 × 951 × 463 (Crossline × Inline × Time). Inline # 375 is considered as a test case. Fig 4.25 shows the Inline # 375 from the F3 block, and the segmented salt dome using 3D Sobel. We can see that the salt dome boundary produced by 3D edge detection based technique is fairly accurate but loses the track where the boundary is not represented by a strong reflector.

Fig 4.26(a) shows the GLCM entropy attribute result for Inline # 375. Fig 4.26(b-d) shows the result of trace, coherency estimate, and the largest eigenvalue attribute for Inline # 375. Fig 4.27 shows the Gabor filter ($\theta = 0, \pi/4, \pi/2, 3\pi/4$)

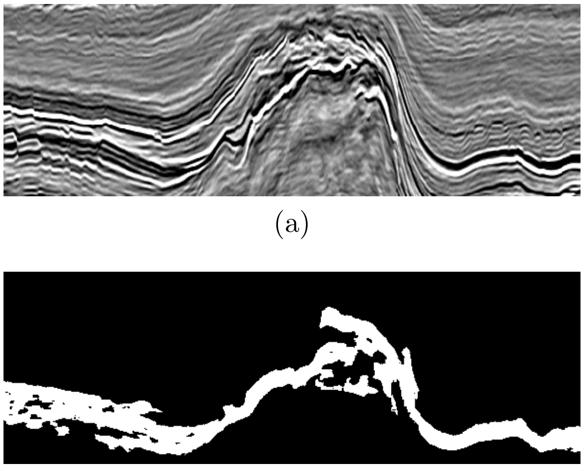

(a)

(b)

Figure 4.25: (a) Inline # 375 (Netherland F3 offshore block) (b) Result of 3D Sobel after thresholding (computational load reduced by a factor of 5)

attributes for Inline # 375. Fig 4.28 (a) shows the result for salt boundary classification for Inline # 375 using texture-based attributes. We see here that most of the boundary points are correctly classified. The output of 3D edge segmentation and texture based segmentation is then combined to achieve more refined boundary. Fig 4.28 (b) shows the final segmented salt dome. We see that the proposed method is able to outline the boundary with excellent accuracy. Two more examples are provided in Fig 4.29 for Inlines # 352 and 355 using the proposed method. The salt boundaries produced by the proposed method are accurate and very close to the ground truth.

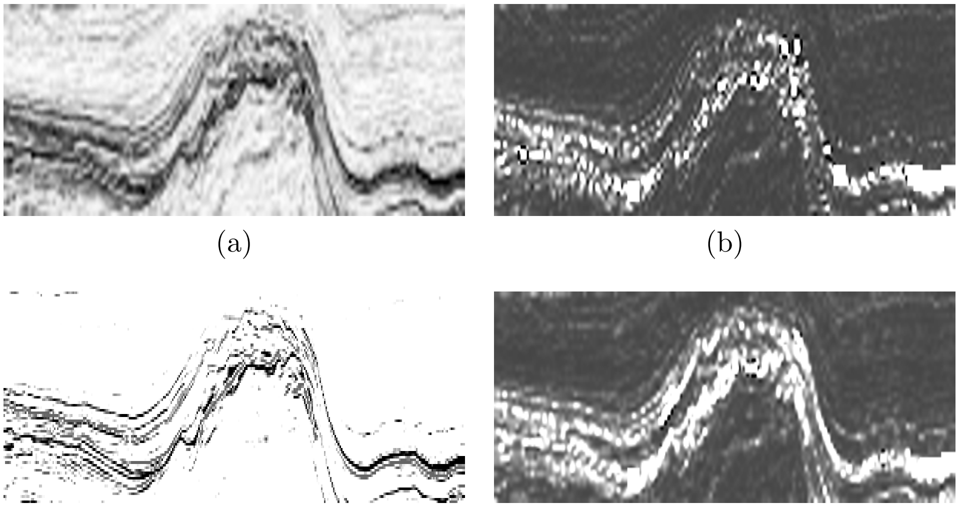

(a) (b)

(c) (d)

Figure 4.26: (a) GLCM entropy attribute result (b) Trace attribute result (c) Coherency estimate (d) Largest eigenvalue attribute

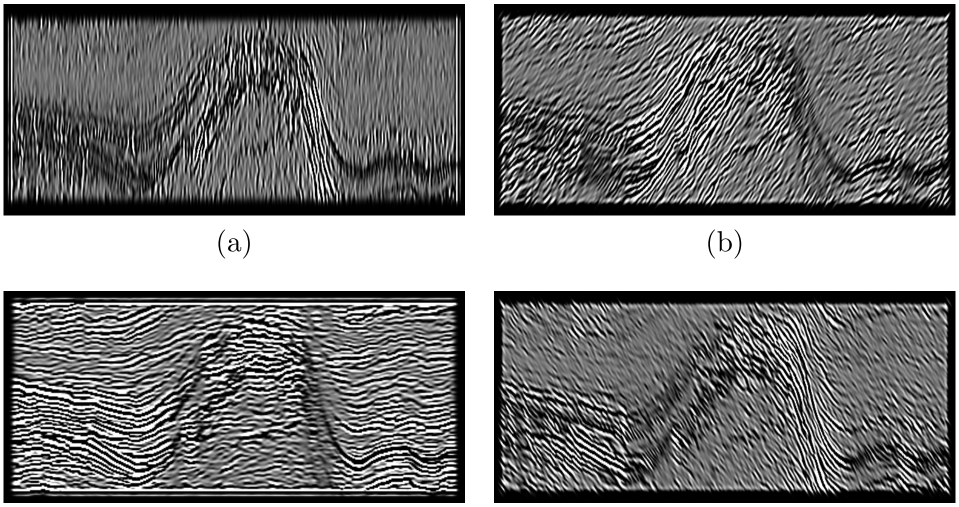

(a) (b)

(c) (d)

Figure 4.27: Gabor filter attributes result $\theta = 0, \pi/4, \pi/2, 3\pi/4$

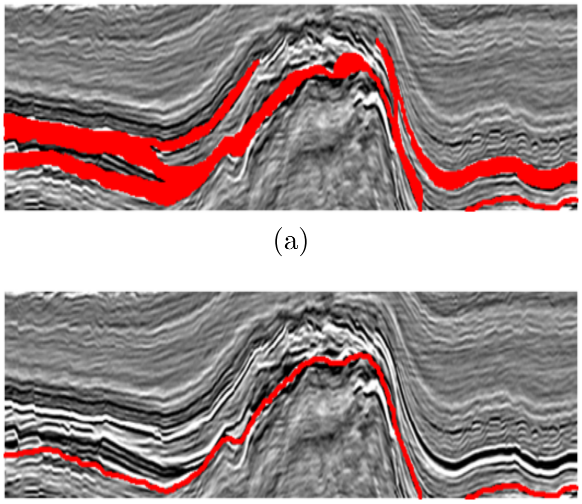

(a)

(b)

Figure 4.28: (a) Classification using texture based attributes (b) Final segmented boundary

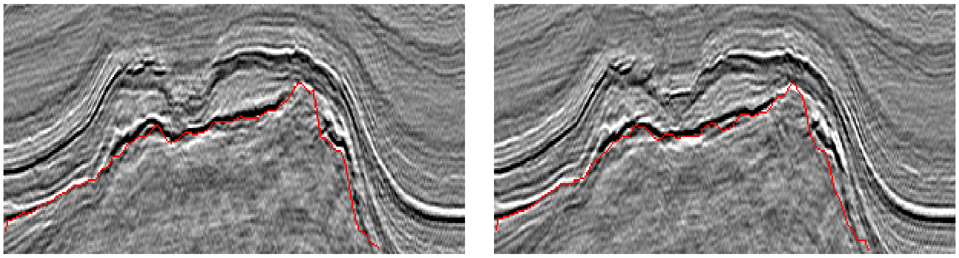

(a)

(b)

Figure 4.29: Final segmented boundary (a) Inline # 352 (b) Inline # 355

4.4 New attributes for Salt Dome Detection in 3D seismic Data using Higher Order SVD

Seismic attributes play a key role in the interpretation process. A good seismic attribute is the one which is directly sensitive to the desired geologic feature or reservoir property of interest. In this section, we present new attributes for seismic interpretation in 3D volumes using Higher Order Singular Value Decomposition (HOSVD). HOSVD based classification methods have effectively been used in many image processing applications such as face recognition, motion analysis, gesture recognition [63]. HOSVD has the advantage of taking into account multidimensional data and therefore can effectively be used for 3D seismic data. We introduce three new attributes for salt dome detection based on the higher-order singular value decomposition (HOSVD) of 3D seismic volumes. These attributes are trace ($Trace_\sigma$), largest singular value (σ_l), and coherence (C_σ). Contrary to many existing attributes that are extracted from 2D windows, the proposed algorithm takes into account the continuity of medium and uses a seismic volume to compute the trace, largest singular value, and coherence attributes. These attributes can be used for detecting salt domes, horizons, chaotic horizons, and faults. In this work, we focus mainly on the problem of salt dome detection in 3D seismic data. The proposed workflow uses the estimated attributes from the inline, crossline and time directions. A combination of these attributes ensures that the proposed algorithm works well even when the salt boundary is represented by weak reflectors. The newly introduced attributes based on HOSVD are shown to produce excellent results as compared to other existing attributes that are being used in seismic interpretation specially the ones based on 2D profiles.

4.4.1 Proposed Seismic Interpretation Workflow

The proposed workflow works by dividing the given 3D seismic volume into small overlapping volumes of size I × J × K. For each pixel p, in the given seismic data, we extract a cube of size I × J × K such that p is the center of the cube. The cube is then unfolded along the inline, crossline, and time directions to create three 2D matrices. The trace, largest singular value, and coherence attributes are calculated for each of the unfolded matrix using the concept of HOSVD. The attributes computed along the different dimensions are combined and thresholded to get the segmented salt dome boundary. Erosion and dilation operations are used to remove the unwanted small noisy patches.

Trace attributes, computed from the covariance matrix, were first proposed in [43] for salt dome detection. The covariance matrix was obtained from the gradients in x, y and z directions. However, the performance of this attribute depends on the strength of edges in different directions and may not give good results for weak edges. In this paper, we compute the trace attribute by unfolding the 3D volume in inline, crossline and time directions thus taking into account the geological structure of the 3D seismic volume. The proposed trace attribute gives high values along the salt boundary where we have large amplitude variations and low values for salt regions which exhibit smooth textures. The proposed largest singular value attribute represents the energy information. The values of this attribute are high for strong edges and low for weak edges and smooth areas. The proposed coherence attribute give low values for high contrast regions and high values for smooth areas.

HOSVD based attributes

Tensors are multimode or multidimensional arrays. An Nth-order tensor, $A \in R^{I_1 \times I_2 \times \dots \times I_N}$, is a multidimensional array of N dimensions where I_m is the upper limit of the m_{th} dimension. In the literature, the order of a tensor is also referred as mode. A vector is therefore a tensor of first order, a matrix is a tensor of 2nd order, and a 3D volume is a tensor of 3rd order. 3D seismic data, $S \in R^{I \times J \times K}$, can be considered as a tensor of 3rd order (See Fig 4.30) where I, J and K corresponds to the dimensions of Inline, crossline and time/depth respectively.

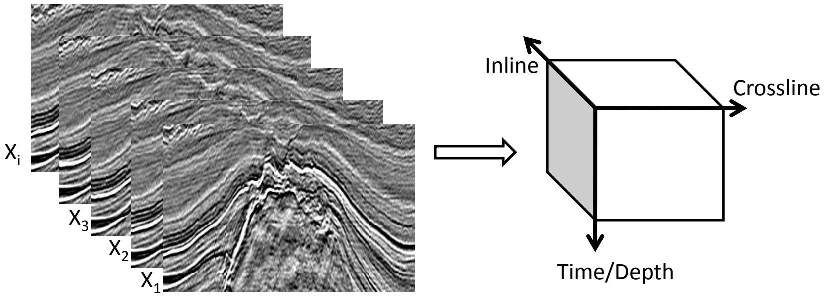

Figure 4.30: 3D seismic data as 3rd order tensor

For simplicity, tensors can be decomposed into sub-tensors: fibers (single dimensional) or slices (two dimensional). Fibers are column vectors defined by fixing every index of higher order tensor except one. In case of 3rd order tensor, column, row and depth are the mode-1, mode-2, and mode-3 fibers of the tensor.

For 3D seismic data, the mode-1 represents crossline, mode-2 represents inline, and mode-3 represents time information. Slices are two dimensional structures, extracted from higher order tensor, by fixing every index except two. We can form three structure of slices, horizontal, lateral, and frontal, from a 3rd order tensor by fixing I, J, and K respectively. In Fig 4.32, we show the decomposition of 3rd order tensor into fibers and slices.

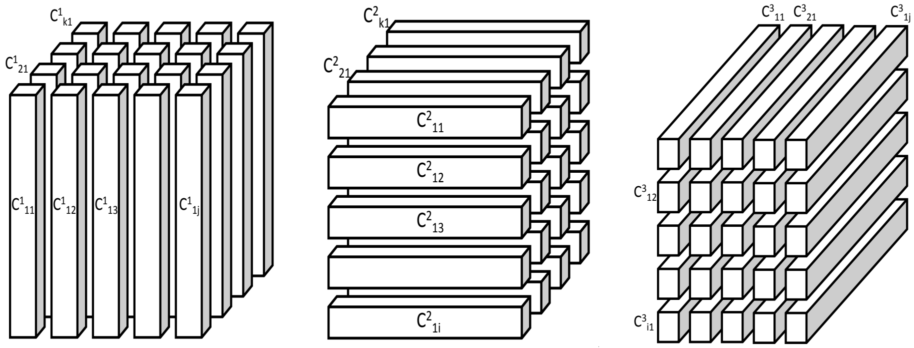

(a) (b) (c)

Figure 4.31: Fibers modes: (a) Crossline (b) Inline (c) Time

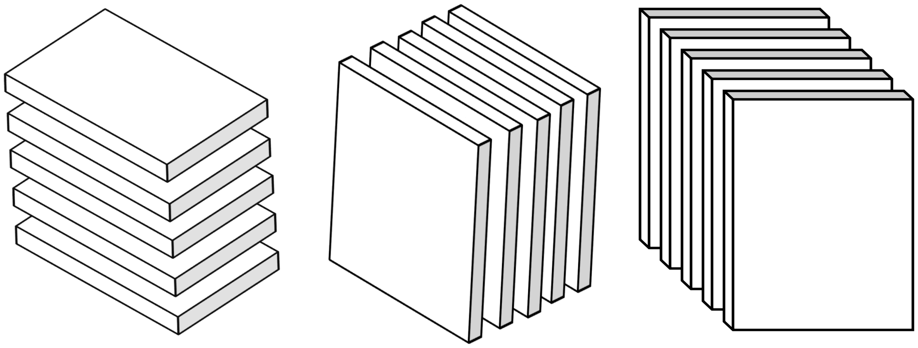

(a) (b) (c)

Figure 4.32: (a) Horizontal slices (b) Lateral slices (c) Frontal slices

To extract useful information from higher order tensors, such as singular values based features, matricizing/unfolding of tensors needs first to be performed. The mode-n matricizing of a tensor, denoted as A(n), is done by aligning mode-n fibers of tensor and concatenating them to form a two dimensional matrix. The resultant unfolded matrix is used for HOSVD. The matricizing of a third order tensor is defined as:

$$\begin{aligned} A_{(1)} &= \left[c^1_{11}\ c^1_{12}\ ...\ c^1_{1j}\ \ c^1_{21}\ ...\ c^1_{2j}\ ...\ c^1_{kj}\right] \\ A_{(2)} &= \left[c^2_{11}\ c^2_{12}\ ...\ c^2_{1i}\ \ c^2_{21}\ ...\ c^2_{2i}\ ...\ c^2_{ki}\right] \\ A_{(3)} &= \left[c^3_{11}\ c^3_{12}\ ...\ c^3_{1j}\ \ c^3_{21}\ ...\ c^3_{2j}\ ...\ c^3_{ij}\right] \end{aligned} \tag{4.33}$$

For the 3D seismic data shown in Fig 4.30, we can unfold the data using the following equations.

$$\begin{aligned} A_{(1)} &= [X_1 \quad X_2 \quad X_3 \ \ ... \quad X_i] \\ A_{(2)} &= \left[X_1^{'} \quad X_2^{'} \quad X_3^{'} \ \ ... \quad X_i^{'}\right] \\ A_{(3)} &= \left[(X_1(:))^{'}\ \ (X_2(:))^{'}\ \ ...\ \ (X_i(:))^{'}\right] \end{aligned} \tag{4.34}$$

Fig. 4.33 shows an example of 3D seismic volume unfolded across inline and crossline directions. The singular value decomposition (SVD) of a matrix is a

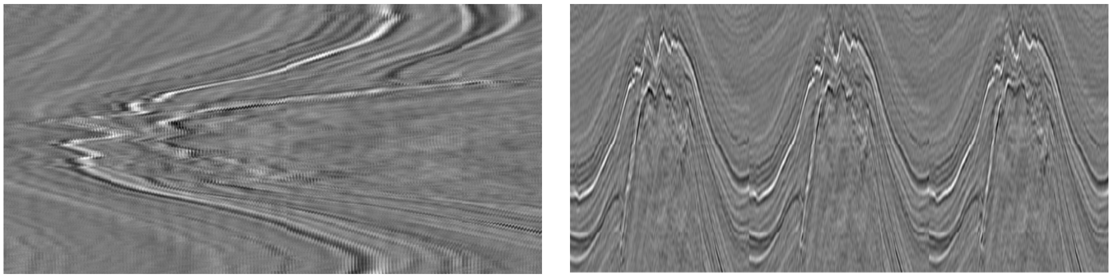

(a) (b)

Figure 4.33: 3D seismic volume unfolded across (a) Crossline (b) Inline

very useful tool in many applications. A 2D matrix $X \in R^{I \times J}$, with $I \geq J$, can be expressed using SVD as: $X = USV^T$ where $U \in R^{I \times I}$ and $V \in R^{J \times J}$ are the orthogonal left and right singular matrices and $S \in R^{I \times J}$ is a diagonal matrix containing J singular values such that $\sigma_1 \geq \sigma_2 \geq ..... \geq \sigma_J$.

HOSVD is used to decompose tensors of third or higher order. The nth order tensor is first unfolded using the matricizing operation discussed above. SVD is then computed for each unfolded matrix. For the 3rd order tensor, SVD is computed for three unfolded matrices i.e. $A_{(1)}, A_{(2)}$, and $A_{(3)}$.

$$\begin{aligned} A_{(1)} &= U^{(1)} S^{(1)} (V^{(1)})^T \\ A_{(2)} &= U^{(2)} S^{(2)} (V^{(2)})^T \\ A_{(3)} &= U^{(3)} S^{(3)} (V^{(3)})^T \end{aligned} \tag{4.35}$$

Here, $S^{(i)}$ is the diagonal matrix containing the singular values for mode-i unfolded matrix. From $S^{(i)}$, we compute the following attributes:

Trace Attribute: The singular values of the matrix $S^{(i)}$ are used to obtain the trace attribute:

$$\mathrm{Trace}_{\sigma}^{\mathrm{(i)}} = \sum diag(S^{(i)}) = \sum_j \sigma_j^{(i)} \tag{4.36}$$

where $\sigma_j^{(i)}{}'s$ are the singular values of the matrix $S^{(i)}$. Strong reflections from salt domes and horizons create amplitude variations across the boundary whereas the profile of salt areas is relatively smooth. Therefore, this attribute gives large

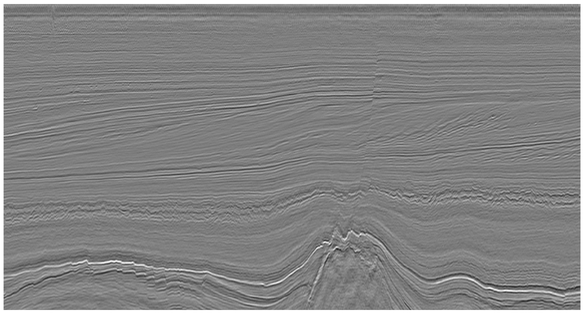

Figure 4.34: Inline # 330 from F3 dataset

values along the boundary and low values for non-boundary regions.

Largest singular value: The largest singular value attribute is computed as:

$$\sigma_l^{(i)} = max(diag(S^{(i)})) \tag{4.37}$$

where $\sigma_l^{(i)}$ is the largest singular value. Salt boundaries and horizons are often represented by strong edges in seismic data. The proposed largest singular value attribute represents edge strength in a chosen volume. The value of this attribute is high for boundaries represented by strong edges and weak for surrounding areas.

Coherence Attribute: The Coherence attribute is the ratio of the trace attribute and the largest singular attribute. The coherence attribute is computed as:

$$C_\sigma^{(i)} = \frac{\sigma_l^{(i)}}{Trace_\sigma^{(i)}}, \tag{4.38}$$

Coherence attribute gives the contrast information present in seismic slices. The attribute exhibits strong values for the smooth areas and low values across the salt boundaries where we usually have high amplitude variations.

In Fig 4.35, 4.36, and 4.37, we show the trace attribute, the largest singular value attribute, and the coherence attribute computed for Inline # 330. Here we have chosen the size of 3D cube as 5 x 5 x 3 (inline x crossline x time). We see that the attribute extracted from $S^{(1)}$ (across inline) and $S^{(2)}$ (across crossline) gives very good result for salt dome and horizons. However, the trace, largest singular value, and coherence attribute computed from $S^{(3)}$ (across time) do not differentiate accurately between salt boundary and other regions. This is mainly because of the geological structure of the salt dome in our dataset. Therefore, for our salt dome detection experiments we have only used the attribute extracted from $S^{(1)}$ and $S^{(2)}$. However, the trace and largest singular attribute computed from $S^{(3)}$ highlights the chaotic horizons. The coherence attribute computed from $S^{(1)}$ and $S^{(2)}$ give low values for fault regions and high for the surroundings.

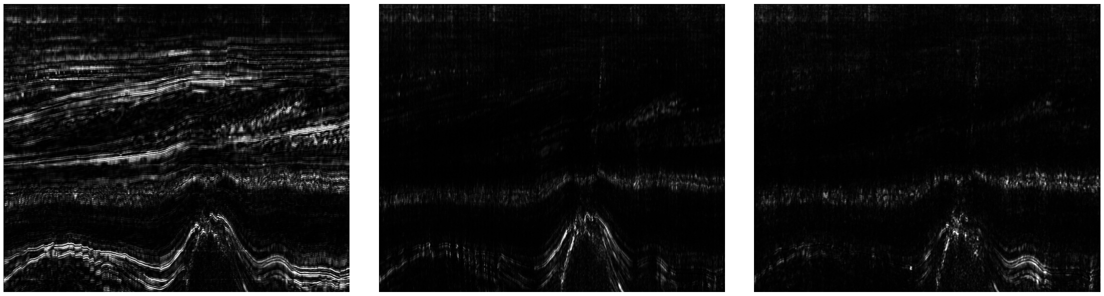
(a) (b) (c)

Figure 4.35: (a) Inline # 330 (F3 Block), Trace attribute: (b) $S^{(1)}$ (inline), (c) $S^{(2)}$ (crossline), (d) $S^{(3)}$ (time)

4.4.2 Experimental Results

We tested our seismic interpretation workflow, using the HOSVD based attributes, on the F3 block which covers an area of 24 x 16 km^2. For each point in a test inline,

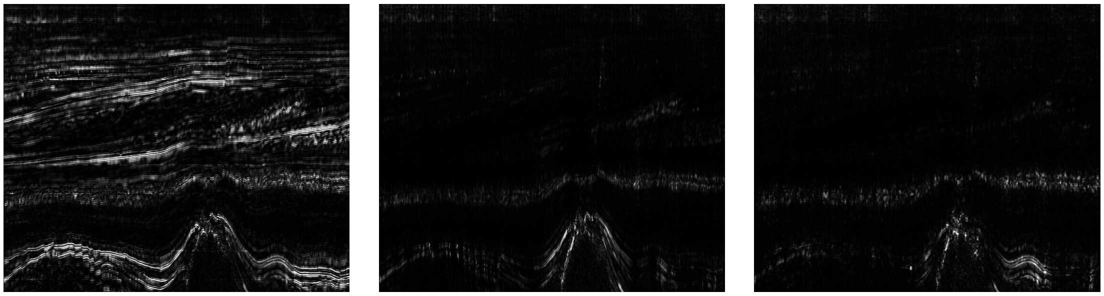
(a) (b) (c)

Figure 4.36: (a) Inline # 330 (F3 Block), Largest singular value attribute: (b) $S^{(1)}$ (inline), (c) $S^{(2)}$ (crossline), (d) $S^{(3)}$ (time)

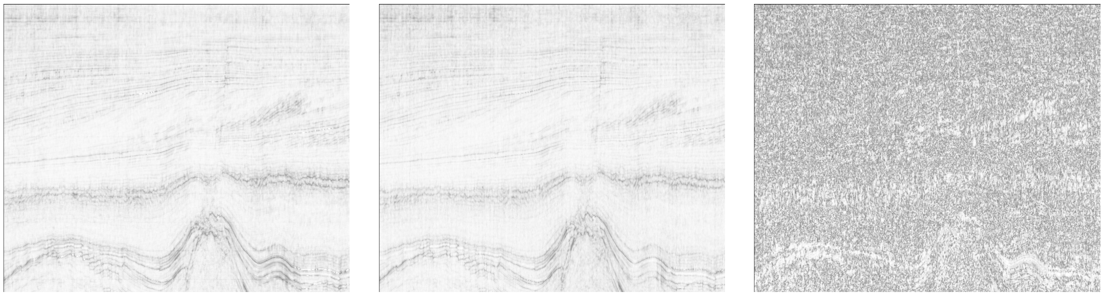
(a) (b) (c)

Figure 4.37: (a) Inline # 330 (F3 Block); Coherence attribute: (b) $S^{(1)}$ (inline), (c) $S^{(2)}$ (crossline), (d) $S^{(3)}$ (time)

we extract a volume of size 5 × 5 × 3 (inline x crossline x time). The volume is then unfolded along inline, crossline, and time directions using the concept of tensors as discussed in the previous section. From the unfolded matrix, we compute the trace, largest singular value, and coherence attributes. For each pixel we get 9 attributes: $Trace_{\sigma}^{(1)}$, $\sigma_l^{(1)}$, and $C_{\sigma}^{(1)}$ from $S^{(1)}$, the unfolded matrix along the inline, $Trace_{\sigma}^{(2)}$, $\sigma_l^{(2)}$, and $C_{\sigma}^{(2)}$ from $S^{(2)}$, the unfolded matrix along the crossline dimension, and $Trace_{\sigma}^{(3)}$, $\sigma_l^{(3)}$, and $C_{\sigma}^{(3)}$ from $S^{(3)}$, the unfolded matrix along the time dimension.

Salt Dome Detection

In Fig. 4.38, we show the trace attribute, the largest singular value attribute, and the coherence attribute maps computed for inline # 360. Here we have chosen the size of 3D cube as 5 × 5 × 3 (inline × crossline × time). We see that the attribute extracted from $S^{(1)}$ (across inline) and $S^{(2)}$ (across crossline) gives very good result. However, the trace, largest singular value, and coherence attribute computed from $S^{(3)}$ (across time) do not differentiate accurately between salt boundary and other regions. Therefore, for the proposed salt dome detection algorithm, we use only the attributes extracted from $S^{(1)}$ and $S^{(2)}$. To improve the computational accuracy, we have used here a classifier-independent approach.

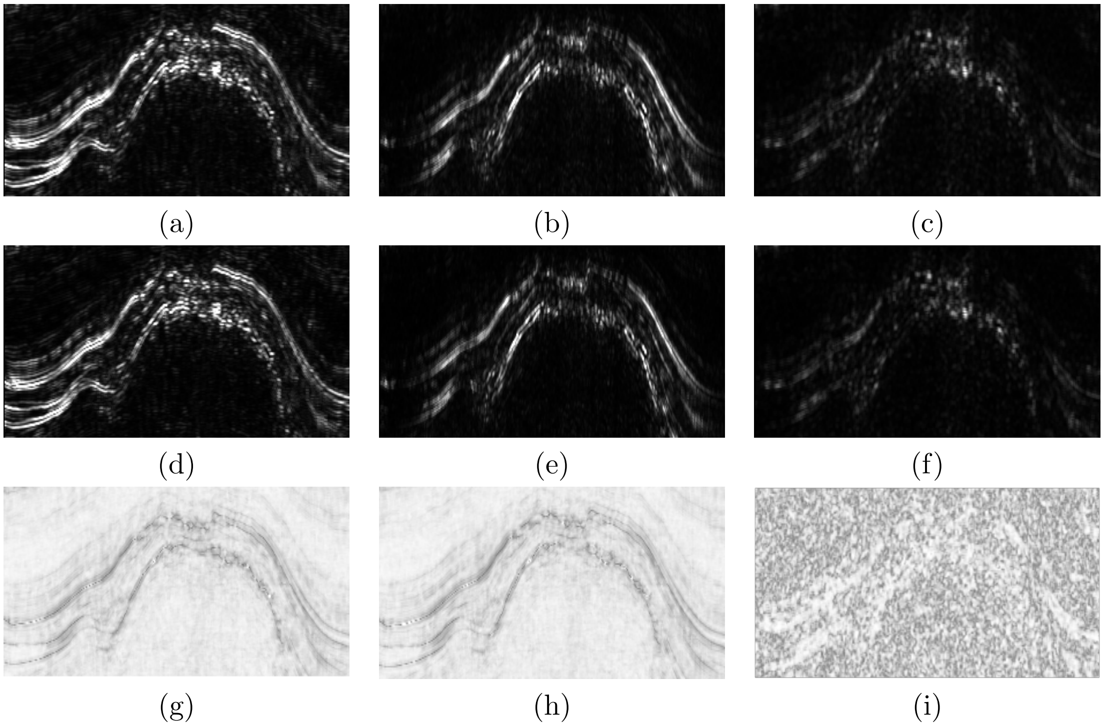

Figure 4.38: (a) Salt dome section (Inline # 360), Trace attribute: (b) $S^{(1)}$ (inline), (c) $S^{(2)}$ (crossline), (d) $S^{(3)}$ (time), Largest singular value attribute: (e) $S^{(1)}$ (inline), (f) $S^{(2)}$ (crossline), (g) $S^{(3)}$ (time), Coherence attribute: (h) $S^{(1)}$ (inline), (i) $S^{(2)}$ (crossline), (j) $S^{(3)}$ (time)

We normalize the six attributes and add them to get one Cumulative Hybrid Seismic Attribute ($CHSA$):

$$\begin{aligned}\text{CHSA} = &\frac{Trace_\sigma^{(1)}}{max(Trace_\sigma^{(1)})} + \frac{\sigma_l^{(1)}}{max(\sigma_l^{(1)})} + \left(1 - \frac{C_\sigma^{(1)}}{max(C_\sigma^{(1)})}\right) \\ &+ \frac{Trace_\sigma^{(2)}}{max(Trace_\sigma^{(2)})} + \frac{\sigma_l^{(2)}}{max(\sigma_l^{(2)})} + \left(1 - \frac{C_\sigma^{(2)}}{max(C_\sigma^{(2)})}\right)\end{aligned} \tag{4.39}$$

Next, we threshold $CHSA$. The threshold value is set empirically through extensive experiments. After thresholding, we remove the small unwanted regions using erosion and dilation operations with a diamond shaped mask of size 4 x 4. In Fig 4.39 (a-b), we show the accumulative attribute $CHSA$ after thresholding and the outline of the boundary detected in inline using the proposed method. In figure 4.39 (c-d), we show the boundary detected using the proposed method and the ground truth for the inline # 360. The proposed salt dome detection based method, using HOSVD features, is able to detect the salt boundary with good accuracy.

We compare the performance of our proposed method with the egde detector based method [3], the texture attributes based method [8], the hybrid edge and texture based method [9], the patch based classification method [10], and the 3D gradient of texture (GoT) method [11]. The texture attributes based salt dome detection method [8] uses the GLCM based attributes, the Gabor filter based attributes, and the eigenstructure based attributes. This method has traditionally been used in previous papers for benchmarking purposes. In Fig 4.40, we show

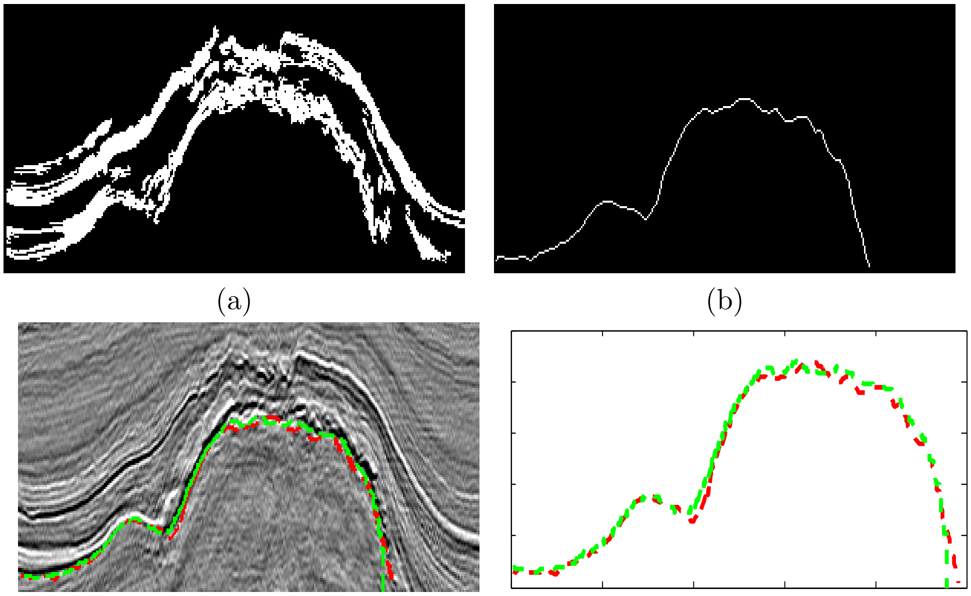
(a)

(b)

(c)

(d)

Figure 4.39: (a) Combined attribute $CHSA$ for inline # 360, (b) Outline of the detected boundary (c-d) Salt boundary detected in inline # 360 (Red) Ground truth (Green)

the results of the salt boundary detected using the proposed method (red), egde detection based method (Black), texture attributes based method (Cyan), hybrid edge texture method (Purple), patch based method (Yellow), and 3D GoT method (Blue). The edge detector based method deviates a lot along the diagonals and at the end where the boundary is not represented by strong reflectors. The salt boundary detected by the texture attributes based method also loses the track at many points especially when the texture of salt boundary resembles to the horizon. The hybrid edge texture method is able to trace the boundary accurately except for the diagonals and the end points of salt dome. The patch-based classification method considers the lower portion of classified patches as salt boundary, therefore this method is not able to produce smooth results as can be seen in Fig. 17. The 3D GoT method misses some points at the start and end of salt dome and also

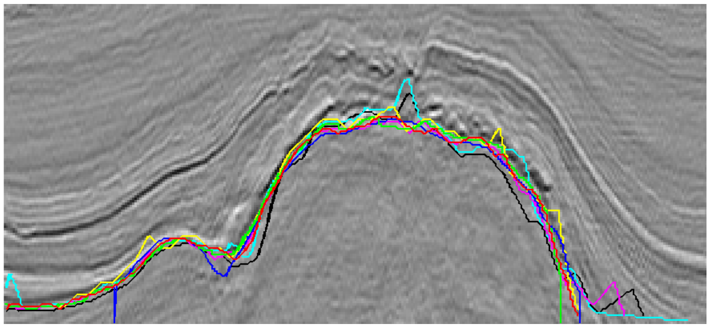

Figure 4.40: Salt boundary detected in inline # 360 using the proposed HOSVD method(Red), Edge-based [3] (Black), Texture-based [8] (Cyan), Hybrid edge texture (Purple) [9], Patch-based (Yellow) [10], 3D GoT (Blue) [11], Ground truth (Green)

produces some over-segmented regions.This shows the superior performance of our proposed attributes over the existing attributes used for the salt dome detection i.e. GLCM, Gabor filter and eigenstructure based.

We show in Table 1 the average classification accuracy for Inlines # 350 to 360 using the proposed method, the edge detector based method, the texture based method, the hybrid edge texture method, the patch-based method, and the 3D GoT method. We have used the normalized frechet distance to calculate the classification accuracy. The proposed HOSVD based salt dome detection method gives an average accuracy of 90.34% which is 4% higher than the edge based method [3], 3% higher than the texture based method [8], 2% higher than the patch-based method [10] and 3D GoT method [11], and 1% higher than the hybrid edge texture method [9].

Table 4.5: Classification Accuracy of the proposed HOSVD-based method and other methods

Method	Classification Accuracy
Proposed method	90.34%
Edge based detector [3]	86.76%
Texture attributes [8]	87.78%
Hybrid Edge Texture [9]	89.61%
Patch-based [10]	88.76%
3D GoT [11]	88.48%

Fault, Horizon and Chaotic Horizon Labeling

In addition to salt domes, the proposed HOSVD-based attributes can also be used to detect faults, horizons, and chaotic horizons. Faults are represented by discontinuities in seismic data and the area around fault exhibits contrast variations (See Fig. 4.41 (a)). Therefore the coherence attribute, that measures the contrast information, can be used to highlight the fault regions. In Fig. 4.41, we show the trace, largest singular value, and coherence attributes computed for fault section along the inline, crossline and time directions. We observe here that the coherence attribute computed along the inline and crossline directions highlights the fault region with good accuracy. The trace and largest singular value attribute computed along the crossline direction also give high value values for fault regions and can be used in fault detection workflow for accurate labeling of faults.

Horizons are the events that appear as strong edges in seismic data (See Fig. 4.42 (a)). The trace and the largest singular value attributes, which measure the edge strength, can be used to detect horizons. In Fig. 4.42, we show the trace, largest singular value, and coherence attributes computed for horizon section along the inline, crossline, and time directions. The trace and largest singular value attribute computed along the inline direction differentiate accurately between the horizons and surrounding areas.

Chaotic horizons appear in seismic data as a combination of noisy texture and weak edges (See Fig. 4.43 (a)). Therefore, a combination of the trace, largest singular value, and coherence attributes can be used to detect chaotic horizons. In Fig. 4.43, we show the trace, largest singular value, and coherence attributes computed for chaotic horizon section along the inline, crossline, and time directions. We observe here that the trace and largest singular value attributes computed along the crossline and time directions and the coherence attribute computed along the inline and crossline directions are able to segment the chaotic horizons accurately. Therefore, these attributes can be used in chaotic horizon detection workflow to achieve excellent accuracy.

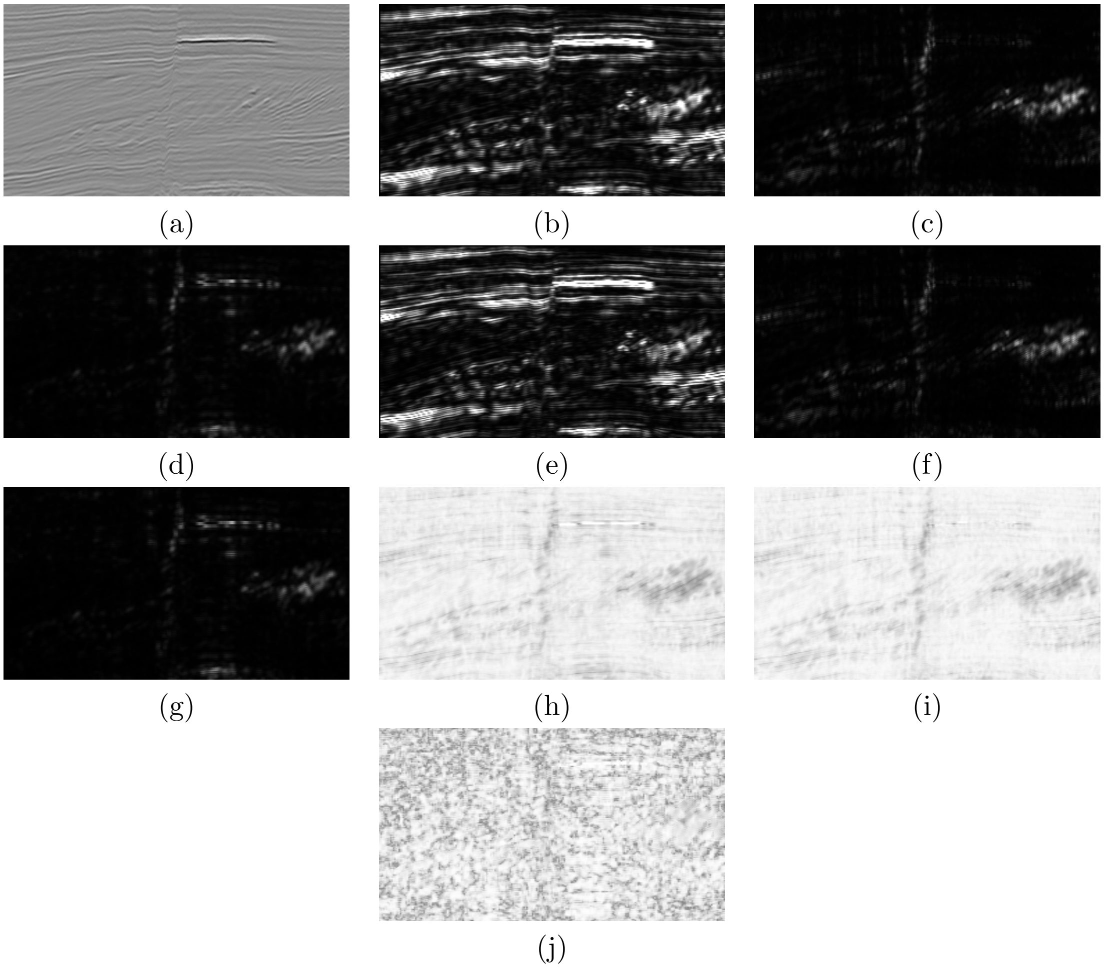

(a) (b) (c) (d) (e) (f) (g) (h) (i) (j)

Figure 4.41: (a) Fault section (Inline # 330), Trace: (b) $S^{(1)}$ (inline), (c) $S^{(2)}$ (crossline), (d) $S^{(3)}$ (time), Largest singular value: (e) $S^{(1)}$ (inline), (f) $S^{(2)}$ (crossline), (g) $S^{(3)}$ (time), Coherence: (h) $S^{(1)}$ (inline), (i) $S^{(2)}$ (crossline), (j) $S^{(3)}$ (time)

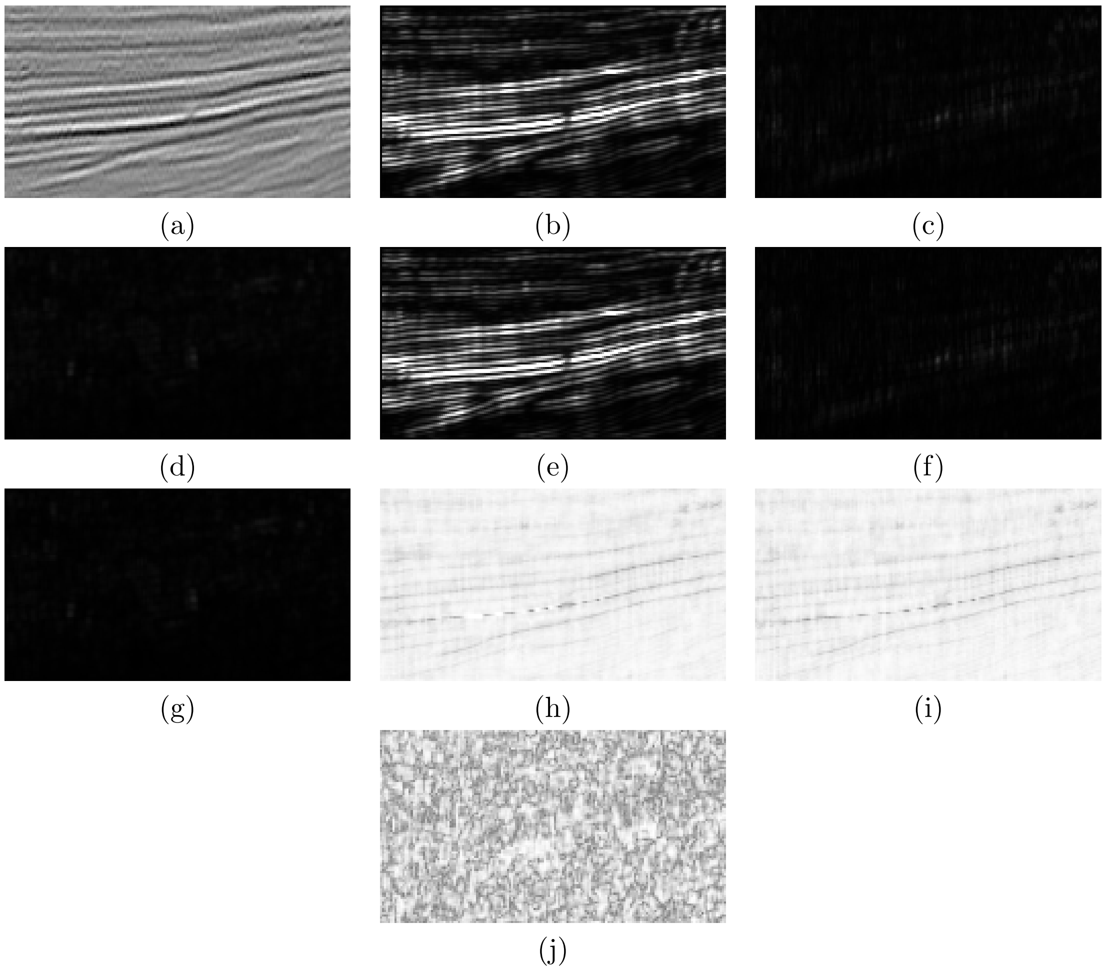

Figure 4.42: (a) Horizon section (Inline # 330), Trace: (b) $S^{(1)}$ (inline), (c) $S^{(2)}$ (crossline), (d) $S^{(3)}$ (time), Largest singular value: (e) $S^{(1)}$ (inline), (f) $S^{(2)}$ (crossline), (g) $S^{(3)}$ (time), Coherence: (h) $S^{(1)}$ (inline), (i) $S^{(2)}$ (crossline), (j) $S^{(3)}$ (time)

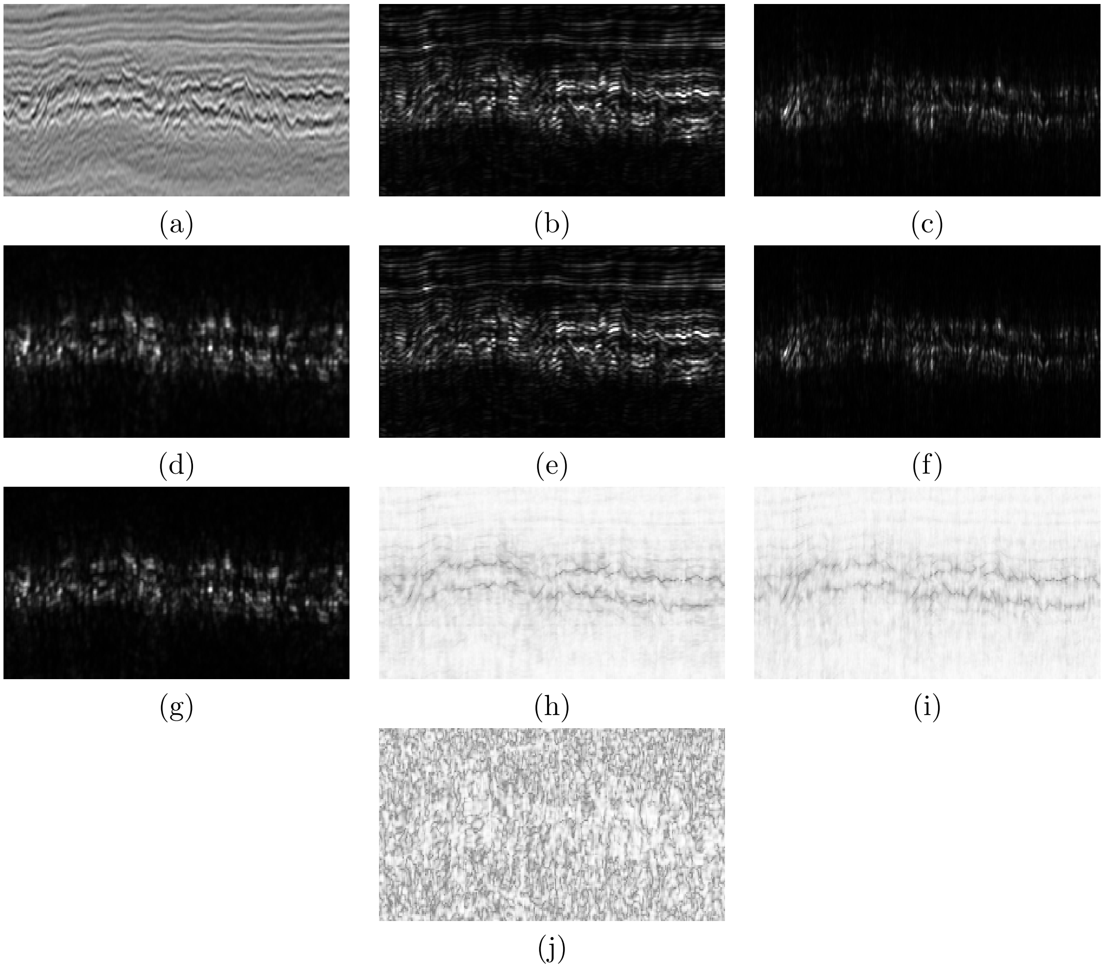

(a) (b) (c) (d) (e) (f) (g) (h) (i) (j)

Figure 4.43: (a) Chaotic horizon section (Inline # 330), Trace: (b) $S^{(1)}$ (inline), (c) $S^{(2)}$ (crossline), (d) $S^{(3)}$ (time), Largest singular value: (e) $S^{(1)}$ (inline), (f) $S^{(2)}$ (crossline), (g) $S^{(3)}$ (time), Coherence: (h) $S^{(1)}$ (inline), (i) $S^{(2)}$ (crossline), (j) $S^{(3)}$ (time)

CHAPTER 5

AUTOMATED SALT DOME DETECTION USING AN ATTRIBUTE RANKING FRAMEWORK WITH A DICTIONARY-BASED CLASSIFIER

Salt domes are an important diapir shaped structures in the Earth subsurface that have excellent sealing capabilities and contain hints about major accumulations of petroleum and gas reservoirs. Therefore, determining the accurate location of salt domes within migrated seismic volumes is one of the key steps in the exploration projects. However, with the increasing size of acquired seismic volumes, manual interpretation of salt domes is becoming extremely time consuming and labor intensive.

In this chapter, we propose a dictionary-based classification approach for salt dome detection within migrated seismic volumes. The proposed workflow resorts to the seismic attributes derived from the gray level co-occurrence matrix (GLCM), Gabor filter, and higher order singular value decomposition (HOSVD) to effectively learn and detect the salt bodies. We use an information theoretic framework to rank the seismic attributes as per their salt dome classification performance. Based on this ranking, we select the top K attributes for dictionary training, testing, and classification. To improve the accuracy of the detected salt bodies and make the proposed workflow robust to different datasets, we introduce a refining step, which utilizes edge strength and energy values to detect the shape of the salt dome boundary within the classified patches. The optimal set of attributes and the refining step ensure that the proposed workflow yields good results for detecting salt-dome boundaries even in the presence of weak seismic reflections. We use the seismic data from the Netherlands offshore F3 block (North Sea) to demonstrate the effectiveness of the proposed workflow in detecting salt bodies. Using both subjective and objective evaluation metrics, we compare the results of the proposed workflow with existing gradient-, texture-, and patch-based classification methods. The proposed algorithm yields better results using reduced number of features as compared to the other texture-attributes-based salt dome detection methods. The main contributions of this chapter include:

- A patch based salt dome detection method using the dictionary-based classifier.
- An information theoretic-based framework to rank the features based on their relevance and significance.
- Utilization of ranked features in dictionary learning and classification.
- A boundary refining step, based on the edge strength and energy values and to overcome the drawbacks of existing patch-based salt dome detection methods.

5.1 The Proposed Salt Dome Detection Workflow

The proposed algorithm works by creating a dictionary from the available training data. The training slices are first partitioned into small patches of size $N \times N$. Next, we compute the GLCM, Gabor filter, and HOSVD based features for these patches. We use the GLCM contrast attribute, GLCM entropy attribute, GLCM energy attribute, Gabor filter attributes for $\theta = 0, \pi/4, \pi/2, 3\pi/2$, trace attribute across inline cross line and time, largest singular value attribute across inline cross line and time, and coherence attribute across inline cross line and time. The details of these attributes were discussed in ch. 3 and 4. These features are then

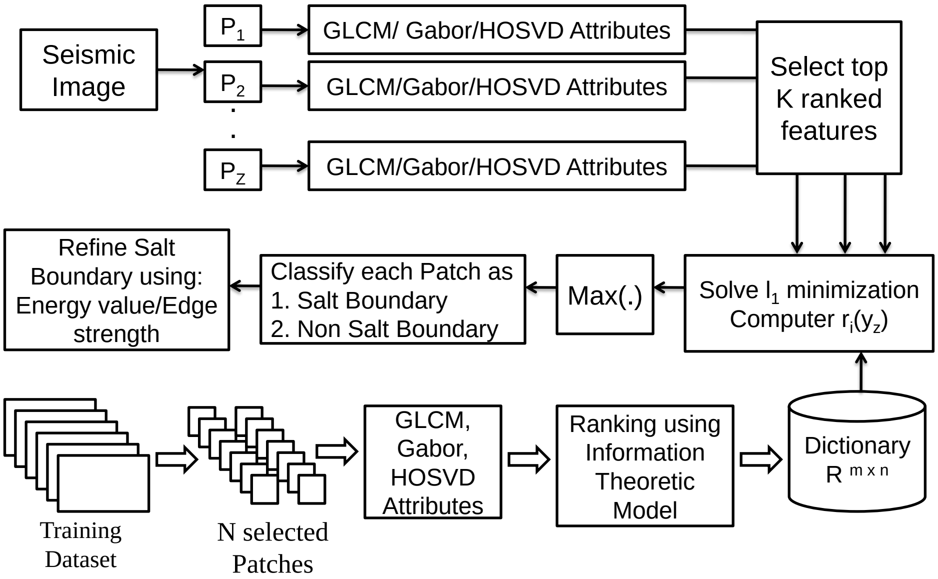

Figure 5.1: The proposed dictionary-based salt dome detection algorithm

ranked using three information theoretic-based models: (i) Mutual Information Feature Selection (MIFS) criterion, (ii) Minimum Redundancy Maximum Relevance (mRMR) criterion, and Joint Mutual Information (JMI) criterion. The top ranked features are selected and concatenated to form a dictionary. For a given test slice, the proposed scheme first partitions it into small non overlapping patches. By solving an ℓ_1 minimization problem, each patch is classified as either a salt boundary or a non-salt boundary patch. To get the accurate salt boundary from these classified patches, we use a combination of energy value and edge strength to detect the correct boundary points within each patch. We obtain the outline of salt boundary by combining all the boundary points. Fig. 5.1 shows the workflow for the proposed algorithm. We will now discuss each of the blocks from Fig. 5.1 in more details.

5.1.1 Feature Ranking using an Information Theoretic Model

The accuracy and complexity of a dictionary-based classifier depend on the relevance and number of features used for classification. To get the optimal set of features, we use an information theoretic-based model. We rank the features in order of their significance and select the K most important features that provide maximum accuracy. The value of K is chosen by experimental analysis. In this work, we use three information theoretic models, mRMR, MIFS, and JMI, for feature ranking. We discuss the results of three models and select the most important and relevant features for salt boundary detection.

The MIFS criterion [64] iteratively creates the feature set by selecting the feature with highest J_{mifs} score in every iteration.

$$J_{mifs} = I(X_k; Y) - \beta \sum_{X_j \in S} I(X_k; X_j), \tag{5.1}$$

where S is the set that includes currently selected features, Y is the class label, X_k is the k^{th} feature. $I(X;Y)$ is the mutual information between X and Y.

$$I(X;Y) = \sum_{x \in X} \sum_{y \in Y} p(x,y) log \frac{p(x,y)}{p(x)p(y)}, \tag{5.2}$$

where $p(x,y)$ is the joint probability mass function, $p(x)$ and $p(y)$ are marginal probabilities. The first term, $I(X_k;Y)$, in J_{mifs} maximizes the feature relevance. The second term is introduced to ensure low correlations with the features already selected in S. Iteratively, the features are ranked in the order best to worst. By selecting different values of β, we can have different feature selection criterion. Choosing $\beta = 0$ will result in selecting features independently, the criterion is also known as Mutual Information Maximization (MIM). For most of the feature selection applications, the optimal value of β is 1. For our experiments, we have also used $\beta = 1$. The problem with MIFS criterion is that as the set S grows, the second term with summation will give large value as compared to the first term. For large S, the first term will have no or very little contribution in feature ranking.

The mRMR criterion [65] is similar to MIFS. The β coefficient in mRMR is in inverse relation with the size of current feature selection set. This choice of β overcomes the limitation of MIFS and limits the second term even when S becomes large. The selection criteria for mRMR is given as:

$$J_{mRMR} = I(X_k; Y) - \frac{1}{|S|} \sum_{X_j \in S} I(X_k; X_j). \tag{5.3}$$

For very large set S, the value of β will be close to zero which means the selection of features will be carried independently as in case of MIM.

As we know, correlation does not always imply redundancy. The inclusion of correlated features can be useful provided correlation within classes is stronger than the overall correlation. The JMI feature selection criterion proposed in [66], [67] considers both the inter-class and intra-class correlation. JMI criterion selects the new feature only if it complements the existing features in set S. The selection criterion for JMI is given as:

$$J_{jmi} = \sum_{j \in S} I(X_k X_j; Y). \tag{5.4}$$

After some manipulations (see [68]), the above relation can be written as:

$$J_{jmi} = I(X_k; Y) - \frac{1}{|S|} \sum_{j \in S} I(X_k; X_j) - I(X_k X_j; Y). \tag{5.5}$$

Like mRMR, the JMI also selects the features independently as the size of feature set S grows. The difference here is the conditional term.

In Table 1, we show the ranking of features according to the three criterions. In Fig. 5.2(a), we show the histogram of top ranked feature. We can see that the distributions of salt boundary and non-salt boundary samples are almost separate and the overlapping region is very small. In Fig 5.2(b), we show the histogram of salt boundary and non-salt boundary samples for the lowest ranked feature, the two distributions overlap each other completely which illustrates that classification using this feature will give poor results.

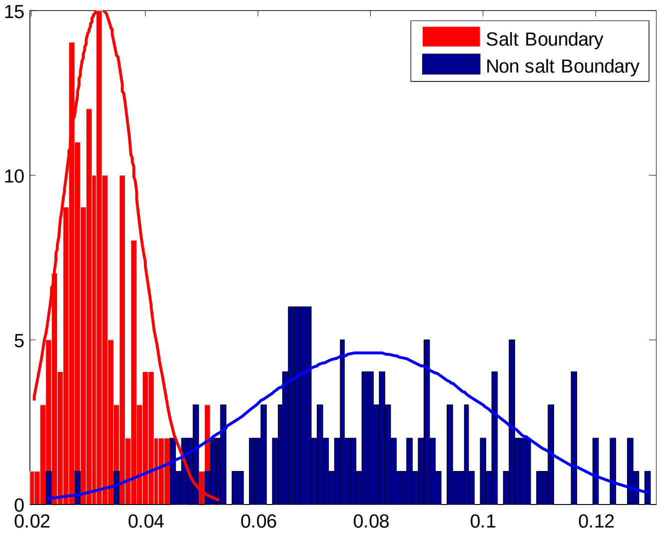

(a)

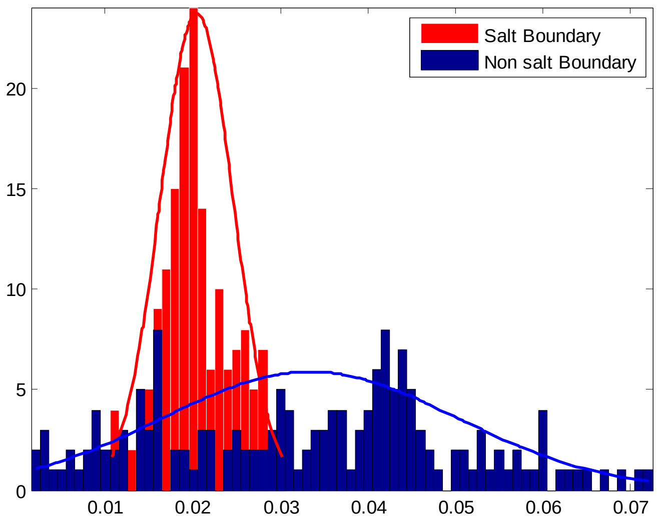

(b)

Figure 5.2: (a) Histogram of top ranked attribute (trace Attribute across crossline) (b) Histogram of lowest ranked attribute (coherence Attribute across time)

5.1.2 Classification using Dictionary-based Learning

Dictionary-based classifiers have the advantage of working with a minimum number of features and have shown excellent results in various texture classification

Table 5.1: Feature ranking using mRMR, MIFS, and JMI selection criterion

Attribute	**MIFS**	**mRMR**	**JMI**
GLCM Contrast	4	4	5
GLCM Entropy	11	11	12
GLCM Energy	5	5	9
Gabor Attribute ($\theta = 0$)	13	13	14
Gabor Attribute ($\theta = pi/4$)	3	3	3
Gabor Attribute ($\theta = pi/2$)	7	7	6
Gabor Attribute ($\theta = 3pi/4$)	10	10	8
Trace Attribute ($Trace_\sigma^{(1)}$)	2	2	2
Trace Attribute ($Trace_\sigma^{(2)}$)	1	1	1
Trace Attribute ($Trace_\sigma^{(3)}$)	9	9	10
Largest Singular Value $\sigma_l^{(1)}$	8	8	7
Largest Singular Value $\sigma_l^{(2)}$	6	6	4
Largest Singular Value $\sigma_l^{(3)}$	12	12	11
Coherence Attribute $C_\sigma^{(1)}$	15	15	15
Coherence Attribute $C_\sigma^{(2)}$	14	14	13
Coherence Attribute $C_\sigma^{(3)}$	16	16	16

problems such as fingerprint identification, tumor segmentation, breast cancer detection etc.

The fundamental principle of texture-based classification is to use the training features from n distinct textures covering different classes to correctly classify a given test sample. The n training feature vectors, each of length m, are stacked to construct a dictionary $\mathbf{D} = [\mathbf{v}_1, \mathbf{v}_2, ..., \mathbf{v}_n] \in \mathbb{R}^{m\times n}$. The columns of the dictionary $\mathbf{D}$ are then the features of n training textures.

For the salt dome detection, we consider two classes of textures: i) salt boundary texture, ii) non-salt boundary texture. A dictionary $\mathbf{D}$ is then represented as:

$$\mathbf{D} = [\mathbf{D}_1\, \mathbf{D}_2] = [\mathbf{v}_{1,1}, \mathbf{v}_{1,2}, \cdots, \mathbf{v}_{1,n_1} \mathbf{v}_{2,1}, \cdots, \mathbf{v}_{2,n_2}] \in \mathbb{R}^{m\times n}, \tag{5.6}$$

where n_1 and n_2 are the number of training samples of salt boundary and non-salt boundary patches. $\mathbf{D}_1 = [\mathbf{v}_{1,1}, \mathbf{v}_{1,2}, ..., \mathbf{v}_{1,n_1}]$
$\in \mathbb{R}^{m \times n_1}$ is the matrix containing feature samples from the salt boundary class, and $\mathbf{D}_2 = [\mathbf{v}_{2,1}, \mathbf{v}_{2,2}, ..., \mathbf{v}_{2,n_2}] \in \mathbb{R}^{m \times n_2}$ is the matrix containing feature samples from the non-salt boundary class.

A test sample $\mathbf{y} \in \mathbb{R}^{m \times 1}$ belonging to the salt boundary class will lie in the linear span of $\mathbf{D}_1$, given that $\mathbf{D}_1$ has enough training samples, and can be projected as:

$$\mathbf{y} = c_{1,1}\mathbf{v}_{1,1} + c_{1,2}\mathbf{v}_{1,2} + ... + c_{1,n_1}\mathbf{v}_{1,n_1}, \tag{5.7}$$

where $c_{1,1}, c_{1,2}, ..., c_{1,n_1}$ are scalar values. For the complete dictionary D, which contains feature vectors from both classes, the linear representation of $\mathbf{y}$ can be rewritten as:

$$\mathbf{y} = c_{1,1}\mathbf{v}_{1,1} + ... + c_{1,n_1}\mathbf{v}_{1,n_1} + c_{2,1}\mathbf{v}_{2,1} + ... + c_{2,n_2}\mathbf{v}_{2,n_2}, \tag{5.8}$$

where $c_{2,1}, c_{2,2}, ..., c_{2,n_2}$ have zero values. Therefore

$$\mathbf{y} = \mathbf{D}\mathbf{x}, \tag{5.9}$$

where $\mathbf{x} = [c_{1,1}, c_{1,2}, ..., c_{1,n_1}, 0, 0, ..., 0]$ is a vector whose only non-zero entries are the ones that are associated with the salt boundary class.

Give a test sample, $\mathbf{y}$, from a salt boundary class and the dictionary $\mathbf{D}$, we first compute $\mathbf{x}$. The system $\mathbf{y} = \mathbf{D}\mathbf{x}$ is underdetermined and $\mathbf{x}$ is sparse, therefore, we can solve the following ℓ_1 minimization problem.

$$\hat{\mathbf{x}} = argmin\,\|\mathbf{x}\|_1 \quad \text{subject to} \quad \mathbf{D}\mathbf{x} = \mathbf{y}. \tag{5.10}$$

Solving ℓ_1 norm minimization problem is computationally intensive. The cost of the solution using linear programming is of order $O(n^3)$ which is extremely slow for seismic data of very large size. Alternatively, other approximation methods such as orthogonal matching pursuit algorithm [69], and Homotopy [70] can be used.

For an exact match, the non-zero entries in $\hat{\mathbf{x}}$ will be associated with the columns of D corresponding to the salt boundary patches only. For all the other columns, the entries will be zero. However, this is not true due to limited number of training samples. Therefore, to classify y, we can sum the entries of $\hat{\mathbf{x}}$ associated with each class and select the class which gives the maximum value.

$$r_i(y) = \sum_{k_i} \alpha(\hat{x}_i), \tag{5.11}$$

$$\text{class}(y) = \text{argmax}_i r_i(y), \tag{5.12}$$

where $\alpha(\hat{x}_i)$ contains the entries of the estimated vector $\hat{\mathbf{x}}$ associated with class i. For our case, we will select the maximum from $r_1(y)$ ad $r_2(y)$ where $r_1(y)$ is the sum of the elements of $\hat{\mathbf{x}}$ associated with salt boundary and $r_2(y)$ is the sum of elements of $\hat{\mathbf{x}}$ associated with non-salt boundary. Algorithm 1 below describes the construction of the dictionary.

Algorithm 1: Dictionary Construction

1. From the available seismic dataset, select n patches of size $L \times L$ for training.
2. Compute K GLCM, Gabor, and HOSVD based features for each training patch.
3. Select m features such that $m < K$.
4. Stack the m feature samples for training patches to create a dictionary $\mathbf{D} \in \mathbb{R}^{m \times n}$.

Based on the above dictionary, we outline our proposed dictionary classification algorithm for salt dome detection.

Algorithm 2: Dictionary based classification

1. Create a dictionary from the given training data for two classes: i) class 1: salt boundary, ii) non-salt boundary (Use Algorithm 1) .
2. Divide the input test inline into $L \times L$ non overlapping patches.
3. For each patch, compute and select m GLCM, Gabor, and HOSVD based features such that $\mathbf{y}_i \in \mathbb{R}^m$.
4. For each patch, solve the ℓ_1 minimization problem
   $\hat{\mathbf{x}} = argmin \left\| x \right\|_1 \quad subject\ to \quad \mathbf{D}\mathbf{x} = \mathbf{y}$.
5. Compute $r_1(y) = \sum_{k_1} \alpha(\hat{x}_1)$ and $r_2(y) = \sum_{k_2} \alpha(\hat{x}_2)$.

6. Identify the class of all the patches using

   $\text{class}(y) = \text{argmax}\{r_1(y), r_2(y)\}$.

5.1.3 Accurate Salt Boundary Detection using Edge Strength and Largest Eigenvalue

Dictionary-based classifier, discussed in the previous section, classify the boundary patches with good accuracy. The size of each patch is $N \times N$ where $N \geq 3$. To estimate the boundary from the classified patches, we need a further refinement step. In [10], the boundary is extracted from the classified patches by just considering the lower part (row) of each patch. The results, however, were not refined. Another approach is to take the center row of each patch and estimate the salt boundary. A third option is to consider the upper part of each patch as the boundary of salt dome. All of these three mentioned approaches may work for some slices, but may not produce the desired results for other slices. In this work, we propose a refining step, based on the energy and the edge strength, to estimate the salt boundary accurately within a patch. For the classified patches, we compute the energy using the eigenvalue attribute as discussed in [43] and the edge strength using the Sobel operator. We select the points that give the maximum energy and edge values for detecting the salt boundary.

Eigenvalue attribute is computed using the covariance matrix obtained from the gradients in x, y, and z directions. The value of this attribute will be high for the salt boundary and low for the surrounding areas. Therefore, this attribute can assist in detecting the salt boundary accurately within a patch. The covariance matrix is computed as:

$$C = \begin{bmatrix} C_{xx} & C_{xy} & C_{xz} \\ C_{yx} & C_{yy} & C_{yz} \\ C_{zx} & C_{zy} & C_{zz} \end{bmatrix}, \tag{5.13}$$

$$C_{ab} = \frac{1}{N^3} \sum_{x,y,z} \left(G_a(x, y, z) - \mu_a \right) \left(G_b(x, y, z - \mu_b) \right), \tag{5.14}$$

where N is the window size ($N = 9$ for 3×3 windows), G_a and G_b are the gradients in directions a and b, and μ_a and μ_b are the means in a and b directions, respectively. From the covariance matrix, we get the eigenvalue attribute:

$$\lambda_1 = max(\lambda_i), \tag{5.15}$$

where $\lambda_i' s$ are the eigenvalues of the covariance matrix. The largest eigenvalue, λ_1, gives the energy information for each pixel. We use this value along with the edge strength to get the desired salt boundary.

For the edge strength, we use the Sobel edge detector which computes spatial gradients of an image and enhances regions of high frequency that represent edges. The convolution operators for the Sobel edge detector in the x direction and y

directions are given as:

$$G_x = \begin{bmatrix} -1 & 0 & 1 \\ -2 & 0 & 2 \\ -1 & 0 & 1 \end{bmatrix}, \tag{5.16}$$

$$G_y = \begin{bmatrix} -1 & -2 & -1 \\ 0 & 0 & 0 \\ 1 & 2 & 1 \end{bmatrix}. \tag{5.17}$$

Although the Sobel operator gives better results as compared to other edge detectors, considering the gradient map only in the x and y directions may not give accurate results along the diagonal directions of salt-dome boundaries. To improve the performance of the Sobel edge detector, we include the diagonal directions (45^o and 135^o) along with x and y directions. The convolution operators for the Sobel edge detector in the diagonal directions are given as:

$$G_{45} = \begin{bmatrix} -2 & -1 & 0 \\ -1 & 0 & 1 \\ 0 & 1 & 2 \end{bmatrix}, \tag{5.18}$$

$$G_{135} = \begin{bmatrix} 0 & -1 & -2 \\ 1 & 0 & -1 \\ 2 & 1 & 0 \end{bmatrix}. \tag{5.19}$$

The magnitude of the total gradient is now computed as:

$$G = \sqrt{{G_x}^2 + {G_y}^2 + {G_{135}}^2 + {G_{45}}^2}. \tag{5.20}$$

The energy value and the edge strength value are accumulated and the points with maximum values in the classified patches are selected as the boundary points.

The refining step introduced here has two advantages: First, the boundary is estimated accurately within each patch and we get refined results as compared to the other patch-based methods. Secondly, we can choose different patch sizes (N). The more accurate features can be estimated using a large patch size. Patch-based methods [10], without the refining step, are sensitive to the patch size as the shape of the detected salt boundary depends largely on the size and location of patches. More accurate and refined boundary is obtained for the small patches. However, the features estimated from the small patches may not be very accurate. In our work, we use a large patch-size to estimate good features. For the final salt-dome boundary, we use the refining step based on the energy value and the edge strength.

5.2 EXPERIMENTAL RESULTS

We tested our salt dome detection method on the Netherlands offshore F3 block acquired in the North Sea for oil and gas exploration. The survey covers an area of 24 x 16 km^2. The Inline range is from 100 to 750, the cross line range is 300 to 1250, the time direction ranges from 0 to 1848 ms sampled at every 4 ms, and the bin size is 25 m in inline and crossline directions. The data set contains important geological features such as salt dome, faults, bright spots, etc.

We selected 100 inline sections each of size 130 $\times$ 300. The dictionary was created using 400 training patches of size $N \times N$.The training patches were selected equally from the salt boundary and non-salt boundary classes. For each patch, the proposed algorithm computes GLCM attributes, Gabor filter attributes, and HOSVD based attributes.

5.2.1 Feature Selection using MIFS, mRMR, JMI

We rank the attributes, computed for each patch, using the MIFS, the mRMR, and the JMI criterion and select the top K features. The value of K is chosen empirically. From experiments, we found that the top 7 ranked attributes provide best results for salt dome detection. In Fig. 5.3, we show the classification accuracy computed for different values of K. We observe that the maximum accuracy is achieved for $K = 7$. As the value of K increases beyond 7, we observe a dip in the accuracy value. This is because the low ranked attributes do not provide any new information, rather they increase the confusion (the curse of dimensionality) which results in low accuracy value. For the classification accuracy, we have used the F-measure value, which is most commonly used evaluation metric in the image segmentation problems (see eq. 31-33).

In Table 2, we show the top 7 ranked attributes using mRMR, MIFS, and JMI features selection criteria. We observe that the top 7 ranked features using mRMR and MIFS are same. This is because the size of set S is not large. Therefore, the second term in MIFS does not limit the effect of the first term. We show in Fig. 5.4 the classification accuracy of salt boundary detected for the inlines # 350 to 359 using the proposed method with feature ranking based on mRMR, MIFS, and JMI. We select the top 7 attributes ranked by mRMR, MIFS, and JMI. The proposed algorithm using the JMI selection criteria gives an average accuracy of 96.5% which is 0.4% higher than the proposed method using mRMR or MIFS criterion. Therefore, for further experiments, we have used the top 7 attributes ranked by the JMI criterion.

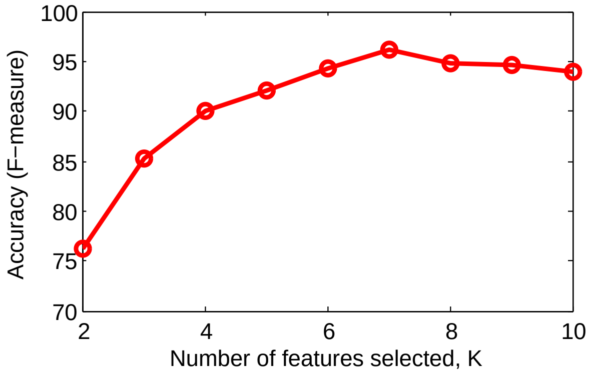

Figure 5.3: Classification accuracy K=2,3,...,10

Table 5.2: Top 6 features ranked using mRMR, MIFS, and JMI criterion

MIFS, mRMR	**JMI**
Trace Attribute ($Trace_{\sigma}^{(2)}$)	Trace Attribute ($Trace_{\sigma}^{(2)}$)
Trace Attribute ($Trace_{\sigma}^{(1)}$)	Trace Attribute ($Trace_{\sigma}^{(1)}$)
Gabor Attribute ($\theta = pi/4$)	Gabor Attribute ($\theta = pi/4$)
GLCM Contrast	Largest Singular Value $\sigma_l^{(2)}$
GLCM Energy	GLCM Contrast
Largest Singular Value $\sigma_l^{(2)}$	Gabor Attribute ($\theta = pi/2$)
Gabor Attribute ($\theta = pi/2$)	Largest Singular Value $\sigma_l^{(1)}$

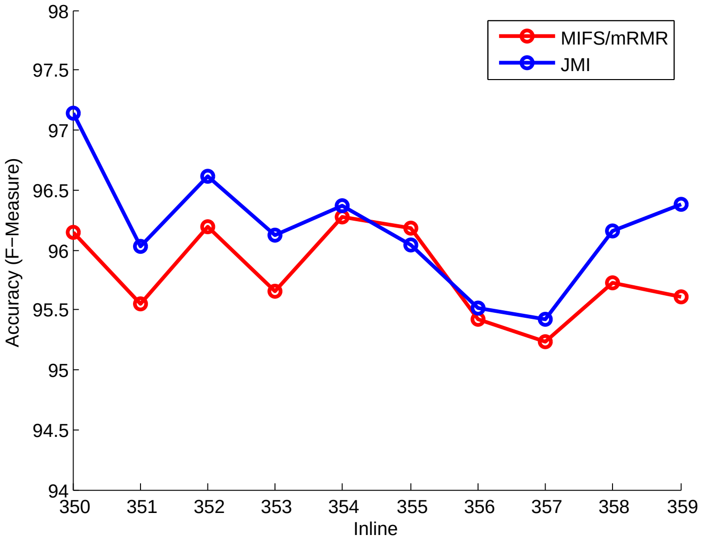

Figure 5.4: Classification accuracy using MIFS/mRMR and JMI for K=7

5.2.2 Optimal Patch Size for Training and Testing

The selection of patch size ($N \times N$) plays an important role in extracting good features for salt dome detection. The accuracy of the features extracted from the GLCM, and those computed from the Gabor filter depends on the window (patch) size. The value of N is also important in estimating the final boundary of salt dome. The introduction of refining step based on the energy value and edge strength gives us the choice to choose a large value of N. In Fig. 5.5, we show the classification accuracy computed for different patch sizes. We see that the maximum accuracy is achieved for $N = 7$. This is because for $N < 7$, the features extracted from the patches are not very accurate as the size of patch is small. For $N > 7$, the accuracy decreases because the features extracted from large patches does not include the local information.

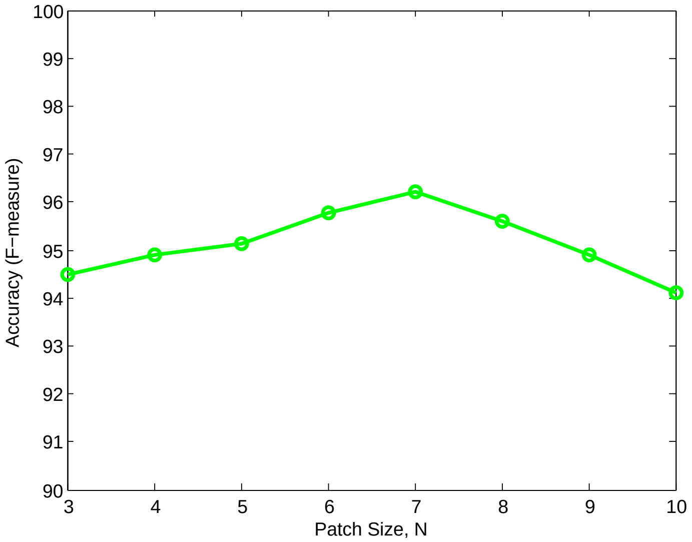

Figure 5.5: Classification accuracy N=3,4,...,10

5.2.3 Comparison with State-of-the-art

We consider inline # 354 as a test case to analyze and compare the performance of the proposed algorithm. The test inline is partitioned into non-overlapping patches of size 7 x 7. Figure 5.6 (b) shows the classification result for the salt boundary patches using the dictionary-based classifier. We see here that most of the boundary patches are correctly classified. Figure 5.6 (c) shows the ground truth and the salt boundary detected for the inline # 354 using the proposed method. The green boundary here is the ground truth, and red is the boundary produced by the proposed method. We see that the proposed method is able to outline the boundary with good accuracy.

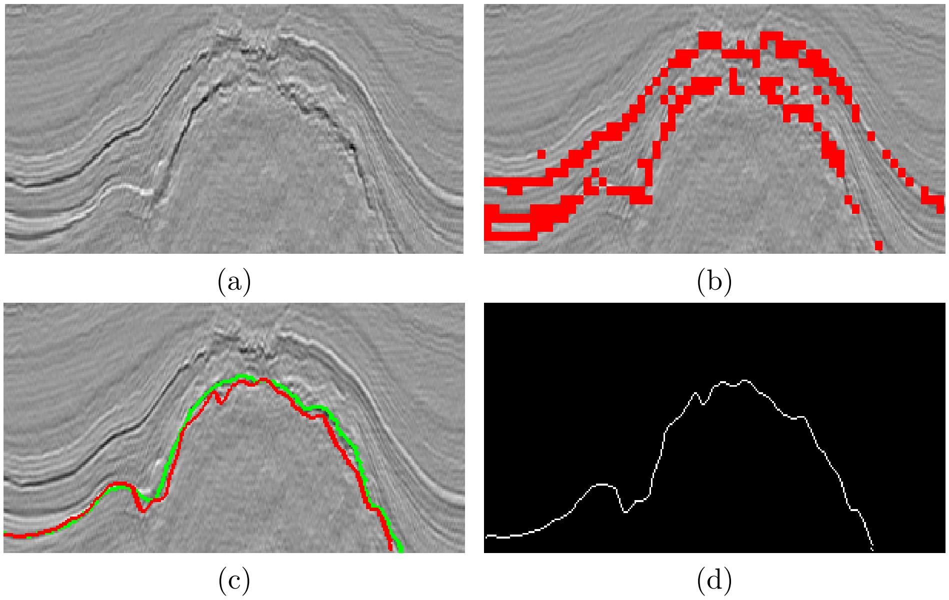
(a) (b) (c) (d)

Figure 5.6: (a) Inline # 354, (b) Identified salt boundary patches, (c) Ground truth (Green), Detected salt boundary (Red), (d) Outline of detected boundary

Two more examples are provided in Fig. 5.7 for inlines # 360 and 389 using the proposed method. The salt boundaries produced by the proposed method are very close to the ground truth. The proposed algorithm gives excellent results even for the inline # 389 which has an uneven salt boundary.

We compared the performance of our method with the edge detection based method [3], the texture attributes based method [8], the hybrid edge and texture based method [9], the dictionary based classification method [10], and the 3D gradient of texture (GoT) method [11]. Sobel edge detector is used for Aqrawi method. The texture based method [8] uses the attributes computed from the GLCM, the Gabor filter, and the eigen structure. Fig. 5.8 shows the classification results using the proposed method, edge detection based method, texture attributes method, hybrid method, patch-based method, and 3D GoT method.

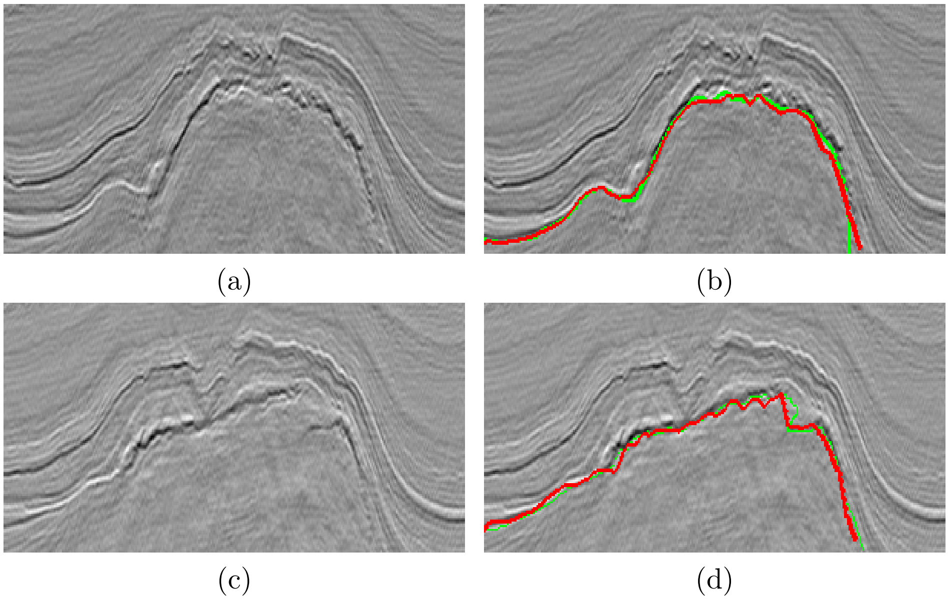

Figure 5.7: 1st Row: Salt boundary detected for the inline # 360, 2nd Row: Salt boundary detected for the inline # 389.

The green boundary here is the ground truth, red is the boundary produced by the proposed method, blue is the boundary produced by the edge-based method [3], cyan is the boundary produced by the texture-based method [8], purple is the boundary produced by the hybrid edge-texture method [9], yellow is the boundary produced by the dictionary-based method [10], and black is the boundary produced by the GoT method [11] method. We can see that the boundary produced by our algorithm is very close to the ground truth. The boundary produced by the texture-based deviates from the ground truth at various points as this method is sensitive to the features used for classification. The edge-based method is not able to detect the points at the end of salt dome where the boundary is not represented by strong edge. The hybrid edge-texture method, which combines edge and texture attributes, is able to trace the boundary accurately except for the diagonals and the end points of salt dome. The dictionary-based method considers the lower portion of classified patches as salt boundary, therefore this method is not able to produce smooth results as can be seen in Fig. 5.8. The GoT method, which measures the texture dissimilarity between two neighboring cubes, misses some points at the start and end of salt dome and also produces some over-segmented regions. The results produced by the proposed method are much better in terms of accuracy than the other salt dome detection methods. Fig. 5.9 shows the boundary outline produced using the proposed method, the edge-based method, the texture-based method, the hybrid edge-texture method, the dictionary-based method, and the GoT method.

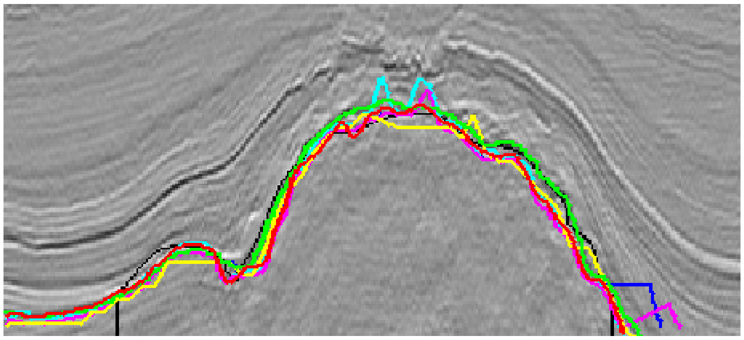

Figure 5.8: Ground truth (Green); Salt boundary detected for inline # 354 using the proposed dictionary-based method (Red), the edge-based method [3] (Blue), the texture-based method [8] (Cyan), the hybrid edge-texture method [9] (Purple), the dictionary-based method [10] (Yellow), and the GoT method[11] (Black)

In Table 3, we show the average classification accuracy (normalized Frechét distance) of salt boundaries, computed for inlines # 350 to 399, using the proposed method, the edge-based method [3], the texture-based method [8], the hybrid edge-texture method [9], the dictionary-based method [10], and the GoT method [11]. The proposed method gives an average accuracy of 90.57% which is almost 4% higher than the edge method, 3% higher than the texture method, 2% higher

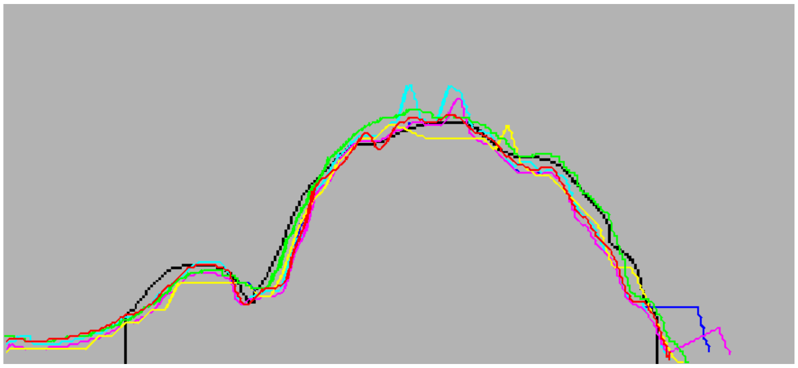

Figure 5.9: Ground truth (Green); Salt boundary outline produced for inline # 354 using the proposed dictionary-based method (Red), the edge-based method [3] (Blue), the texture-based method [8] (Cyan), the hybrid edge-texture method [9] (Purple), the dictionary-based method [10] (Yellow), and the GoT method[11] (Black)

Table 5.3: Classification Accuracy of the proposed Dictionary-based method and other methods

Salt dome detection method	**Average accuracy**
Proposed method	90.57 %
Edge-based method [3]	86.74 %
Texture-based method [8]	87.78 %
Hybrid edge-texture method [9]	89.61 %
Dictionary-based method [10]	88.83 %
GoT method [11]	88.48 %

than the dictionary and GoT method, and 1% higher than the hybrid edge-texture method.

Precision, Recall, and F-measure are used commonly as objective evaluation metrics in image segmentation. To calculate these metrics, we compute the True Positive (TP), the False Positive (FP), the True Negative (TN), and the False Negative (FN) using the ground truth and the detected salt region.

- **TP:** Salt dome points classified correctly
- **TN:** Non-salt points classified correctly

- **FP:** Non-salt points classified as salt points
- **FN:** Salt dome points classified as non-salt points

Precision, recall, and F-measure are computed using:

$$Precision = \frac{TP}{TP + FP}, \tag{5.21}$$

$$Recall = \frac{TP}{TP + FN}, \tag{5.22}$$

$$F - Measure = 2 \times \frac{Precision \times Recall}{Precision + Recall}. \tag{5.23}$$

In Fig. 5.10, we show the ground truth of the salt dome and the salt regions detected using the proposed method, the edge-based method [3], the texture-based method [8], the hybrid edge-texture method [9], the dictionary-based emthod [10], and the GoT method [11] for inline # 354. In Fig. 5.11, 5.12, and 5.13, we show and compare the precision, recall, and F-measure values computed for inlines # 350 to 359 using the proposed method and the other methods discussed above. Precision gives the percentage of correctly classified salt points out of total classified points. We see that the proposed method gives excellent precision values for all inlines followed closely by the [10] method. The edge and GoT methods give consistent precision values for different inlines, the values however are less than those computed for the proposed and dictionary [10] method. The texture

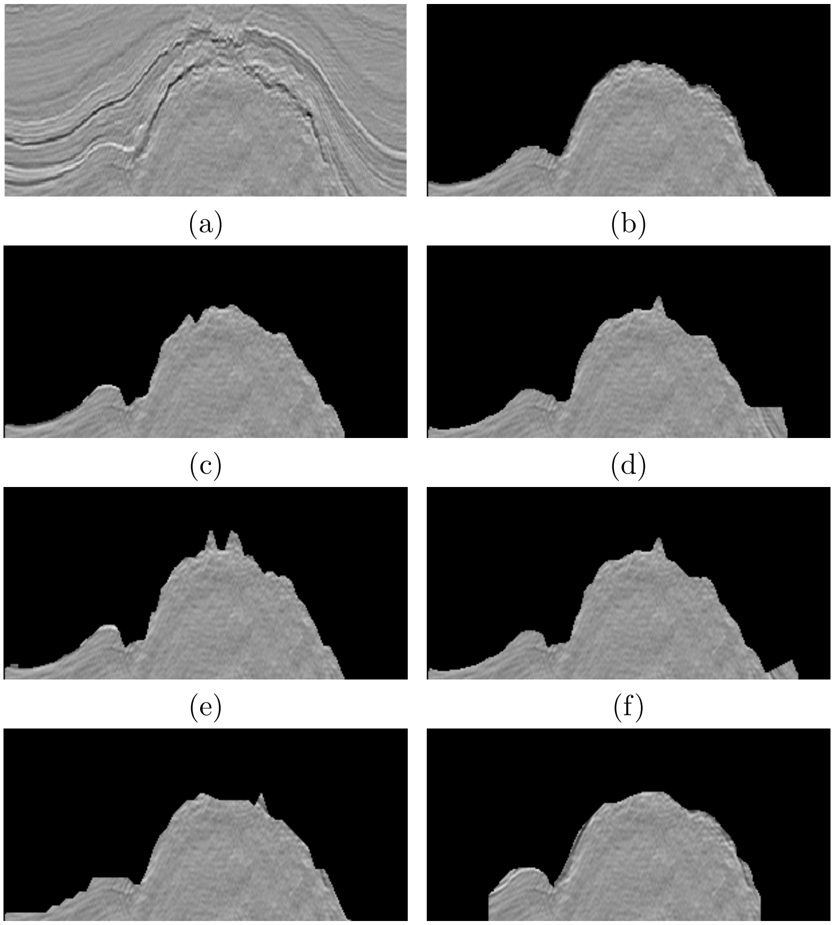
(a) (b) (c) (d) (e) (f) (g) (h)

Figure 5.10: (a) Inline # 354, (b) Ground Truth, Detected salt dome: (c) the proposed dictionary-based method, (d) the edge-based method [3], (e) the texture-based method [8], (f) the hybrid edge-texture method [9], (g) the dictionary-based method [10], (h) the GoT method [11]

.

method produce over-segmented results, as can be seen in Fig. 5.10. Therefore, the precision values are not consistent and varies significantly for different inlines. The hybrid edge-texture method, which combines the edge and texture attributes, gives good precision values with some inconsistency. This inconsistency is due to the over-segmented salt region produced by the texture attributes based method.

For the second evaluation metric i.e. Recall, the proposed method gives highest values for all inlines followed by the texture and hybrid edge-texture methods. The dictionary [10] method gives consistent but lowest recall values among all the methods. This is because the dictionary [10] method considers bottom pixels of each classified patch as salt boundary, and therefore, the detected shape is not very accurate. The recall values, calculated for the edge and hybrid edge-texture method, shows inconsistency and changes significantly for different inlines.The GoT method gives consistent but low recall values.

The third metric, F-measure, is used in image segmentation to find the accuracy of segmented regions. We have also used F-measure to compute the classification accuracy of salt dome detection methods. From Fig. 5.13, we see that the proposed algorithm gives highest F-measure values followed by the hybrid edge-texture method. The dictionary [10] and GoT methods give consistent but low F-measure values as compared to the proposed method. The edge and texture methods give inconsistent F-measure values for different inlines.

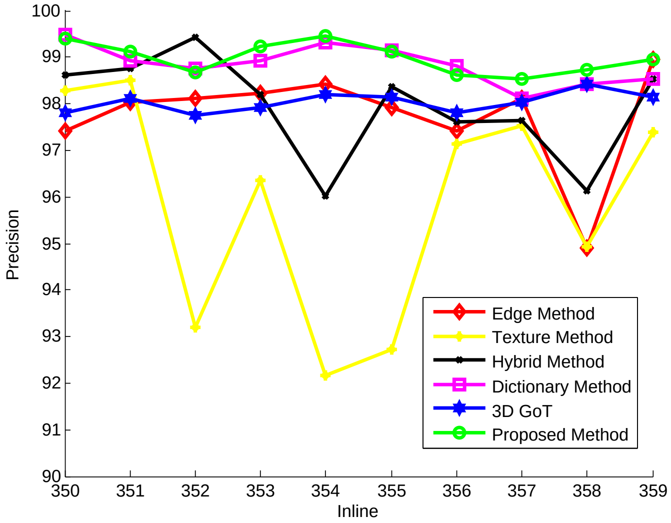

Figure 5.11: Precision values for the proposed dictionary-based method and other methods

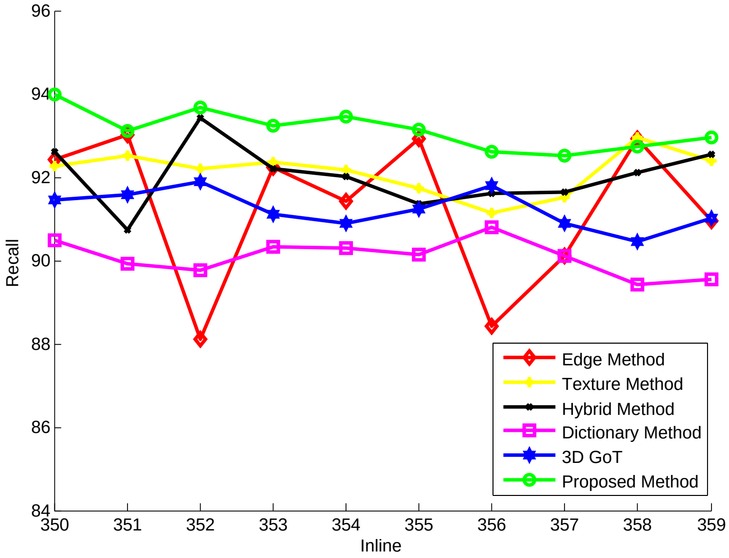

Figure 5.12: Recall values for the proposed dictionary-based method and other methods

Table 5.4: Precision, Recall, and F-Measure of the proposed Dictionary-based method and other methods

Salt dome detection method	**Prec**	**Recall**	**F-M**
Proposed method	98.97	94.24	96.55
Edge-based method [3]	97.75	91.25	94.37
Texture-based method [8]	95.82	92.12	93.92
Hybrid edge-texture method [9]	97.93	92.63	95.21
Dictionary-based method [10]	98.84	90.08	94.26
GoT method [11]	97.81	91.44	94.72

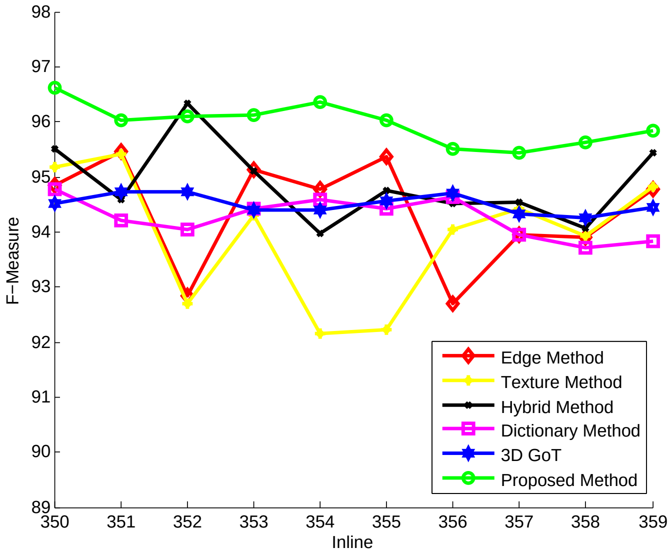

Figure 5.13: F-measure values for the proposed dictionary-based method and other methods

In Table 4, we show the average precision (Prec), recall, and F-measure (F-M) values computed for inlines # 350 to 399. The average F-measure value obtained for the proposed method is almost 2.6% higher than the texture-based method [8], approximately 2% higher than the edge-based [3], dictionary-based [10], and GoT [11] methods, and 1.5% higher than the hybrid edge-texture [9] method. The results show the improved performance obtained using the proposed algorithm while keeping the algorithm complexity to the minimum.

5.2.4 Accuracy and Complexity Comparison of the Proposed Dictionary-based Classifier

The proposed dictionary-based classifier detects salt dome with good accuracy. We compare the performance of the proposed dictionary-based classifier with the traditional Bayesian classifier discussed in [43]. We use the same set of attributes for both the classifiers. Figure 5.14 shows the classification accuracy for inlines # 101 - 150 to using the dictionary-based classifier and the Bayesian classifier. The dictionary-based classifier gives an average accuracy of 96.5% which is 3.6% higher than the Bayesian classifier. However, the computational cost of the dictionary-based classifier is higher than the Bayesian classifier.

The proposed dictionary-based classifier solves the ℓ_1 minimization problem to classify each patch. The solution to ℓ_1 minimization is computationally expensive. General LP solvers are slow and therefore not suitable for our application. In this work, we have used the Homotopy based solver [70] for ℓ_1 minimization problem. The accuracy of the Homotopy-based solver is comparable to the general Linear Programming (LP) solvers, whereas the computational cost is significantly less. In Table 5, we show the computational complexity of the proposed dictionary-based classifier method using the Homotopy method and the general LP solvers for five inlines. The dictionary-based classifier using the Homotopy method is three times computationally more efficient than the general LP solvers based method.

Table 5.5: Time Comparison: Homotopy vs general LP Solver

Inline #	**Homotopy**	**General LP Solver**
350	28.3 sec	74.24 sec
351	31.75 sec	80.28 sec
352	29.52 sec	77.52 sec
353	30.93 sec	79.62 sec
354	28.84 sec	74.87 sec

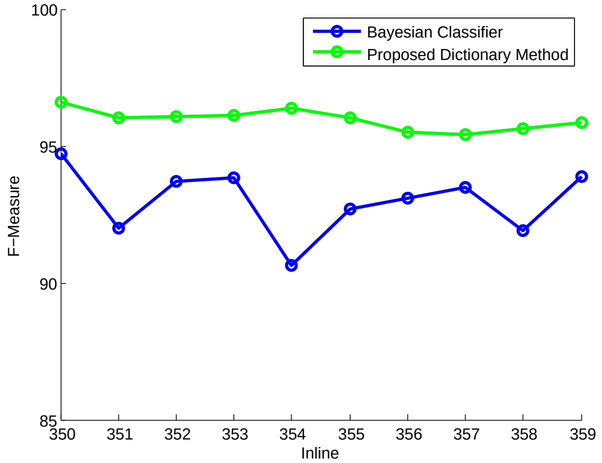

Figure 5.14: Dictionary-based classifier vs Bayes classifier (F-measure result)

5.2.5 Classification Accuracy with and without the Proposed Refining Step

As discussed in the previous section, we use a refining step based on energy value and edge strength to estimate the boundary accurately within the classified patch. Without the proposed refining step, the boundary of salt dome can be estimated by considering the bottom row pixels, middle row pixels or the top row pixels of each patch as the boundary pixels. We compare the performance of the proposed refining step with the other three approaches in Table 6. We see that the refining step enhances the accuracy of the proposed algorithm. The dictionary-based method, using the proposed refining step, gives an average F-measure value

Table 5.6: Accuracy Comparison: Dictionary based Classifier with and without refining

Salt Dome Detection Method	**F-measure**
Proposed method (with refining)	96.55
Dictionary Method (Bottom pixels, w/o refining)	94.26
Dictionary Method (Middle pixels, w/o refining)	92.51
Dictionary Method (Top pixels, w/o refining)	91.79

of 96.55% which is 2.5 % higher than the dictionary-based method considering bottom pixels of patches as the boundary. The other two approaches gives even lower F-measure values. The proposed refining step demonstrates a considerable enhancement as compared to no refining.

In this chapter, we introduced a new approach for salt dome detection using a dictionary-based classification framework. The features used with such a framework consist of an optimal set obtained from the GLCM, the Gabor filters, and Higher Order SVD, using an information theoretic feature ranking approach. We tested three popular feature ranking techniques, namely, the MIFS, mRMR, and JMI models. The JMI based information theoretic model was shown to provide the best ranking methodology suitable for salt dome detection. We also introduced a new boundary refining step for patch-based classification methods. This step was implemented using the energy values and the edge map computed for the classified patches. By combining the energy values and the edge map based refining step, together with the dictionary-based classification stage, we ensure that the proposed algorithm achieves excellent detection accuracy even when the salt boundary is represented by very weak reflectors.

CHAPTER 6

SALT DOME DETECTION AND TRACKING IN SEISMIC SURVEYS USING A HIDDEN MARKOV MODEL

A hidden markov model (HMM) is a stochastic process with an underlying process that is hidden, but observed through a sequence of symbols. Hidden markov models provide a simple and effective framework for modeling time varying sequences. 3D seismic data can be considered as a sequence of 2D slices. We introduce a HMM based approach to detect and track the salt boundaries in seismic volumes. In addition to applying salt dome detection scheme on 2D slices, we also propose an approach for tracking boundaries across slices taking into account continuity in the medium. The proposed algorithm combines the HMM with the Higher

Order Singular Value Decomposition (HOSVD) based features (discussed in Ch. 04) to accurately delineate the salt boundaries in seismic data. The optimal parameters for the HMM are estimated using the Expectation-Maximization (EM) algorithm. By using the HOSVD based features, we ensure that the proposed algorithm overcomes the limitations of existing texture attributes based methods that are heavily dependent upon the relevance of attributes and the size of window used for extracting these attributes.

6.1 The Proposed Salt Dome Detection Algorithm

The proposed algorithm works by extracting sequences of salt boundary and non-salt boundary pixels from the available training data, and computing the HOSVD-based features for the extracted sequences. The extracted features from the training set are then used with the EM algorithm to estimate the optimal parameters for the HMM. For a given test data, the algorithm first divides the input slice into sequences and then computes the HOSVD-based features for all the pixels in each sequence. Hidden states (salt or non-salt boundary) are then estimated for all pixels using the Viterbi algorithm. We use the estimated hidden states to delineate the salt boundaries. In Figure 6.1, we show the workflow of our proposed detection model. We will now discuss in more detail the proposed HMM used for training and testing.

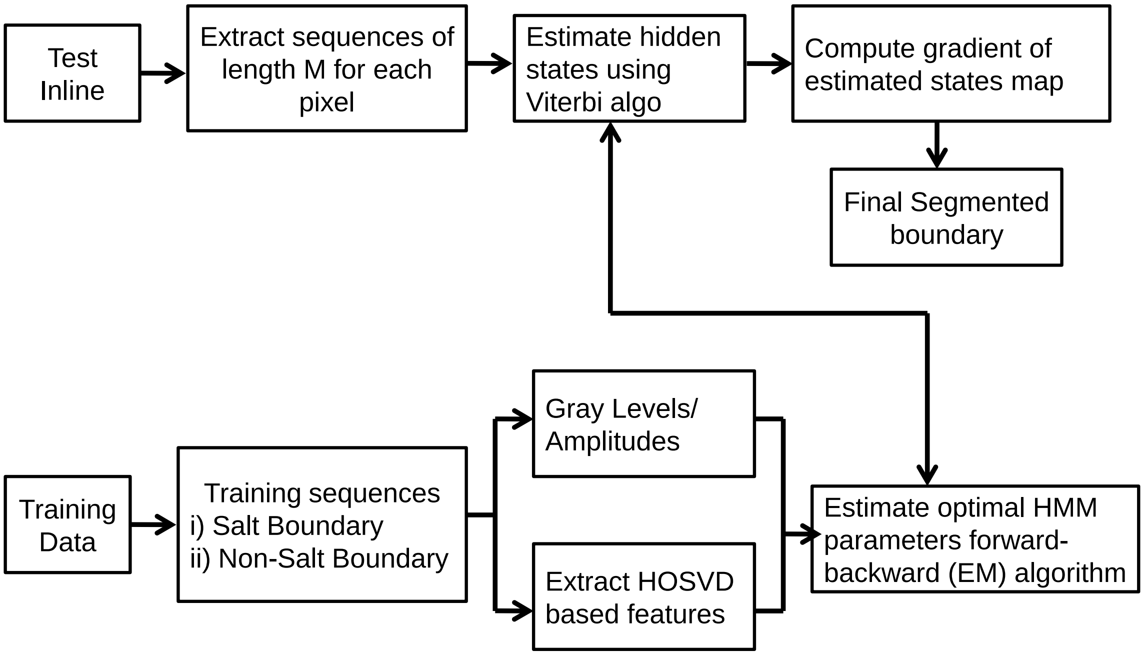

Figure 6.1: Workflow for salt dome detection using HMM

6.1.1 HMM Modeling and EM Parameter Estimation

The underground texture change following a specific direction is modeled as a Markov process. Let x_t denote the texture at the t-th pixel, which is assumed to have two possible discrete values: $x_t \in S = \{1, 2\}$. Value "1" refers to that the texture is non-salt, or in other words, the t-th pixel is not located in a salt dome. On the other hand, value "2" refers to that the t-th pixel is located in a salt dome. It is assumed that the underlying Markov chain defined by $P(x_t|x_{t-1})$ is index-homogeneous. Therefore, the joint probability of the state can be represented as $\Gamma \in R^{2\times 2}$, where its entries are

$$a_{i,j} \quad = \quad P(x_t = j|x_{t-1} = i), \quad i, j = 1, 2. \tag{6.1}$$

The special case of index $t = 1$ is described by the initial state distribution, $\pi_i = p(x_1 = i)$. Furthermore, let y_t denote either continuous or discrete observation of x_t. The probability of a particular observation vector at a particular pixel t for state j is described by:

$$b_j(x_t) = p(y_t|x_t = j). \tag{6.2}$$

The complete collection of parameters for all observation distributions is represented by $B = \{b_j(\cdot)\}$. Estimating the HMM parameters $\theta = (A, B, \pi)$ from a set of observation $Y = \{y_1, \cdots, y_T\}$ by using the EM algorithm can be done in the following steps.

A. Initialization

Assigning an initial value to $\theta^0 = (\Gamma^0, B^0, \pi^0)$ based on the prior information about the parameters.

B. EM procedure, starting with k=0

1. **Forward procedure**

   Let $\alpha_i(t) = P(y_1, ..., y_t, x_t = i|\theta^k)$ denote the joint probability of the first t observations $y_1, y_2, ..., y_t$ and $x_t = i$ given parameters θ^k, which is calculated recursively as follows,

$$\alpha_i(1) = \pi_i b_i^k(y_1) \tag{6.3}$$

$$\alpha_j(t+1) = b_j^k(y_{t+1}) \sum_{i=1}^{2} \alpha_i(t) a_{ij}^k \tag{6.4}$$

2. **Backward procedure**

Let $\beta_i(t) = P(y_{t+1}, ..., y_T | x_t = i, \theta^k)$ denote the joint probability of the ending partial sequence $y_{t+1}, ..., y_T$ and $x_t = i$ given parameters θ^k. Similarly, $\beta_i(t)$ is calculated recursively as,

$$\begin{aligned} \beta_i(T) &= 1 && (6.5) \\ \beta_i(t) &= \sum_{j=1}^{2} \beta_j(t+1) a_{ij}^k b_j^k(y_{t+1}) && (6.6) \end{aligned}$$

3. **Update**

By applying Bayes' rule, the probability of $x_t = i$ given the observed sequence Y and the parameters θ^k is obtained as

$$\begin{aligned} \gamma_i(t) &= P(x_t = i | Y, \theta^k) && (6.7) \\ &= \frac{\alpha_i(t)\beta_i(t)}{\sum_{j=1}^{2} \alpha_j(t)\beta_j(t)}. && (6.8) \end{aligned}$$

The joint probability of $x_t = i$ and $x_{t+1} = j$ given the observations Y and parameters θ^k is obtained as

$$\begin{aligned} \xi_{ij}(t) &= P(x_t = i, x_{t+1} = j | Y, \theta^k) && (6.9) \\ &= \frac{\alpha_i(t) a_{ij} \beta_j(t+1) b_j(y_{t+1})}{\sum_{h=1}^{2} \alpha_h(T)}. && (6.10) \end{aligned}$$

Then, parameter $\theta^{k+1} = (\Gamma^{k+1}, B^{k+1}, \pi^{k+1})$ is updated as

$$\pi_i^{k+1} = \gamma_i(1) \tag{6.11}$$

$$a_{ij}^{k+1} = \frac{\sum_{t=1}^{T-1} \xi_{ij}(t)}{\sum_{t=1}^{T-1} \gamma_i(t)} \tag{6.12}$$

$$b_i^{k+1}(v_k) = \frac{\sum_{t=1}^{T} 1_{y_t=v_k}\gamma_i(t)}{\sum_{t=1}^{T} \gamma_i(t)}. \tag{6.13}$$

C. Convergence evaluation

If θ^{k+1} achieves the desired level of convergence, then the EM algorithm is terminated with $\theta^* = \theta^{k+1}$, else let $k = k + 1$ and go back to step **Forward procedure**.

6.2 The Proposed Salt Dome Tracking Method

For salt dome tracking, we propose a new HMM, the parameters of which are estimated such that the candidate points in the successive inlines have a higher probability of belonging to the salt boundary class. The contextual information is also incorporated to make the overall algorithm more robust and accurate. From the detected salt boundary in Inline # K, the candidate points are computed using a simple 5×5 kernel as shown in Fig. 6.2. The salt boundary is tracked in the next N inlines using these points. The algorithm again computes the candidate points using the Inline # $K + N$. Similarly, the process continues for the whole salt dome. In Fig.6.3, we show the workflow of our proposed salt dome tracking methodology.

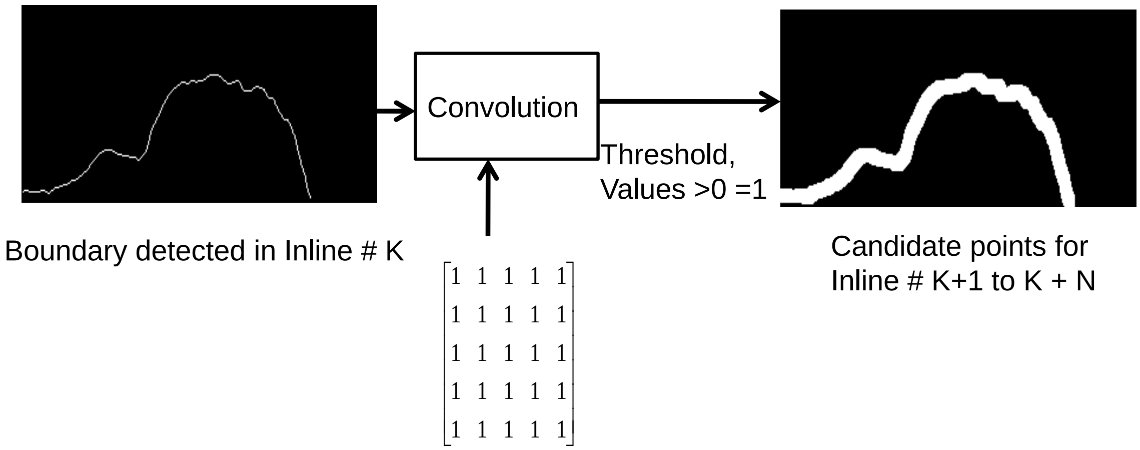

Figure 6.2: Candidate points for tracking

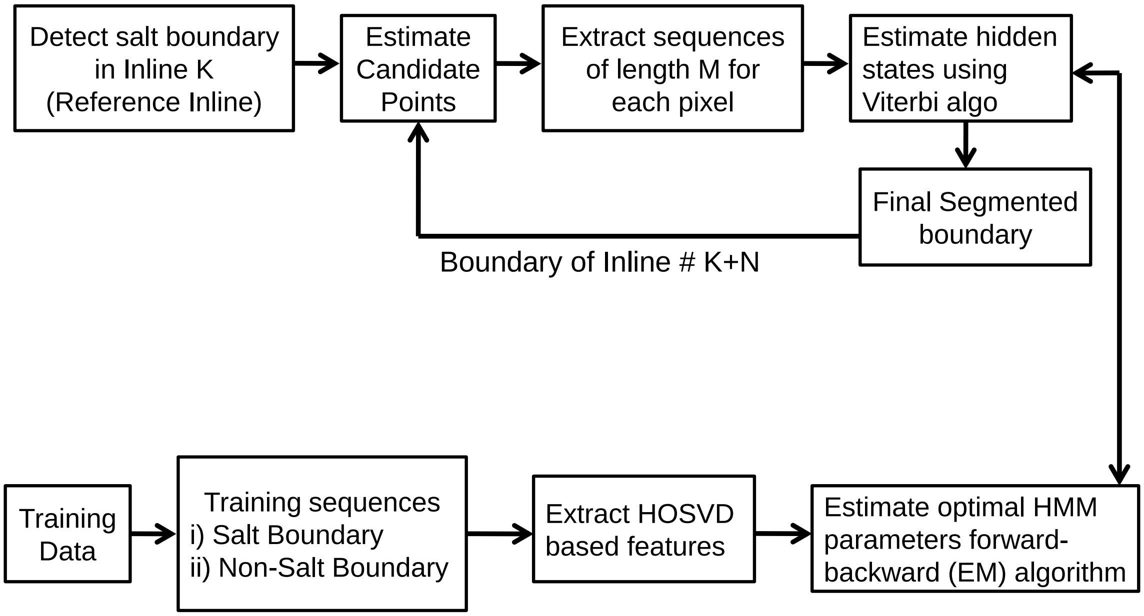

Figure 6.3: Workflow for salt dome tracking using HMM

6.3 Experimental Results

We tested our salt dome detection method on the Netherlands offshore F3 block acquired in the North Sea. In the first case, we used the discrete gray level values as features (1 dimensional feature vector) for the proposed HMM based salt dome detection method. The initial parameters $\theta = (\Gamma, B, \pi)$ were estimated using the gray level values of the training sequences. For a given test inline, we first take the pixels row-wise and estimate the state sequences. State can either be 1 (background) or 2 (foreground). An edge is present at the point where there is a change in state (1 to 2, or 2 to 1). For the same inline, once we have computed the horizontal edges, we take the pixels column-wise and calculate the vertical edges. A combination of horizontal and vertical edges gives us the final result. Fig.6.4 (b) & (c) shows the horizontal and vertical edge maps computed for test Inline # 126. Fig.6.4 (c) shows the combined gradient map. Fig.6.4 (e) & (f) shows the salt boundary detected for the Inline # 126 using the proposed HMM based method.

The HMM-based method, using the gray level features, is able to detect the salt boundaries with good accuracy especially where the boundary is represented by strong reflectors. However, in absence of strong edges, the proposed method fails to detect the boundary accurately as can be seen in Fig.6.4 (e). We overcome this drawback by using the proposed HOSVD-based features, the trace and the largest singular value attribute. For each point in a training sequence, we extract a volume of size 5 x 5 x 3 (inline x crossline x time). The volume is then unfolded

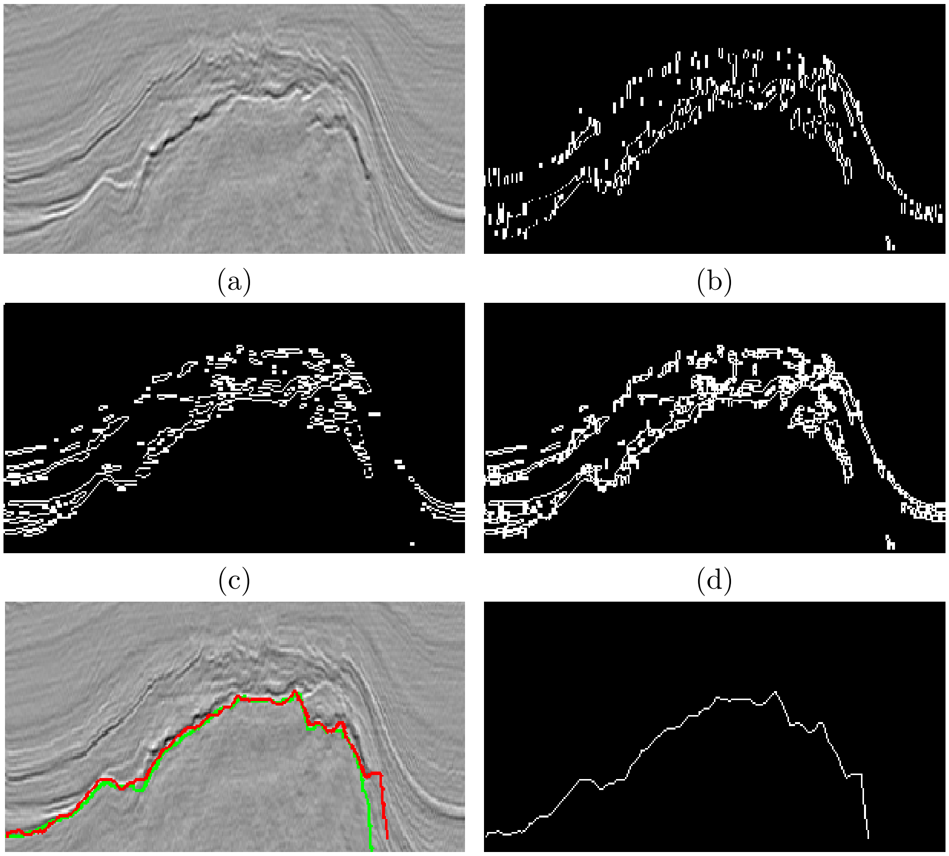

(a) (b)

(c) (d)

(e) (f)

Figure 6.4: (a) Inline # 126, (b) Horizontal gradient map using HMM, (c) Vertical gradient map using HMM , (d) Combined gradient map (e-f) Salt boundary detected in Inline # 126 using the HMM with gray level features.

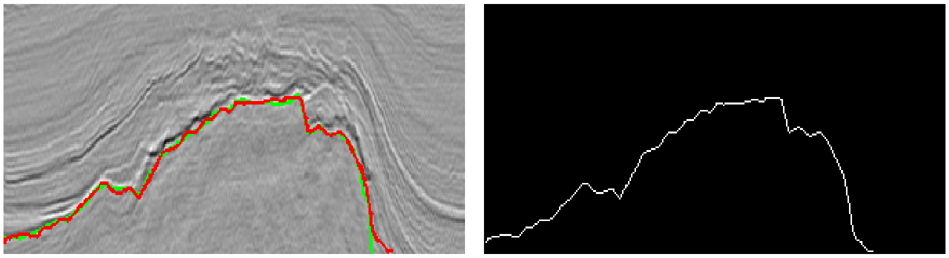

(a) (b)

Figure 6.5: Salt boundary detected in Inline # 126 using the proposed HMM algorithm with HOSVD-based features (Red), Ground truth (Green).

along inline, crossline, and time directions using the concept of tensors as discussed in the previous section. From the unfolded matrix, we compute the trace and largest singular value attributes. These attributes are used to estimate the optimal parameters $(\Gamma, B\ (1\ Guassian,\ \ K\ \ features), \pi)$, for the HMM, using the EM algorithm. For a test Inline, the hidden states for all the points are computed using the estimated HMM. The estimated states are then used to delineate the salt dome boundaries.

Fig.6.5 (a) & (b) shows the salt boundary detected for the Inline # 126 using the proposed HMM-based algorithm with HOSVD-based features. We see that the proposed method is able delineate the salt boundary with excellent accuracy. The detected salt boundary (Red) is very close to the ground truth (Green). In Fig.6.6, we provide two more examples of salt boundaries detected in Inlines # 111 and 134 using the proposed method. The salt boundaries produced by the proposed method are very close to the ground truth.

We compare the performance of our proposed method with the edge detector based method [2], the texture attributes based method [43], and the hybrid edge-texture based method [9]. The texture attributes based salt dome detection

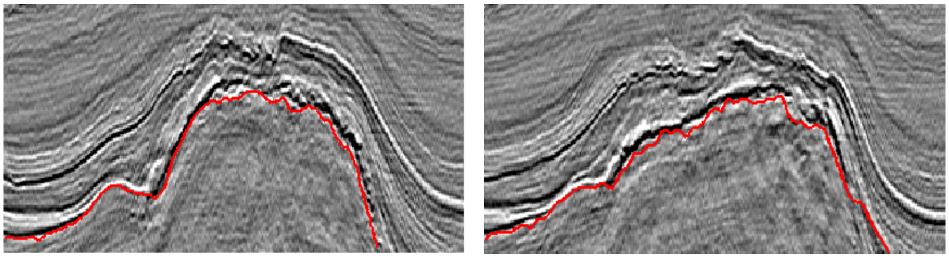

(a) (b)

Figure 6.6: Salt boundary detected using the proposed HMM method (a) Inline # 111, (b) Inline # 134

method [43] uses the GLCM based attributes, the Gabor filter based attributes, and the eigenstructure based attributes. This method has traditionally been used in previous papers for benchmarking purposes. In Fig 6.7 and 6.8, we show the results of the salt boundary detected using the proposed method, egde detector based method, the texture attributes based method, and the hybrid edge-texture based method. The salt boundary produced by the edge detector based method deviates a lot along the diagonals and at the end where the boundary is not represented by strong reflectors. The salt boundary detected by the texture attributes based method also loses the track at many points especially when the texture of salt boundary resembles to the horizon. The hybrid edge-texture based method produces better results than the edge-based and the texture-based methods, however this method fails to produce accurate results when the salt boundary has weak amplitude and the contrast variations along the salt boundaries are very small. The proposed HMM-based method, using HOSVD-based features, gives better results than the other methods and detects the salt boundary with great accuracy as can be seen.

We show in Table. 1 the classification accuracy for the Inlines # 126 to 135

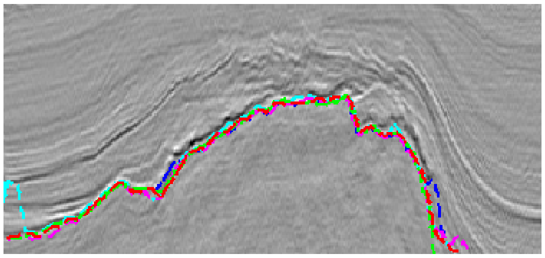

Figure 6.7: Salt boundary detected for Inline # 126 using the proposed HMM method (Red), the edge-based method (Blue), the texture-based method (Cyan), the hybrid edge-texture method (Purple), Ground truth (Green)

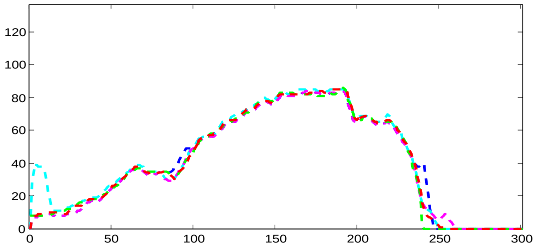

Figure 6.8: Salt boundary points detected for Inline # 126 using the proposed HMM method (Red), the edge-based method (Blue), the texture-based method (Cyan), the hybrid edge-texture method (Purple), Ground truth (Green)

Table 6.1: Classification Accuracy of the proposed HMM-based method and other methods

Salt Dome Detection Method	Accuracy (F-measure)
Proposed method	98.51%
Edge detection based method	96.82%
Texture based method	95.72%
Hybrid edge-texture method	97.36%

using the proposed method, the edge detector based method, the texture based method, and the hybrid edge-texture method. The classification accuracy, here, is the F-measure value which is considered as the state-of-the art evaluation metric in image segmentation problems. The proposed method gives an average accuracy of 98.70% which is 3% higher than the texture-based method, 2% higher than the edge-based method, and 1.2% better than the hybrid edge-texture method. The proposed method, using a single HMM, is computationally very efficient as

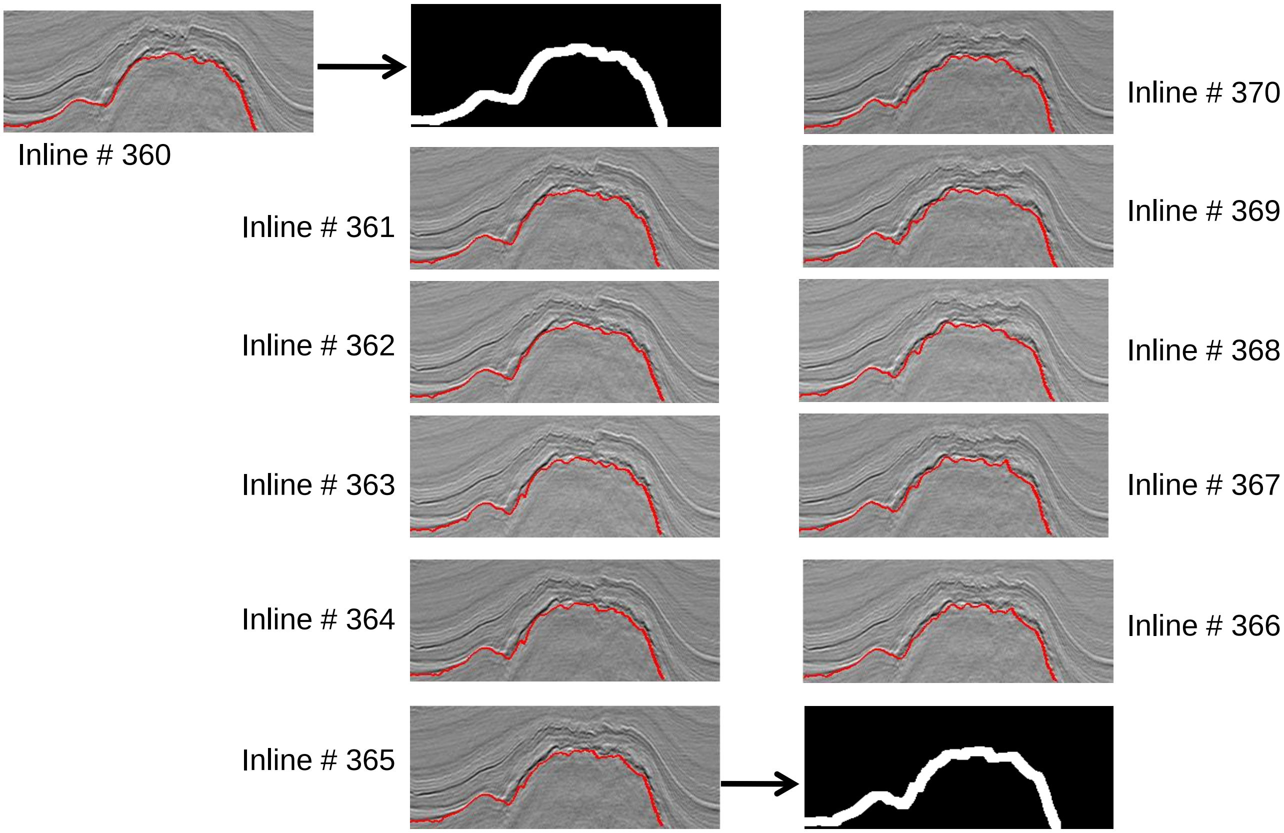

Figure 6.9: Salt boundary tracked, Inline # 361 - 370

compared to other classifier-based salt dome detection methods.

In Figure 6.9, we show the results for the salt boundary tracked in inlines # 361-370 using the proposed HMM tracking method. We first detect the salt boundary in Inline # 360 using the HMM detection model. Using the detected salt boundary in Inline # 360, we compute the candidate points (See Figure.6.2) for the next $N = 5$ inlines. The process is then repeated for the remaining Inlines. We observe in Figure 6.9 that the proposed method is able to track the salt boundary accurately.

In this chapter, we introduced a robust salt dome detection and tracking method for migrated seismic data using a Hidden Markov Model. The optimal

HMM parameters are estimated using the attributes computed from the HOSVD projections along the inlines, crosslines, and time directions. The Viterbi algorithm is used to estimate the hidden states (salt or non-salt boundary), which are further used to delineate the salt dome boundaries. Our experimental results showed that the proposed HMM based detection framework, using the HOSVD attributes, can detect the salt boundaries with good accuracy outperforming existing edge-based, texture-based, and hybrid edge-texture based methods.

CHAPTER 7

CONCLUSION AND FUTURE RECOMMENDATIONS

7.1 Conclusion

In this thesis, we made a number of contributions towards salt dome detection from 2D and 3D seismic data. Starting with the existing seismic attributes, we proposed an extension of 2D edge-based salt dome detector to 3D taking into account continuity in the medium [15]. The advantage of our 3D multi-directional edge detector is the accurate delineation of salt boundaries especially along the diagonals and low complexity. A data-driven codebook based model [16] is also proposed using the texture-based attributes. The algorithm utilizes the K-means clustering algorithm to reduce the size of codebook, thus making the overall algorithm computationally efficient. The codebook model outperforms other patch-based approaches in terms of both accuracy and computational efficiency. We also combined the edge and texture-based classification models and proposed a hybrid approach for salt dome detection. This fusion was carried at the decision stage [9].

We also proposed new 3D seismic attributes computed using the concept of HOSVD. The proposed attributes were developed in accordance with the salt dome detection problem, therefore these attributes are able to differentiate accurately between the salt boundary and other regions. We also introduced an optimal set of attributes using information-theoretic based algorithms. The ranking order shows the importance and relevance of our HOSVD-based attributes.

A dictionary-based classification model [10] is proposed using the HOSVD-based attributes and a feature ranking framework. In this model, we also introduced a boundary refining step to detect the salt boundaries accurately within the classified patches. Finally, we proposed HMM models [18] to detect and track salt boundaries in 3D data. The HMM model uses the contextual information to increase the accuracy and reduce the computational time of the detection and tracking process.

In addition to the above discussed major contributions, additional research work is carried out and some important contributions to the area are made. These contributions include i) the development of a color image segmentation algorithm by combining the convex active contour and the chan vese Model [71], ii) the development of a texture-based interpretation work flow with application to delineating salt domes [11] iii) new LRI-based seismic attributes for seismic retrieval and scene labeling [19] , iv) the development of a fault tracking algorithm in seismic volumes using tracking vectors [72]. These contributions complements the work presented in the thesis.

7.2 Future Recommendations

Accurate detection of salt domes is vital to the Oil and Gas exploration process. The cost of exploration process can be reduced significantly using accurate interpretation methods. Based on the research work discussed in this thesis, the following future recommendations are proposed:

- **Detection of other seismic events: Horizons, Seismic facies, etc**

  The proposed approaches can be used to detect other useful events such as horizons, chaotic horizons, seismic facies, etc. In addition to salt domes and faults, these events also provide useful information about earth sub-surfaces which can assist in exploration processes.

- **Salt dome detection algorithms for compressed data**

  Seismic datasets used in oil and gas industry are usually of the order of tera-bytes. Compression schemes are often used to reduce the size of seismic data. However, there are some distortions that occur in seismic data due to lossy compression. The challenge is to develop robust salt dome detection approaches for compressed seismic data without compromising the accuracy of the interpretation process. The HOSVD-based approach proposed in this thesis can be extended to work with compressed data.

- **Interactive framework for visualizing results**

  It is also important to develop a 3D interactive visualization platform to analyze the results of seismic interpretation. In the case of fully automated algorithms, the interactive platform will give user the flexibility to intervene at any time. For example, the user may input some manual labels to be used in the optimization process. The user can also decide on the desired degree of interactivity, e.g., by setting the number of iterations to skip between two display updates.

- **Scene labeling in seismic volumes**

  Over the last few years, the labeling of seismic volumes using machine learning approaches has attracted a lot of interest from the geophysics community. The accurate scene labeling can assist interpreters in identifying various events. However, it is challenging to develop efficient approaches for accurate labeling in seismic surveys due to small texture variations across different events.

- **Development of new techniques for 3D medical applications**

  The 3D seismic data exhibits contrasting similarities with medical data such as MRI, mammogram images, etc. The proposed segmentation approaches can, therefore, be used with medical images for segmentation applications.

REFERENCES

[1] ([Dec. 20, 2014]) http://www.opendtect.org/.

[2] Z. Jing, Z. Yanqing, C. Zhigang, and L. Jianhua, "Detecting boundary of salt dome in seismic data with edgedetection technique," in *SEG Technical Program Expanded Abstracts 2007*, 2007.

[3] A. A. Aqrawi, T. H. Boe, and S. Barros, "Detecting salt domes using a dip guided 3d sobel seismic attribute," in *SEG Annual Meeting*, 2011.

[4] L. J., C. R., and B. Biondi, "Application of image segmentation to tracking 3d salt boundaries," *GEOPHYSICS*, vol. 72, no. 4, pp. P47–P56, 2007.

[5] A. Halpert, R. Clapp, and B. Biondi, "Seismic image segmentation with multiple attributes," in *SEG Technical Program Expanded Abstracts*, 2009, pp. 3700–3704.

[6] ——, "Speeding up seismic image segmentation," in *SEG Technical Program Expanded Abstracts*, 2010.

[7] J. Hauks, O. R. Ravndal, B. Fotland, A. Bounaim, and L. Sonneland, "Automated salt body extraction from seismic data using the level set method," *First Break*, vol. 31, pp. P35–P42, 2013.

[8] A. Berthelot, A. H. Solberg, and L.-J. Gelius, "Texture attributes for detection of salt," *J. of Applied Geophysics*, vol. 88, pp. 52 – 69, 2013.

[9] A. Amin and M. Deriche, "A hybrid approach for salt dome detection in 2d and 3d seismic data," in *Image Processing (ICIP), 2015 IEEE International Conference on*, 2015, pp. 2537–2541.

[10] A. Amin, M. Deriche, T. Hegazy, Z. Wang, G. AlRegib *et al.*, "A novel approach for salt dome detection using a dictionary-based classifier," in *2015 SEG Annual Meeting*, 2015.

[11] M. A. Shafiq, Z. Wang*, A. Amin, T. Hegazy, M. Deriche, and G. AlRegib, "Detection of salt-dome boundary surfaces in migrated seismic volumes using gradient of textures," in *SEG Technical Program Expanded Abstracts 2015*, 2015, pp. 1811–1815.

[12] A. Berthelot, A. H. S. Solberg, E. Morisbak, and L.-J. Gelius, "Salt diapirs without well defined boundaries - a feasibility study of semi-automatic detection," *GEOPHYSICS PROSPECT*, vol. 59, pp. P682–P696, 2011.

[13] T. K.M. and de Rooij M, "Semi-automatic detection of faults in 3d seismic data," *GEOPHYSICS PROSPECT*, vol. 53, pp. P533–P542, 2005.

[14] B. M.R., R. M.A., and T. K., "Semi-automatic detection of faults in 3d seismic data," *Journal of Seismic Exploration*, vol. 18, pp. P289–P304, 2009.

[15] A. Asjad and D. Mohamed, "A new approach for salt dome detection using a 3d multidirectional edge detector," *Applied Geophysics*, vol. 12, no. 3, pp. 334–342, 2015.

[16] A. Amin and M. Deriche, "Salt-dome detection using a codebook-based learning model," *IEEE Geoscience and Remote Sensing Letters.*

[17] M. Deriche, "Robust salt-dome detection using the ranking of texture-based attributes," *Applied Geophysics*, vol. 13, no. 3, pp. 449–458, 2016. [Online]. Available: http://dx.doi.org/10.1007/s11770-016-0569-6

[18] A. Amin, M. Deriche, and B. Liu, "A novel approach for salt dome detection in seismic surveys using a hidden markov model," in *SEG Technical Program Expanded Abstracts 2016.* Society of Exploration Geophysicists, 2016, pp. 1688–1692.

[19] Z. Long, Y. Alaudah, M. A. Qureshi, M. Al Farraj, Z. Wang, A. Amin, M. Deriche, G. AlRegib *et al.*, "Characterization of migrated seismic volumes using texture attributes: a comparative study," in *2015 SEG Annual Meeting*, 2015.

[20] R. C. Gonzalez and E. Richard, "Woods, digital image processing," *ed: Prentice Hall Press, ISBN 0-201-18075-8*, 2002.

[21] J. Canny, “A computational approach to edge detection,” *Pattern Analysis and Machine Intelligence, IEEE Transactions on*, vol. PAMI-8, no. 6, pp. 679–698, 1986.

[22] J. Shi and J. Malik, “Normalized cuts and image segmentation,” *IEEE Transactions on Pattern Analysis and Machine Intelligence*, vol. 22, no. 8, 2000.

[23] H. D. and J. Emanuel, “Atomic meshing of seismic images,” in *SEG Expanded Abstracts*, 2002.

[24] H. D. and J. U. Emanuel, “Seismic interpretation using global image segmentation,” in *SEG Expanded Abstracts*, 2003.

[25] J. Lomask and . B. Biondi, “Image segmentation for tracking salt boundaries: Stanford exploration,” *project report*, vol. 193200, 2003.

[26] L. J. B. Biondi and J. Shragge, “Image segmentation for tracking salt boundaries,” in *SEG Annual Meeting*, 2004.

[27] L. J. R. G. Clapp and B. Biondi, “Parallel implementation of image segmentation for tracking 3d salt boundaries,” in *68th Annual International Meeting, EAGE, Expanded Abstracts*, 2006.

[28] H. A., C. R., L. J., and B. Biondi, “Image segmentation for velocity model construction and updating,” in *SEG Technical Program Expanded Abstracts*, 2008, pp. 3088–3092.

[29] J. Bednar, “Least squares dip and coherency attributes,” *Leading Edge (Tulsa, OK)*, vol. 17, no. 6, p. 775, 1998, cited By 5.

[30] P. F. Felzenszwalb and D. P. Huttenlocher, “Efficient Graph-Based Image Segmentation,” *Int. J. Comput. Vision*, vol. 59, no. 2, pp. 167–181, 2004.

[31] C. Zahn, “Graph-theoretical methods for detecting and describing gestalt clusters,” *IEEE Trans. on Computers*, vol. C-20, no. 1, pp. 68–86, 1971.

[32] A. Halpert, “Model building with image segmentation and fast image updates,” in *SEG Technical Program Expanded Abstracts*, 2011, pp. 4035–4039.

[33] Y. Zhang and A. Halpert, “Enhanced interpreter-aided salt boundary extraction using shape deformation,” in *SEG Technical Program Expanded Abstracts*, 2012, pp. 1–5.

[34] M. A. Shafiq, Z. Wang, and G. AlRegib, “Seismic interpretation of migrated data using edge-based geodesic active contours,” in *Signal and Information Processing (GlobalSIP), IEEE Global Conference on*, 2015.

[35] S. Wang, W. Zhu, and Z.-P. Liang, “Shape deformation: Svm regression and application to medical image segmentation.” in *ICCV*, 2001, pp. 209–216.

[36] C. Ferguson, A. Avu, N. Schofield, and G. Paton, “Seismic analysis workflow for reservoir characterization in the vicinity of salt,” *First Break*, vol. 28, no. 10, pp. 107–113, 2010, cited By 2.

[37] J. Sethian, “Level set methods and fast marching methods,” *Cambridge University Press*, vol. 2, 1999.

[38] S. Osher and J. A. Sethian, “Fronts propagating with curvature-dependent speed: Algorithms based on hamilton-jacobi formulations,” *Journal of Computational Physics*, vol. 79, no. 1, pp. 12–49, 1988.

[39] B. Kadlec, G. Dorn, and H. Tufo, “Interactive visualization and interpretation of geologic surfaces in 3-d seismic data,” in *SEG Technical Program Expanded Abstracts*, 2009, pp. 1147–1151.

[40] T. Hanning and G. M. Pisinger., “A pixel-based segmentation algorithm of color images by n-level-fitting,” in *5th international association of science and technology for development, Computer graphics and imaging*, 2002.

[41] J. B. MacQueen, “Some methods for classification and analysis of multivariate observations,” in *Proc. of the fifth Berkeley Symposium on Mathematical Statistics and Probability*, L. M. L. Cam and J. Neyman, Eds., vol. 1. University of California Press, 1967, pp. 281–297.

[42] Y. Gdalyahu, D. Weinshall, and M. Werman, “Self-organization in vision: Stochastic clustering for image segmentation, perceptual grouping, and image database organization.” *IEEE Trans. Pattern Anal. Mach. Intell.*, vol. 23, no. 10, pp. 1053–1074, 2001.

[43] A. Berthelot, A. H. S. Solberg, E. Morisbak, and L.-J. Gelius, "3d segmentation of salt using texture attributes," in *SEG Technical Program Expanded Abstracts 2012*, 2012, pp. 1–5.

[44] T. Hegazy and G. AlRegib, "Texture attributes for detecting salt bodies in seismic data," in *2014 SEG Annual Meeting*, 2014.

[45] G. Winkler, "Smoothers for discontinuous signals," *Journal of Nonparametric Statistics*, vol. 14, no. 1, pp. 203–222, 2002. [Online]. Available: http://www.informaworld.com/10.1080/10485250211388

[46] T. Randen and J. H. Husy, "Filtering for texture classification: A comparative study." *IEEE Trans. Pattern Anal. Mach. Intell.*, vol. 21, no. 4, pp. 291–310, 1999.

[47] R. T., M. E., S. C., A. A., H. J.O., S. T., and S. J, "Three-dimensional texture attributes for seismic data analysis," in *SEG Technical Program Expanded Abstracts*, 2003, pp. 668–671.

[48] T. Randen and L. Sønneland, *Atlas of 3D seismic attributes.* Springer, 2005.

[49] Z. Wang, T. Hegazy, Z. Long, and G. AlRegib, "Noise-robust detection and tracking of salt domes in postmigrated volumes using texture, tensors, and subspace learning," *Geophysics*, vol. 80, no. 6, pp. WD101–WD116, 2015.

[50] S. Chopra and K. J. Marfurt, "Seismic attributesa historical perspective," *Geophysics*, vol. 70, no. 5, pp. 3SO–28SO, 2005.

[51] M. Forrest, “Bright investments paid off: Aapg explorer,” 2000.

[52] R. J. Lisle, “Detection of zones of abnormal strains in structures using gaussian curvature analysis,” *AAPG bulletin*, vol. 78, no. 12, pp. 1811–1819, 1994.

[53] R. M. Haralick, K. S. Shanmugam, and I. Dinstein, “Textural features for image classification.” *IEEE Transactions on Systems, Man, and Cybernetics*, vol. 3, no. 6, pp. 610–621, 1973.

[54] D. Gao, “Volume texture extraction for 3d seismic visualization and interpretation,” *GEOPHYSICS*, vol. 68, pp. P1294–P1302, 2003.

[55] A. Beghdadi, M. A. Qureshi, and M. Deriche, “A critical look to some contrast enhancement evaluation measures,” in *Colour and Visual Computing Symposium (CVCS), 2015.* IEEE, 2015, pp. 1–6.

[56] Y. Zhai, D. L. Neuhoff, and T. N. Pappas, “Local radius index-a new texture similarity feature,” in *International Conference on Acoustics, Speech and Signal Processing (ICASSP).* IEEE, 2013, pp. 1434–1438.

[57] T. M.R., “Texture discrimination by gabor functions,” *Biological Cybernetics*, vol. 55, pp. P71–P82, 1986.

[58] M. Clark, A. C. Bovik, and W. S. Geisler, “Texture segmentation using gabor modulation/demodulation.” *Pattern Recognition Letters*, vol. 6, no. 4, pp. 261–267, 1987.

[59] A. Jain and F. Farrokhnia, “Unsupervised texture segmentation using gabor filters,” *Pattern recognition*, vol. 24, no. 12, pp. 1167–1186, 1991.

[60] A. C. Bovik, “Analysis of multichannel narrow-band filters for image texture segmentation.” *IEEE Transactions on Signal Processing*, vol. 39, no. 9, pp. 2025–2043, 1991.

[61] A. C. Bovik, N. Gopal, T. Emmoth, and A. Restrepo, “Localized measurement of emergent image frequencies by gabor wavelets.” *IEEE Transactions on Information Theory*, vol. 38, no. 2, pp. 691–712, 1992.

[62] Z. Jin-Yu, C. Yan, and H. Xian-Xiang, “Edge detection of images based on improved sobel operator and genetic algorithms,” in *Image Analysis and Signal Processing, 2009. IASP 2009. International Conference on.* IEEE, 2009, pp. 31–35.

[63] T. G. Kolda and B. W. Bader, “Tensor decompositions and applications,” *SIAM review*, vol. 51, no. 3, pp. 455–500, 2009.

[64] R. Battiti, “Using mutual information for selecting features in supervised neural net learning,” *Neural Networks, IEEE Transactions on*, vol. 5, no. 4, pp. 537–550, 1994.

[65] H. Peng, F. Long, and C. Ding, “Feature selection based on mutual information criteria of max-dependency, max-relevance, and min-redundancy,” *Pattern Analysis and Machine Intelligence, IEEE Transactions on*, vol. 27, no. 8, pp. 1226–1238, 2005.

[66] H. H. Yang and J. E. Moody, "Data visualization and feature selection: New algorithms for nongaussian data." in *NIPS*, vol. 99. Citeseer, 1999, pp. 687–693.

[67] P. E. Meyer, C. Schretter, and G. Bontempi, "Information-theoretic feature selection in microarray data using variable complementarity," *Selected Topics in Signal Processing, IEEE Journal of*, vol. 2, no. 3, pp. 261–274, 2008.

[68] G. Brown, A. Pocock, M.-J. Zhao, and M. Luján, "Conditional likelihood maximisation: a unifying framework for information theoretic feature selection," *The Journal of Machine Learning Research*, vol. 13, no. 1, pp. 27–66, 2012.

[69] D. L. Donoho, Y. Tsaig, I. Drori, and J. luc Starck, "Sparse solution of underdetermined linear equations by stagewise orthogonal matching pursuit," Tech. Rep., 2006.

[70] Q. S. ul Haq, L. Tao, F. Sun, and S. Yang, "A fast and robust sparse approach for hyperspectral data classification using a few labeled samples." *IEEE T. Geoscience and Remote Sensing*, vol. 50, no. 6, pp. 2287–2302, 2012.

[71] A. Amin and M. Deriche, "Robust image segmentation based on convex active contours and the chan vese model," in *Signal and Information Processing (GlobalSIP), 2014 IEEE Global Conference on*. IEEE, 2014, pp. 1044–1048.

[72] Z. Wang, Z. Long, G. AlRegib, A. Asjad, and M. A. Deriche, "Automatic fault tracking across seismic volumes via tracking vectors," in *2014 IEEE*

International Conference on Image Processing (ICIP). IEEE, 2014, pp. 5851–5855.

Vitae

- Name: Asjad Amin
- Nationality: Pakistan
- Date of Birth: 17 April, 1986
- Permanent Address: Bahawalpur, Pakistan
- Phone: (+92) 3006801053
- Email: *asjad.amin@gmail.com*
- M.S. Electrical Engineering, May 2012
- B.S. Electrical Engineering, June 2007